GROWTH AND REMODELING OF EXTRACELLULAR MATRIX DURING LIMB DEVELOPMENT

by

Yue Leng

A Dissertation

Submitted to the Faculty of Purdue University

In Partial Fulfillment of the Requirements for the degree of

Doctor of Philosophy

Weldon School of Biomedical Engineering

West Lafayette, Indiana

December 2020

THE PURDUE UNIVERSITY GRADUATE SCHOOL
STATEMENT OF COMMITTEE APPROVAL

Dr. Sarah Calve, Chair
Weldon School of Biomedical Engineering

Dr. Adrian Buganza Tepole
School of Mechanical Engineering
Weldon School of Biomedical Engineering

Dr. Eric A. Nauman
School of Mechanical Engineering
Weldon School of Biomedical Engineering

Dr. Luis Solorio
Weldon School of Biomedical Engineering

Dr. Shihuan Kuang
School of Agricultural and Biological Engineering

Approved by:
Dr. George R. Wodicka

This dissertation is dedicated to my family, my amazing professors and mentors, and my friends, who encouraged me to pursue my dreams and helped me in all things great and small.

ACKNOWLEDGMENTS

I want to express my thankfulness to the following people mentioned in this section, who have helped me enormously during my doctorate study at Purdue University. Without their supportive advice, I could not have gone this far for my degree.

First and foremost, I would like to express my sincere gratitude and appreciation to my major advisor, Dr. Sarah Calve, for her continuous support throughout my entire Ph.D. studies. Dr. Calve is extremely kind and patient and always provides tremendous help to her students when they have hard times. Inspired by her passion for research, critical thinking, target-oriented approach, I have become a better researcher and engineer. She is not only an inspiring mentor but also a caring friend, who kept me on the right track and helped me grow both professionally and personally. I am deeply grateful for the opportunity to be a part of her Musculoskeletal Extracellular Matrix Laboratory and proud that I have been working with her.

I would like to thank my wonderful Ph.D. committee members. Dr. Buganza Tepole is very supportive. I want to thank him for sharing his knowledge as well as his mentorship. He proposed many great ideas and spent lots of hours in guiding me on the modeling part. His suggestions always were insightful and helped me improve my research significantly. Without him, I wouldn't be able to finish the fourth chapter of this dissertation. I would also like to express my appreciation to Dr. Shihuan Kuang, Dr. Eric Nauman, and Dr. Luis Solorio for their valuable time and effort to instruct me and for their insights and comprehensive feedback on my doctoral research. They are always open to discuss my work and ask critical questions with engineering and biological perspectives, which helps the development of the scientific value of this dissertation. Their advice and guidance will benefit me throughout my life.

My gratitude also goes to the faculty and research collaborators at Purdue, such as Drs. Michael K. Wendt, David Umulis, Tamara Kinzer-Ursem, Donald Ready, and Jacqueline Linnes, who have supported me and the work. Additionally, I would like to thank the staff at the Weldon School of Biomedical Engineering especially Tammy Siemers and Sandra May, for everything they do to support students.

I would like to thank all the former and current members of our lab, particularly those who worked closely with me and gave valuable advice on the projects presented in this dissertation, including Dr. Ye Bu, Julian Jimenez, Kathryn Jacobson, Dr. Andrea Acuna, Sarah Lipp, Chenwei

Duan, Alexander Ocken, Juan Martin Silva Garcia, and Zhiyu Li. We have been through many time together solving challenging problems, building foundations for the projects. Without the dedicated teamwork and collaborations from these talented team members, I could not accomplish the work we have done. There are many other individuals I would like to thank for making my experiences at Purdue colorful and memorable, including my friends, instructors who worked together with me as a teaching assistant, classmates who helped me with courses, etc.

Next, my deepest gratitude goes to my family, especially my husband Dr. Sikai Chen and my parents. I would have never been able to make it this far without them. No words can express what their endless love, encouragement, trust, and unconditional support meant to me.

Finally, I would like to acknowledge the Weldon School of Biomedical Engineering and the Purdue Graduate School for granting me the Leslie A. Geddes Fellowship and the Bilsland Dissertation Fellowships. It was through these funding opportunities that I was able to carry out the doctoral studies in this dissertation

PREFACE

One chapter of this dissertation (**Chapters 2**) has been published in a peer-reviewed journal as noted at the start of the chapter. Minor changes in formatting and wording have been made for cohesive writing purposes.

The organization of this dissertation begins with an overview of this work and is followed by the background introduction to the extracellular matrix and an in-depth overview of its role in muscle, tendon, and their interface (**Chapters 1**). A special focus is laid on the interactions between the extracellular matrix and these tissues during the development of a functional musculoskeletal system. Next, the current methods to characterize extracellular matrix organization and model its network and mechanics are reviewed. **Chapter 2** focuses on characterizing the role of hyaluronic acid, a molecule that is found in abundance in the extracellular matrix of musculoskeletal tissues, during skeletal muscle development. **Chapter 3** presents the three-dimensional mapping of extracellular matrix organization and its instructive role in muscle and tendon formation during embryogenesis. Using fibrin gel as a prototype, **Chapter 4** includes a neural network based computational model to describe extracellular matrix mechanical properties. Finally, **Chapter 5** summarizes this dissertation by summing up its conclusion and reflecting on its contributions, as well as providing future research directions. A complete list of authored journal articles could be found in the Publications section.

TABLE OF CONTENTS

LIST OF TABLES

LIST OF FIGURES

LIST OF ABBREVIATIONS

CD44: cluster of differentiation 44

ColI: type I collagen

ColIII: type III collagen

ColV: type V collagen

DFN: discrete fiber networks

E: embryonic day (e.g. embryonic day 11.5, E11.5)

ECM: extracellular matrix

EdU: 5-ethynyl-2´-deoxyuridine

ERK1/2: extracellular signal-regulated kinase 1/2

FBN2: fibrillin-2

FCNN: fully connected neural networks

FE: finite element

FN: fibronectin

GAG: glycosaminoglycans

GFP: green fluorescent protein

GP: Gaussian process

HA: hyaluronic acid

HAS: hyaluronic acid synthase

HYAL: hyaluronidase

ML: machine learning

MTJ: myotendinous junction

NN: neural network

P: postnatal day

PG: proteoglycans

PI: protease inhibitors

RHAMM: receptor for hyaluronan-mediated motility

RVE: representative volume element

SCX: Scleraxis

SDS: sodium dodecyl sulfate

TGFβ: transforming growth factor β

UMAT: user material subroutine

WGA: wheat germ agglutinin

WT: wild type

3D: three-dimensional

4MU: 4-methylumbelliferone

ABSTRACT

Within the cellular microenvironment, the extracellular matrix (ECM) is an essential support structure that provides dynamic signaling cues through biochemical and physical factors. In response to interactions with the ECM, cells activate biochemical and mechanotransduction pathways that modulate their survival, migration, proliferation, differentiation, and function. Recent studies suggest the utility of ECM molecules as a basis for engineered scaffolds to restore functionality to damaged or missing tissues. However, current designs have poor functional outcomes. A reason engineered scaffolds have not been able to adequately restore the damaged tissue is that the scaffold design predominantly relies upon artificial polymers and/or ECM components that mimic the architecture and composition of the homeostatic adult tissue. Meanwhile, researchers investigating the mechanism of tissue formation and regeneration have primarily focused on the transcription factors and growth factor-induced signaling pathways controlling cell behaviors. What has yet to be fully taken into consideration by tissue engineers is that the composition and mechanics of ECM undergoes dramatical remodeling during development and scar-free repair, which plays a significant role in directing cellular behavior in the formation of mature functional tissue.

Here, we focus on the musculoskeletal system, and the hypothesis driving this research is that an ECM-based template is crucial for the functional muscle formation during vertebrate forelimb development. To test our hypothesis, we first evaluate how hyaluronic acid, a main skeletal muscle ECM component, regulates myogenesis. Secondly, we investigate the musculoskeletal ECM as a whole using clearing methods to see how the ECM template guides the muscle fiber alignment and growth in the murine developing forelimb. Third, we develop a multiscale computational model to help characterize macroscale growth and remodeling which is driven by microscale ECM remodeling processes. Taken together, a better understanding of the synergistic biochemical and biomechanical interactions between cells and the ECM will provide critical insight into the mechanisms that orchestrate tissue assembly and establish guidelines for regenerative therapies.

1. INTRODUCTION

1.1 Overview

The formation of complex and heterogeneous musculoskeletal system is a highly regulated process that depends on the interplay between a wide range of cell-autonomous and extrinsic factors. Muscle and tendon, arising from different embryological origins, are initially specified independently, but later seamlessly integrate as development progresses (Huang, 2017). However, muscle, tendon, and their interface called myotendinous junction (MTJ) represent significant healthcare challenges after injury due to tissue complexity (Bayrak & Yilgor Huri, 2018). Tissue engineering is a promising strategy to repair each tissue and its interface when natural healing fails (Mase et al., 2010). The utilization of replacement scaffolding materials as delivery platforms for progenitor cells aims to enhance large scale tissue repair by recruiting more cells available for endogenous regeneration (Grasman et al., 2015). To direct functional tissue formation, scaffolds should mimic the complex structural and functional features of tissues which can facilitate cellular events such as cell alignment and migration, promote tissue growth, and stimulate vascularization and innervation (Borschel et al., 2006). Unfortunately, multiple complicated factors that affect the biological and mechanical outcomes make it difficult to accurately and precisely mimic nature tissue, so that current design of scaffolds lead to nonideal recovery (Beldjilali-Labro et al., 2018). A reason engineered scaffolds have not been able to adequately restore the damaged tissue is that the scaffold design predominantly relies upon artificial polymers (Cronin et al., 2004; Kamelger et al., 2004) and/or extracellular matrix (ECM) components that mimic the architecture and composition of the homeostatic adult tissue (Borselli et al., 2011; Chen & Walters, 2013; Page et al., 2011). What is not fully taken into consideration by tissue engineers is that the composition and mechanics of musculoskeletal ECM undergo dramatic remodeling during development and scar-free repair, which plays a significant role in directing cellular behavior in the formation of mature functional tissue. Researchers investigating the mechanism of tissue formation and regeneration have primarily focused on the transcription factors and growth factor-induced signaling pathways controlling cell behaviors (Nassari et al., 2017). Even though the intrinsic molecular signals regulating musculoskeletal assembly have been well documented, the interactions among muscle, tendon, and surrounding ECM during development are not completely

elucidated. As the essential non-cellular component of all tissues, the ECM provides both structural support and signaling regulation to surround cells and guide tissue assembly during embryogenesis by influencing cell survival, adhesion, migration, proliferation, and differentiation (Frantz et al., 2010). Structurally, some ECM proteins form a fibrillar environment around cells, while other molecules deposit a sheet-like basement membrane beneath cells. The biomechanical properties of ECM, such as stiffness, also provide cells with regulatory information (Walma & Yamada, 2020). Moreover, ECM offers biochemical cues through cell-ECM binding and regulate the location and bioactivity of signaling molecules (Frantz et al., 2010). In the process of establishing a functional musculoskeletal system during embryonic development, questions regarding (1) the spatiotemporal distribution of ECM molecules with respect to the cells of the developing musculoskeletal system, and how these ECM components specifically regulate tissue specification, patterning, and differentiation; (2) what directs the characteristic alignment of muscle and tendon progenitors prior to differentiation, and how the progenitor cells are flawlessly integrated to form a functional unit; (3) how local remodeling of ECM at the cellular level during embryogenesis leads to the emergent mechanical properties at the tissue level remain poorly understood.

The ***central hypothesis*** driving this research is that *an ECM-based template deposited before muscle and tendon differentiation is crucial for the formation of muscle and tendon, and required to direct the proper assembly of the muscle-tendon interface during vertebrate forelimb development.* Understanding how the ECM guides and interacts with these tissues will provide critical insight into the mechanisms that orchestrate musculoskeletal assembly and establish guidelines for regenerative therapies that aim to restore functional muscle, tendon, and muscle-tendon junction in diseased and damaged tissues. By harnessing the basic elements nature uses to assemble the musculoskeletal system *in vivo*, the functional integration of replacement constructs into the host will be enhanced.

Before we could fully answer the question regarding the role of ECM in musculoskeletal assembly, we first studied how hyaluronic acid (HA), a main skeletal muscle ECM component, regulates myogenesis. Secondly, we investigated the musculoskeletal ECM as a whole using decellularization and clearing methods to see how the ECM template guides the muscle and tendon fibers alignment and growth in the murine developing forelimb. Thirdly, we built a neural network-based computational model to describe fiber matrix mechanical properties at the microscale, so

that the tissue level growth and remodeling can be predicted with a multiscale model that is driven by microscale ECM remodeling processes.

1.2 Background

1.2.1 Composition and complexity of the ECM

The ECM is a complex, macromolecular network that is present in all biological tissues and organs (Frantz et al., 2010). ECM provides biomechanical and biochemical cues that cooperate in the integrated regulation of cell survival, migration, proliferation, and differentiation during tissue assembly (Bosman & Stamenkovic, 2003; Rozario & DeSimone, 2010). ECM is composed of several types of molecules, including glycosaminoglycans (GAGs), proteoglycans (PGs), and fibrous/network forming proteins (Figure 1.1).

GAGs are unbranched long linear chains of polysaccharides; GAGs are composed of repeating disaccharide blocks made up of alternating uronic acid and hexosamine units in highly negatively charged polysaccharide chains that are usually covalently linked to protein cores to form proteoglycan molecules (Raman et al., 2005). There are two main types of GAGs: nonsulfated GAG (hyaluronic acid) and sulfated GAGs (chondroitin sulfate, dermatan sulfate, heparan sulfate and heparin, and keratan sulfate) (Kusindarta & Wihadmadyatami, 2018). GAGs are present primarily on the cell or in the ECM, but also could be found in secretory vesicles in some cells (Varki et al., 1999). GAGs have high viscosity and low compressibility, which are ideal for lubrication and affect mechanical property of the tissue (Azeloglu et al., 2008). Their rigidity offers cells with structural integrity and passageways for cell migration. The tensile loading of the fiber network is exerted by the swelling pressure of inflated GAGs, which provides the ECM with shear stiffness and helps preserve the organization of the ECM (Maroudas, 1976). GAGs have also been shown to influence mechanosensing, which can be disrupted under disease conditions (Roccabianca et al., 2014).

Proteoglycans consist of core proteins and covalently attached large GAG side chains. Based on their location, PGs can be classified into four classes: intracellular, cell-surface, pericellular, and extracellular proteoglycans (Iozzo & Schaefer, 2015). Acting primarily in the extracellular space, PGs function either as a structural molecule or as ligands regulating cell migration, proliferation, cell-cell communication, and cell-matrix interactions during embryogenesis,

inflammation, and wound healing. (Ghatak et al., 2015; Iozzo & Schaefer, 2015). PGs provide proper alignment of fibrous and elastic elements in ECM (Smith & Melrose, 2015) and help tendon to resist high compression and tension associated with loading and mobilization (Yoon & Halper, 2005).

Fibrous/network forming proteins, including collagen, elastin, fibronectin, laminin, etc., are the most abundant proteins in the ECM (Ott & Rajab, 2016). They are secreted locally and assembled into the organized meshwork that provide structure and place for cells to adhere (Alberts et al., 2002; Muiznieks & Keeley, 2013). These proteins, mainly produced by connective tissue cells, are rich in skin, tendons, ligaments, bone, and cartilage. Fibrous extracellular networks give the dominant response to tissue mechanical forces (Muiznieks & Keeley, 2013). For example, collagen, a major abundant fibrous protein in the ECM, provides tissues with required tensile strength, enabling resistance to plastic deformation or rupture (Kusindarta & Wihadmadyatami, 2018). Elastin imparts resilience and extensibility, allowing tissues to withstand the repetitive cycle of mechanical loading (Gosline et al., 2002).

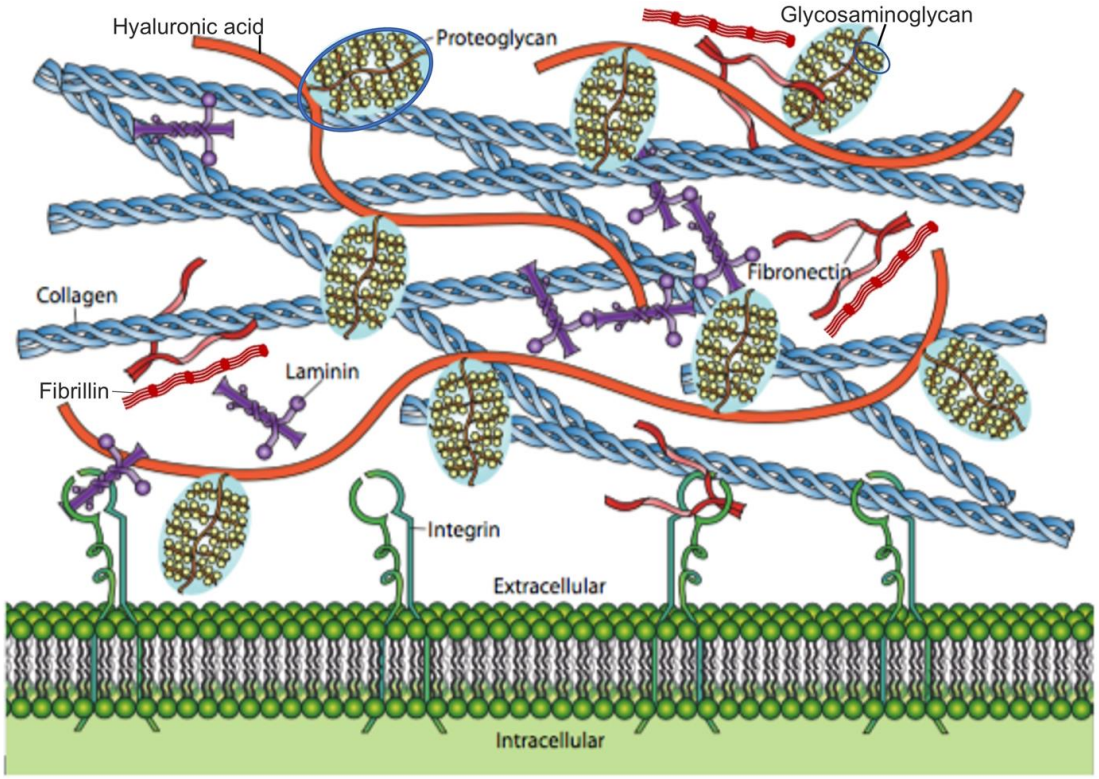

Figure 1.1. Schematic representation of complex structure of the natural ECM and the interactions between cells and the ECM components. The cellular receptors for a number of these ECM components are integrins. Adapted from (Bhagawati & Kumar, 2014; Wong, 2020).

Hyaluronic acid

Hyaluronic acid or hyaluronan (HA), which has a simple chemical structure but extraordinary biological features, is an ideal material for scaffolding, as HA not only serves as a synthetic building block, but also as a biological signaling motif (Toole, 2004). HA is a negatively charged, linear glycosaminoglycan that is found throughout the ECM of all vertebrate tissues, on the cell surface, and even inside cells (Dicker et al., 2014). Individual HA molecules are typically made up of 2,000 to 25,000 disaccharides, with a high molecular weight of 10^6–10^7 Da and extended molecular lengths of 2 to 25μm (Toole, 2004). These characteristics help regulate the hydration and viscosity of HA-containing tissues and contribute directly to the remodeling and cellular events that drive embryonic morphogenesis, tissue regeneration, and tumorigenesis (Itano, 2008). Through interactions with HA-binding proteoglycans (*e.g.* aggrecan and versican), HA maintains extracellular and pericellular matrix structural integrity via provision of a hydrated zone which facilitates cellular invasion during development and tissue remodeling (Dicker et al., 2014; Toole, 2001).

In addition, HA acts as a signaling molecule and mediates cellular behavior by binding to cell surface receptors, including the cluster of differentiation 44 (CD44) (Aruffo et al., 1990) and the receptor for HA-mediated motility (RHAMM) (Hardwick et al., 1992; Turley et al., 2002). CD44 is a ubiquitous, multi-domain cell surface glycoprotein that is considered to be the principal HA receptor (Aruffo et al., 1990). The N-terminal extracellular "link module" directly binds to HA. The C-terminal cytoplasmic tail is important for CD44-mediated intracellular signal transduction (Dzwonek & Wilczynski, 2015; Ponta et al., 2003). Cell type, cytoplasmic tail phosphorylation, and receptor clustering affect the activation state of CD44 and subsequently binding with HA (Isacke & Yarwood, 2002). HA-CD44 binding influences diverse processes, including cell-cell and cell-matrix adhesion, cell migration during development, inflammation, tumor growth, and metastasis (Lesley et al., 1993; Misra et al., 2015). In particular, the interaction between HA and CD44 is required for early adhesive cell-cell interactions of limb bud mesenchyme during limb bud outgrowth (Maleski & Knudson, 1996). CD44 also regulates growth and tissue integrity by mediating the cellular uptake and degradation of HA (Kaya et al., 1997; W. Knudson et al., 2002).

RHAMM (also known as CD168) (Hardwick et al., 1992), an acidic, coiled-coil protein expressed by many cell types, localizes to the nucleus, cytoplasm, and cell surface (Maxwell et al., 2008). It is thought that RHAMM binds HA via a BX7B motif on the -COOH terminus (Toole,

2001; Yang et al., 1994). Nuclear RHAMM, when bound to extracellular signal-regulated kinase 1/2 (ERK1/2) and mitogen-activated protein kinase (MEK), participates in cell motility and inflammation (Tolg et al., 2014). Cytoplasmic RHAMM interacts with microtubules and actin filaments in the cytoskeleton either directly, or through binding with microtubule- and centrosome-related proteins, to affect cell polarity and direct cell migration (Assmann et al., 1999; Silverman-Gavrila et al., 2011; Tolg et al., 2014). Extracellular RHAMM influences cellular transformation and cell migration during tissue injury and repair in a HA-dependent manner (Turley et al., 2002). In addition, RHAMM interacts with CD44, HA, and growth factors to activate protein tyrosine kinase signaling cascades that activate the ERK1,2 –MAP kinase cascade, which increases random motility (Tolg et al., 2014).

Although RHAMM and CD44 can participate independently in regulating cellular behaviors, their relative contributions are not clearly understood. When knocked out in vivo, these receptors have redundant or overlapping functions that can compensate for each other as evidenced by the viability of CD44-knockout and RHAMM-knockout mice (Nedvetzki et al., 2004; Schmits et al., 1997; Tolg et al., 2003). For example, in a collagen-induced arthritis model, the development of arthritis depended on CD44 in wild-type mice. However, in CD44-knockout mice, RHAMM expression was upregulated to compensate for the loss of CD44 and the induction of arthritis was RHAMM-dependent (Nedvetzki et al., 2004). Muscle repair is also influenced by CD44, wherein CD44-knockout mice show delayed repair in a tibialis anterior injury model (Mylona et al., 2006). Subsequent in vitro studies with myoblasts isolated from these mice indicated that lack of CD44 negatively influenced cell migration and differentiation (Mylona et al., 2006). Although many studies have shown RHAMM binds to HA to mediate cell migration (Gouëffic et al., 2006; Tolg et al., 2006), to date there have been no investigations into the role of RHAMM in skeletal muscle. Moreover, the relative contribution of the two types of HA receptors and the intracellular signaling pathways involved in HA-mediated effects in myogenesis remain unknown.

Collagen

Members of the collagen family are the most abundant proteins in the ECM summing up to 30% of the total protein mass of a body (Frantz et al., 2010). In ECM, collagens participate in forming the fibrillar network, and thus are the major structural element providing tensile strength, stabilizing the tissue and organs, and maintaining their structural integrity (Gelse et al., 2003).

Moreover, collagens also regulate cell adhesion, cell migration, and direct tissue development (Rozario & DeSimone, 2010). The bulk of collagen is predominantly synthesized by fibroblasts, but epithelial cells are also responsible for the secretion of some types of collagen (Alberts et al., 2002). The fibroblasts, either residing in the stroma or being recruited by the surrounding tissues, assemble collagen fibrils into sheet or cable structures and organize fibers with different alignments by exerting stress on the matrix.

While in a particular tissue or organ, collagens are usually a mixture of different types, one kind of them typically dominate (Frantz et al., 2010). So far, there are 46 different collagen genes that generate 28 different types of collagen fibrils (Ricard-Blum, 2011). The different collagen types are characterized by their complex structure, different splice variants, non-helical domains, various assemblies, and distinct functions. The main type of collagens (90%) belongs to the fibrillar collagens, or fibril-forming collagens (Gelse et al., 2003). These collagen molecules organize into thin (10-300 nm) and long (hundreds of microns) polymers (fibrils) (Alberts et al., 2002). Type I collagen is the most common of all, contributing to the skin (Watt & Fujiwara, 2011), blood vessels (Rhodes & Simons, 2007), bone (Tzaphlidou, 2008), muscle (Gillies & Lieber, 2011), ligament (Mäkisalo et al., 1989), and tendon (Zhang et al., 2005). Types II and XI collagen fibers predominantly form differentially aligned fibrillar networks of articular cartilage (Mayne, 1989). Together with type I collagen, Type III collagen is the major component of the interstitial matrix (Nielsen & Karsdal, 2016), and is abundant in collagen I containing tissues except for bone (Gelse et al., 2003). Type V collagen is usually codistributed with type I collagen in bone, skeletal muscle, and interstitial matrix of smooth muscle (von der Mark, 2006). Fibril-associated collagens, such as collagen types IX and XII, decorate the surface of collagen fibrils and regulate the diameter of the fibrils. Types IV and VII are network-forming collagens (Van Der Rest & Garrone, 1991). Types IV and VII belong to network-forming collagens (Alberts et al., 2002). Type IV collagen, with a more flexible triple helix, is the main constituent of the basement membrane and lined to the laminin network (Sudhakar & Kalluri, 2010).

Fibrillins

Fibrillins are large glycoproteins (350 kDa) that are arranged in a head-to-tail pattern and forms microfibrils distributed in connective tissues (Raghow, 2013; Sakai et al., 1991). The fibrillar structures have a diameter of 10-12 nm (Olivieri et al., 2010) and are either closely

associated or independent of elastic fibers (Kaur & Reinhardt, 2015). There are three homologous fibrillin proteins: fibrillin-1, fibrillin-2 (Fbn2), and fibrillin-3 (Kaur & Reinhardt, 2015). During embryogenesis, fibrillin-2 is broadly distributed and has more restricted expression in mesenchymal cells postnatally, whereas most adult microfibrils consist of fibrillin-1 (Apte, 2016). In the developing and mature limbs, fibrillin-1 and fibrillin-2 are expressed in a temporal and spatial specific manner (Kitahama et al., 2000). In the beginning, they are predominantly in the ECM of the emerging limb buds, but later, they are widely distributed and found in the perichondrium, growth plate, marrow stroma, and bone mostly (Loeys, 2013). In Fbn2 mutants, a decrease of collagen crosslinking is observed in tendon compared to wild type mice. Moreover, bone length in the extremities is also decreased (Boregowda et al., 2008). In contrast to the shorter skeletal phenotype in Fbn2 null mice, bone is overgrown in fibrillin-1 hypomorphic mice (Pereira et al., 1999). Fibrillin microfibrils function in the following way: (1) as scaffolds in which elastin is complexed, *e.g.* in the tunica media of the aorta; (2) as scaffolds in non-elastic tissues, such as the suspensory ligament of the lens and glomerular mesangium in kidney; and (3) as bonds between elastin and other components in the matrix, for example, connecting elastin fibers and the dermoepidermal junction of the skin (Kaplan, 2005). Fibrillins are also important in regulating TGFβs and BMPs by influencing their storage, release, and activation (Raghow, 2013).

1.2.2 Skeletal muscle development and its ECM

In vertebrates, appendicular skeletal muscle is derived from the somites, which are ball-like clusters of mesodermal precursor cells that form along the anterior-posterior axis of the embryo. In the developing limb, muscle progenitors delaminate from the dorsal portion of the somite (dermomyotome) and migrate into the forelimb bud between embryonic day (E)9.5 and E10.5 (Buckingham et al., 2003). These progenitor cells, or myoblasts, further differentiate into mononuclear myocytes, begin expressing myosin heavy chain isoforms, and fuse into contractile, multi-nucleated myofibers (Biressi et al., 2007). A distinct population of myogenic precursor cells, called satellite cells, remains on the surface of the myofibers in a quiescent undifferentiated state (Chargé & Rudnicki, 2004). The organization of these progenitors into a functional assemblage of limb muscles involves four successive phases of myogenesis (Biressi et al., 2007). Embryonic myogenesis (E10.5-E12.5) gives rise to the basic pattern. Fetal myogenesis (E14.5–birth) and neonatal myogenesis (P0–P21; P, postnatal day) are crucial for growth and maturation. Finally,

adult myogenesis (P21 and later) occurs to restore functionality after injury. Each phase involves migration, proliferation, differentiation, and fusion of myogenic precursors into multinucleated myofibers. A number of biochemical and mechanical factors are important regulators during myogenesis. In particular, it has been demonstrated that the surrounding connective tissue directs the organization of muscle in the developing limb (Mathew et al., 2011; Vallecillo-García et al., 2017). The connective tissue is primarily comprised of fibroblasts and the ECM these cells secrete (Mathew et al., 2011; Vallecillo-García et al., 2017); however, the exact composition of the ECM and how it directly regulates embryonic myogenesis remains unknown. As for transcription factors, Pax3/Pax7 expression is essential for the formation of all dermomyotome-derived myogenic precursors except those of the primary myotome (Relaix et al., 2005). Myogenesis is induced through the activation of the myogenic regulatory factors which commit cells to the myogenic lineage (Myf5, Mrf4, and MyoD) and then activate their differentiation program (myogenin, MyoD, and Mrf4) (Buckingham, 2006).

Skeletal muscle ECM can be classified into two layers: the interstitial matrix in the intercellular spaces, and the basement membrane on which the cells rest (Frantz et al., 2010). The first type consists of a tissue- and an age-specific mixture of a variety of collagen types, elastin, fibronectin, tenascins amongst others, as well as proteoglycans and glycosaminoglycans (such as HA) (Frantz et al., 2010). The second type of matrix (basement membrane) is in close contact with cells and has a different molecular composition than the surrounding interstitial matrix (Thorsteinsdóttir et al., 2011). It has sheet-like structures, primarily composed of laminins, type IV collagen, and perlecan (LeBleu et al., 2007). Laminins are the main basement membrane components. They are composed of a combination of three chains (α, β, and γ) which exist in different forms, forming at least 16 different laminins (Gullberg et al., 1999). During development, the expression type and level of ECM composition are dynamically changed. For example, during myogenesis, a huge amount of fibronectin secreted by myoblasts is gradually replaced by laminins in myotubes. Fibronectin promotes the adhesion and proliferation of myoblasts (Olwin & Hall, 1985). When myoblasts are subjected to differentiation, fibronectin is located primarily in the extracellular environment, whereas laminin synthesis increases in the cytosolic fraction (Grzelkowska-Kowalczyk et al., 2015). However, the precise spatio-temporal distribution of these ECM molecules with respect to the cells of the developing musculoskeletal system, and how these components specifically regulate myogenesis remains unclear.

The lack of objective information about muscle ECM compared to the other connective tissues of mesenchymal origin, such as bone and cartilage, is primarily because the geometry of muscle ECM is tremendously complex compared to other connective tissues. Didactic, but relatively arbitrary, presentations regarding muscle ECM often subdivide it into endomysial (around the muscle cell), perimysial (around groups of muscle cells), and epimysial (around the whole muscle) connective tissues (Figure 1.2), but how ECM transitions through these hierarchical structures from muscle to tendon are not clear. One of the hypotheses stated that perimysium is continuous with the tendon (Passerieux et al., 2007). As tendon and perimysium both contain primarily type I collagen, and the primary proteoglycan for both structures is decorin. In contrast, the epimysium and endomysium are made up of almost equal amounts of types I and III collagen and contain other proteoglycans. The structure of perimysium is also different from the mesh-like structure of endomysium (Passerieux et al., 2007).

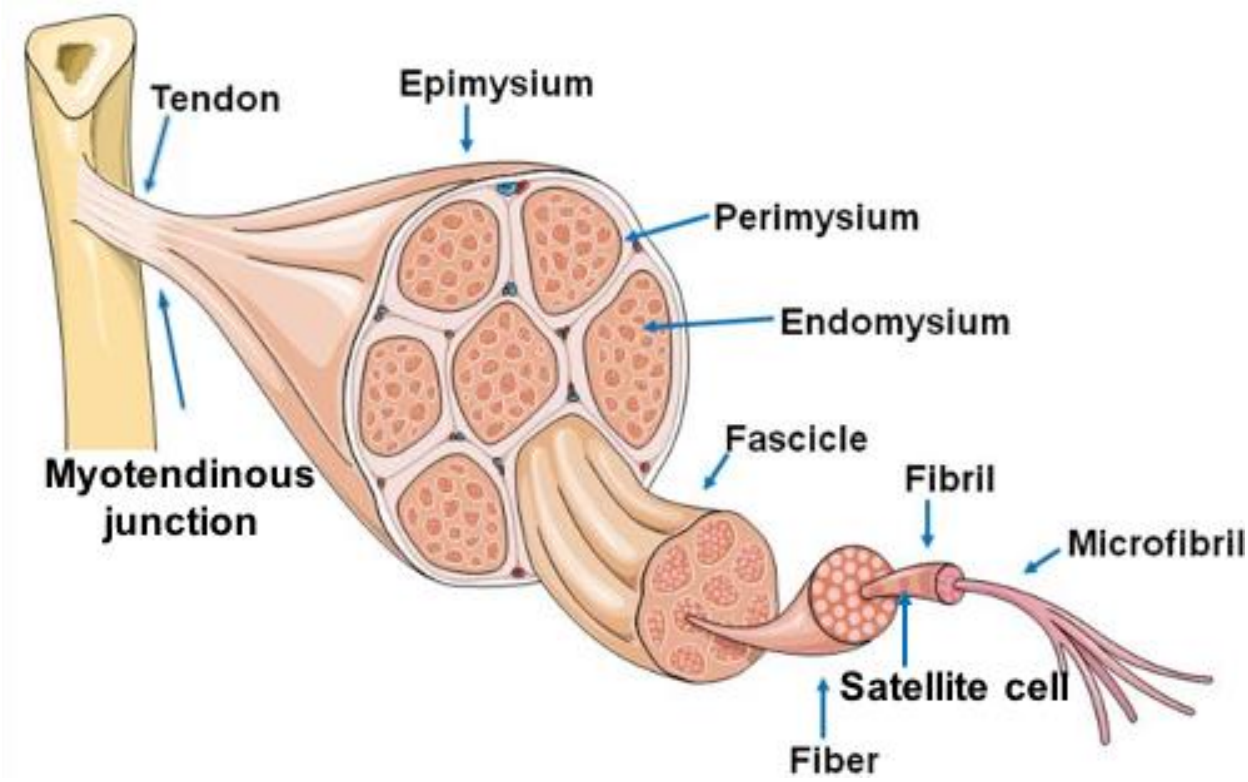

Figure 1.2. Diagram of the gross organization of muscle tissue and muscle ECM-tendon organization. Anatomical breakdown of skeletal muscle down to the microfibril and surrounding connective tissue layers. Adapted from (D'Cruz, 2016).

1.2.3 Tendon development and its ECM

Tendon is a connective tissue that attaches skeletal muscle to bone and enables different modes of locomotion by transmitting mechanical forces between muscles and bone. Tendon progenitors originate from the lateral plate mesoderm (Chevallier et al., 1977; R. Schweitzer et al., 2001). The development of tendon in the mouse limb is a multistage process composed of induction, recruitment, differentiation, and growth (Hasson, 2011; Huang, 2017; Huang et al., 2015). Transcription factor Scleraxis (Scx) and TGFβ signaling play key roles in this process (Edom-Vovard & Duprez, 2004; Murchison et al., 2007; Pryce et al., 2009). Scx is the earliest known marker of tendon progenitors. In the mouse limb, its expression is initially detected in limb buds at E10.5 in dorsal and ventral domains (R. Schweitzer et al., 2001). Apparent tendon pattern is not observed until E12.5, when divergent muscles are discernable and tendon progenitors align between the muscles and cartilages (Murchison et al., 2007). During E11.5–E12.5, TGFβ signaling is necessary for the recruitment and maintenance of limb tendon progenitors. No limb tendon progenitors are observed in TGFβ2 and TGFβ3 double mutants (Pryce et al., 2009). By E13.5, progenitor cells condense into aggregated tendon structures throughout the limb and express markers for tendon differentiation including Tnmd (Shukunami et al., 2001, 2006), Mkx (Ito et al., 2010; Liu et al., 2010), Col1a1, Egr1, and Egr2 (Guerquin et al., 2013; Lejard et al., 2011). Interestingly, while Scx expression from the early stages of tendon development suggested that it could be a master regulator of the tenocytes, there was no universal tendon loss due to the loss of the Scx. In Scx mutants, tendon progenitors are normal, phenotypes are not detectable until E13.5, and functional tendon structure is still formed. However, tendon phenotype is very extreme. These mutants, although viable, show reduced mobility because of the loss or disruption of all the long tendons. These results not only demonstrate the importance of Scx for normal development and effective force transmission of the tendon, but also suggest Scx does not label all the tendon progenitors (Murchison et al., 2007; Pryce et al., 2009).

Tendon ECM is mainly composed of collagen (60–85% dry weight) (Kannus, 2000; Kastelic et al., 1978). Type I is the predominant collagen (95% of the collagen) and the monomers aggregate together and form the basic tensile element in tendon, *i.e.* fibril (Trelstad & Hayashi, 1979). These fibrils usually have diameters of 50-500 nm, are bundled into fibers 1-20 μm in diameter, then are grouped into fiber bundles and fascicles ranging from 50-300 μm in diameter (Birk & Trelstad, 1986; Fukashiro et al., 1995). The division of tendon into fibrils not only stops minor

damage from spreading to the whole tissues but also equips tendon a high structural strength (Kjaer, 2004). Besides type I collagen, small levels of collagen types III, V, XI, XII, and XIV can be found (Banos et al., 2008; Hanson & Bentley, 1983; Riley, 2004). In addition, elastin fibers are also present (Svärd et al., 2020). A small amount of non-fibrous proteins are interspersed on each level of the hierarchically arranged structure (Kastelic et al., 1978), the major ones being PGs, including decorin (Derwin et al., 2001), biglycan (Dunkman et al., 2014), aggrecan (Rees et al., 2005). The PGs and water play a spacing and lubricating role for the tendon. ECM also contains other glycoproteins, such as tenascin-C (Martin et al., 2003), laminins, and fibronectin (Jozsa et al., 1989). Although these non-collagenous matrix proteins are known to be present in tendon tissue, details of the amounts, precise location, and function of specific components are generally poorly understood.

Appropriate ECM composition and structure enable tendon to perform its mechanical and biological functions (Screen et al., 2015). Most of the time, tendon (positional tendon) is loaded along the long axis in tension, enabling muscle to move the bone and thus making body motion possible (Galloway et al., 2013). Besides this, tendon (energy storing tendon) also functions as an elastic spring that stretches and stores energy, which rebound to the system through recoil to enhance the locomotion efficiency (Beldjilali-Labro et al., 2018; Biewener, 1998; Screen et al., 2015). Biologically, complex and dynamic cell-matrix interactions are critical for functional tendon (Bi et al., 2007). For example, tendon ECM controls the access of the growth factor to local cells, adjusting cell metabolism and ultimately affecting local matrix components and future growth factor availability, and thus regulates tendon growth, maintenance, and adaption to environments (Mikos et al., 2006).

1.2.4 The assembly of muscle-tendon interface

Tendon attaches to muscle through the ECM, forming a specialized junction called myotendinous junction (MTJ). Structurally speaking, MTJ consists of four distinct ultrastructural domains linking the collagen fibers in tendon with the actin filaments in muscle sarcomere to increase the surface area of attachment and provide mechanical resistance (Asahara et al., 2017). These domains are: (1) the internal lamina, composed of cross-linked actin filament networks; (2) the connecting domain, linking the internal lamina to the external lamina; (3) the lamina densa, a component of the basement membrane zone consisting of collagen IV, laminin, perlecan, and

proteoglycans; and (4) the matrix, occupying the area between the lamina densa and the collagen fibers (Bartels, 1987; Trotter et al., 1983).

MTJ development relies not only on the cross-talk between muscle and tendon cells, but also their interactions with ECM molecules and other cells. In zebrafish, the formation of myosepta (an analog of MTJ in mammal) is as follows: first, ECM is secreted and aggregated between muscle segments; then, recruitment of tenocytes occurs; next, ECM is further matured, and finally, tendon connects to the muscle (Charvet et al., 2011). In vertebrates, during embryogenesis, muscle and tendon progenitors first aggregate at the site of the future MTJ. Tenocytes produce a sparse fibrillar ECM matrix adjacent to muscle cells, which are starting to fuse into contractile myotubes. Later, a nascent basement membrane emerges surrounding the myotubes and collagens start to align in parallel due to random contractions. Meanwhile, ECM constrains the filaments in sarcomere to form a parallel organization. Correspondingly, sarcolemma resistance to the increasing forces results in the progressive formation of sarcomeres and the parallel aligned collagens. This procedure indicates a mechanical crosstalk between muscle and tendon cells. Collagen fibers grow in length, and finger-like processes between muscle and tendon start to develop. Then, after the completion of the basement membrane deposition and assembly, the myotubes which are not attached to the ECM are removed (Baldino et al., 2016; Kostrominova et al., 2009; Narayanan & Calve, 2020).

1.2.5 Visualization of 3D ECM structure *in situ*

The ability to obtain high-resolution 3D imaging of ECM is very valuable, such as how the 3D organization of these ECM components varies as a function of development, which is difficult to investigate in 2D (Ji et al., 2017). Confocal microscopy is a powerful optical imaging tool widely used for the visualization of the internal structure of biological tissues (Zhang et al., 2018). The development of diverse fluorescent labeling methods combined with confocal imaging has paved the path for 3D reconstruction of tissue structures with high-resolution (Gómez-Gaviro et al., 2020). However, visualization of the ECM in 3D has been hindered by the high scattering of biological tissues with limited penetration of light (Richardson & Lichtman, 2015). Thus, the image blurs and both the imaging resolution and contrast decrease as light propagates deeper into the tissue (Gratton, 2011).

Tissue optical clearing methods, such as CLARITY (Chung et al., 2013), SeeDB (Ke et al., 2013), and ClearT (Kuwajima et al., 2013), have emerged to reduce the scattering of light and make the tissue more transparent, which leads to significant enhancement of the imaging depth (Tuchin et al., 1997). For example, optical clearing based approaches have been used to improve the visualization of a certain type of ECM proteins, such as type IV collagen in the brain (Lee et al., 2016), and proteoglycans in connective tissues (Calve et al., 2015). In the case of human tissue, in order to diagnose and visualize endocrine and exocrine pathologies and to assess the 3D architecture of neoplasia lesions and adenocarcinomas, optical clearing is also proven to be an effective histopathology method for pancreatic lesions diagnosis (Hong et al., 2019; Matryba et al., 2019). The choice of different cleating methods depends on the transparency of the tissue, the type of fluorescence, the tolerance of shrinkage, and clearing time (Gómez-Gaviro et al., 2020). Take skeletal muscle as an example, clearing methods enable the observation of connection between various cell types (muscle cells, fibroblasts, and endothelial cells) and changes in myofiber organization during development, regeneration, and other processes (Gómez-Gaviro et al., 2020). CUBIC has been reported for a Duchenne muscular dystrophy study in mouse muscle (Bozycki et al., 2018). In GFP+ skeletal muscle, while preserving the endogenous GFP signal (Pax3-Cre/ZsGreen1+ transgenic mice), musculature can be seen through the skin of the foot after clearing (Calve et al., 2015). Clearing methods 3DISCO, CUBIC, FDISCO, FRUIT, SeeDB, and ScaleS have been used to study interfaces between peripheral nerves and muscle fibers (Yin et al., 2019).

Nonetheless, not all clearing methods are compatible with immunostaining (Hou et al., 2015), and for those techniques, tissue penetration and fluorescent signal attenuation are of concern (Richardson & Lichtman, 2015). Moreover, most clearing techniques were not designed to visualize the organization of the ECM fibrils within intact tissues (Acuna et al., 2018). Thus, it is critical to develop decellularization methods that use mild detergents to remove cellular inference while preserving the 3D organization of the ECM proteins simultaneously (Narayanan & Calve, 2020). To achieve tissue-specific decellularization, physical, chemical, and enzymatic techniques can be used. For example, a clearing method to selectively remove intracellular proteins while leaving behind proteins of the ECM in the native 3D conformation is reported for softer, embryonic tissues by using multiple low-concentration sodium dodecyl sulfates (SDS) washes (Acuna et al., 2018). SDS has shown to achieve adequate cell removal and retain collagens, glycoproteins, and

fiber orientation in multiple tissues, such as aortic heart muscular tissue (Ott et al., 2008) and kidney (Nakayama et al., 2010), and is recognized as a very effective agent for tendon and skeletal muscle decellularization (Cartmell & Dunn, 2000; Gillies & Lieber, 2011; Mendibil et al., 2020; Wilson et al., 2016). Using this method, our lab is able to visualize that proteoglycan-rich fibrils maintain connections between the epidermis and the underlying tendon and cartilage in E12.5 and E14.5 autopods (Acuna et al., 2018). This approach can also be used for the 3D visualization of developing kidney to reveal the intricate architecture of the interstitial matrix (Lipp et al., 2020).

1.2.6 Mechanics of the ECM

For decades, the cellular events based on molecular signaling cascades were well studied, with little consideration for the impact of biomechanical signals from a larger mechanical structure at the tissue level, in which the cells are settled (Peyton et al., 2007). In a wide range of biological processes, such as embryogenesis, tissue morphogenesis, and wound healing, mechanical cues from the environment, including tension, compression and shearing, play a vital role in regulating cell behaviors (Bian, 2014). For example, during chick skeletogenesis, muscle contractility is abrogated after the administration of neuromuscular blocking agents. Then, the induced paralysis further affects bone development, resulting in irregular curvature of neck, spine, and growth of long bone (humerus, femur, tibia) (Hall & Herring, 1990). After neural tube excision, the induced neuromuscular atrophy in the hindlimb of chick embryo leads to a significant short femur and tibiotarsus. The mechanical integrity of the tibiotarsus is altered because of lacking muscle contraction (Wong et al., 1993). Similar muscle contraction-induced effects are also seen in mice. As a result of loss of Myf5 and MyoD, striated muscle is completely absent. The normal growth and development of cervical vertebrae, viscerocranium, humerus, scapula, clavicle, palate, and sternum were substantially compromised (Rot-Nikcevic et al., 2006). Moreover, changes in ECM molecules such as tenascin-C, type XII collagen in immobilized limbs and joints are hypothesized to cause the morphological abnormalities in joint (Bastow et al., 2005; Bian, 2014; Kavanagh et al., 2006; Mikic et al., 2000).

As for the cell-matrix mechanical interactions, cells are usually embedded in an ECM scaffold, which provides cells with structural support and conducts biomechanical signals (Frantz et al., 2010). Cell behaviors, such as migration and division, are a result of the active application of tensile forces on the ECM from cells (Gjorevski et al., 2015; Lesman et al., 2014; Van Helvert et

al., 2018). The importance of the physical properties of the ECM has been demonstrated in many studies. ECM fibers, such as collagen and elastic fibers, have nonlinear viscoelastic properties (Sopher et al., 2018; Wen & Janmey, 2013), including strain-stiffening behavior under tensile load (Han et al., 2018) and microbuckling under compression (Notbohm et al., 2015). This nonlinearity enables cell-applied forces to spread far into the matrix, and allows cells to detect distant boundaries and neighbors (Humphries et al., 2017; Rudnicki et al., 2013). On a linear elastic substrate, a shorter range of force propagation and limited sensing of neighbors are shown, which then result in significant matrix densification and increased fiber alignment (Reinhart-King et al., 2008; Vader et al., 2009). The aligned fibers with increased density further mechanically couple distant cells and control cellular behaviors, such as directing cells to one another (Vader et al., 2009), enhancing cell communication by introducing stiffness gradients (Kim et al., 2017). Such matrix bands also dramatically speed up the transport of molecules released by distant cells (Gomez et al., 2019). Moreover, time-specific changes in matrix elasticity during development have also been demonstrated to have a key role in directing progenitor cell fate (Young & Engler, 2011).

1.2.7 ECM fiber-network modeling

Fiber networks of ECM are critical for maintaining the integrity and viscoelasticity of tissues and organs (Dhume & Barocas, 2017). Most research on the mechanical behavior of ECM remodeling has been carried out almost exclusively in collagen gels, the most abundant fibrous protein of connective tissues and ECM (Natan et al., 2020). For example, in 3D collagen gels, the traction forces from the cells generate the strains remodel the matrix significantly and irreversibly. Computational modeling suggests that the plasticity of the network is due to the irreversible dynamics of cross-links and fiber entanglement (Kim et al., 2017), In addition to collagen gels, fibrin, a commonly used extracellular biopolymer, polymerizes into a hydrogel. In response to injury, blood circulating fibrinogen is cleaved by thrombin, leading to the formation of a fibrin matrix. Later, fibroblasts migrate to this predominant structural component of blood clots, start the healing process, and contract the wound (Smithmyer et al., 2014). Mechanically speaking, fibrin clots have extraordinary extensibility, viscoelasticity, and negative compressibility, and can preserve permeability and bulk structural integrity following cellular contraction and proteolytic degradation (Brown et al., 2009; Kotlarchyk et al., 2011). Also, fibrin influences long-range force

transmission and cell mechanosensing (Wang et al., 2015). The mechanical behaviors of fibrin have been studied at the scale of individual fibers (Guthold et al., 2004; Hudson et al., 2010), 2D fiber networks (Hudson et al., 2010), and within macroscale cubic gels (Ryan et al., 1999). In general, the unique macroscopic mechanical responses of the cross-linked fibrin network are modulated by the microstructure configurations (properties of single fiber and their ensembles), including fiber orientation, curvature, length, diameter, volume fraction, and their bending, stretching, and buckling behaviors (Lin & Gu, 2015; Litvinov & Weisel, 2017). The properties of individual fibrin fibers are dependent on the number of double-stranded half-staggered protofibrils and their packing arrangements (Litvinov & Weisel, 2017).

Computational models of randomly distributed fibers are broadly used to investigate the behaviors of fibrillar networks (Stylianopoulos & Barocas, 2007). Crosslinks in the model are represented as nodes (intersection points), that are connected to one another by links. Basically, a network is determined by which nodes are attached to which links, and by which links are bound to which nodes (Dhume & Barocas, 2017). Fibers, that support tension or compression load, are crosslinked at nodes that are constrained either as pinned rotating joints (Black et al., 2008; Heussinger et al., 2007) or welded joints (Onck et al., 2005; Shahsavari & Picu, 2012). Each polymer fiber at crosslinks can be represented by either regular thin and long fiber (Stylianopoulos & Barocas, 2007) or spring (Ritter et al., 2009).

A fundamental challenge in network modeling of biomechanics is accounting for network effects within a large biological system (Dhume & Barocas, 2017). To do so, some assumptions are required. For example, fibers are connected at freely rotating joints in the network making up the tissue. Moreover, the network is assumed to be statistically homogeneous and at mechanical equilibrium (Dhume & Barocas, 2017). A typical construct of the multiscale method is a representative volume element (RVE) at every integration point of a finite element (FE) model at the macroscopic scale (Cheng et al., 2006). To pass information between the microscopic and the macroscopic scale, the RVE is assumed to be small compared to the finite element dimensions, and the displacement of the boundary nodes in for each RVE is given by the macroscopic displacement field (Sab, 1992). For each RVE, its mechanical equilibrium is given by solving all the nodal force balance at the same time. The multiscale problem is solved using Newton iteration, and the algorithm has the following steps: applying boundary conditions and making an initial guess for the displacements of nodes; deforming RVEs based on the element; solving RVE force

balance; passing stress up to the FE solver. This procedure repeats until convergence is reached at all microscopic and macroscopic calculations (Dhume & Barocas, 2017). Due to the computational cost of running this type of nested models, simulations of individual RVE's are common to understand the overall behavior of a network, but the FE model usually works with a homogenized constitutive model that takes a simple analytical form (Kouznetsova et al., 2001; Perdahcioğlu & Geijselaers, 2011).

2. HYALURONIC ACID, CD44, AND RHAMM REGULATE MYOBLAST BEHAVIOR DURING EMBRYOGENESIS

The content presented in this chapter is adapted from our work “Hyaluronic acid, CD44 and RHAMM regulate myoblast behavior during embryogenesis”, which was published in Matrix Biology. Minor edits to the formatting have been made to produce a cohesive dissertation. The published version of this chapter is available at the following link:
https://doi.org/10.1016/j.matbio.2018.08.008.

2.1 Abstract

Hyaluronic acid (HA) is an extracellular matrix (ECM) component that has been shown to play a significant role in regulating muscle cell behavior during repair and regeneration. For instance, ECM remodeling after muscle injury involves an upregulation in HA expression that is coupled with skeletal muscle precursor cell recruitment. However, little is known about the role of HA during skeletal muscle development. To gain insight into the way in which HA mediates embryonic myogenesis, we first determined the spatial distribution and gene expression of CD44, RHAMM and other HA related proteins in embryonic day (E)10.5 to E12.5 murine forelimbs. While HA and CD44 expression remained high, RHAMM decreased at both the protein (via immunohistochemistry) and RNA (via qPCR) levels. Next, we determined that 4-methylumbelliferone-mediated knockdown of HA synthesis inhibited the migration and proliferation of E11.5/E12.5 forelimb-derived cells. Then, the influence of CD44 and RHAMM on myoblast and connective tissue cell behavior was investigated using antibodies against these receptors. Anti-RHAMM, but not anti-CD44, significantly decreased the total distance myogenic progenitors migrated over 24 hrs, whereas both inhibited connective tissue cell migration. In contrast, anti-CD44 inhibited the proliferation of connective tissue cells and muscle progenitors, but anti-RHAMM had no effect. However, when myoblasts and connective tissue cells were depleted of CD44 and RHAMM by shRNA, motility and proliferation were significantly inhibited in both cells indicating that blocking cell surface-localized CD44 and RHAMM does not have as pronounced effect as global shRNA-mediated depletion of these receptors. These results show, for the first time, the distribution and activity of RHAMM in the context of skeletal muscle.

Furthermore, our data indicate that HA, through interactions with CD44 and RHAMM, promotes myogenic progenitor migration and proliferation. Confirmation of the role of HA and its receptors in directing myogenesis will be useful for the design of regenerative therapies that aim to promote the restoration of damaged or diseased muscle.

2.2 Introduction

In vertebrates, appendicular skeletal muscle is derived from the somites, which are ball-like clusters of mesodermal precursor cells that form along the anterior-posterior axis of the embryo. In the developing limb, muscle progenitors delaminate from the dorsal portion of the somite (dermomyotome) and migrate into the forelimb bud between embryonic day (E)9.5 and E10.5 (Buckingham et al., 2003). These progenitor cells, or myoblasts, further differentiate into mononuclear myocytes, begin expressing myosin heavy chain isoforms and fuse into contractile, multi-nucleated myofibers (Biressi et al., 2007). A distinct population of myogenic precursor cells, called satellite cells, remain on the surface of the myofibers in a quiescent undifferentiated state (Chargé & Rudnicki, 2004). The organization of these progenitors into a functional assemblage of limb muscles involves four successive phases of myogenesis (Biressi et al., 2007). Embryonic myogenesis (E10.5-E12.5; E, embryonic day) gives rise to the basic pattern. Fetal myogenesis (E14.5–birth) and neonatal myogenesis (P0–P21; P, postnatal day) are crucial for growth and maturation. Finally, adult myogenesis (P21 and later) occurs to restore functionality after injury. Each phase involves migration, proliferation, differentiation, and fusion of myogenic precursors into multinucleate myofibers. A number of biochemical and mechanical factors are important regulators during myogenesis. In particular, it has been demonstrated that the surrounding connective tissue directs the organization of muscle in the developing limb (Mathew et al., 2011; Vallecillo-García et al., 2017). The connective tissue is primarily comprised of fibroblasts and the extracellular matrix (ECM) these cells secrete (Mathew et al., 2011; Vallecillo-García et al., 2017); however, the exact composition of the ECM and how it directly regulates embryonic myogenesis remains unknown.

ECM in adult skeletal muscle can be classified into two layers: a basement membrane that surrounds individual myofibers and an interstitial matrix that fills the intercellular spaces (Grounds, 2008). The basement membrane is comprised of a basal lamina, primarily made up of type IV collagen and laminin, and a type VI collagen-containing fibrillar reticular lamina that links the

basal lamina to the interstitial matrix (Bosman & Stamenkovic, 2003; Sanes, 2003). The interstitial matrix consists of fibrillar collagens, elastin, proteoglycans, fibronectin, and hyaluronic acid (HA) (Calve et al., 2010; Grounds, 2008; Okita et al., 2004). During muscle repair and regeneration, the ECM undergoes significant remodeling. There is a transient upregulation of tenascin-C, fibronectin, and HA, which have been shown to facilitate the scar-free restoration of the musculature (Calve et al., 2010, 2012). It is likely that similar ECM remodeling occurs during muscle development as it has been shown that HA is highly expressed in the developing limb and participates in various aspects of morphogenesis (Matsumoto et al., 2009; Solis et al., 2012; Andrew P Spicer & Tien, 2004). During the early stages of limb bud outgrowth, HA is prominent at sites where cell migration occurs (Camenisch et al., 2000), and enhances mesenchymal cell migration and division (Knudson, 2003; Solis et al., 2012). Moreover, conditional inactivation of HAS2 within the limb mesoderm revealed an important role for HA in regulating skeletal growth, patterning, chondrocyte maturation, and joint formation in developing limbs (Matsumoto et al., 2009); however, the effect of HA on the behavior of myogenic progenitors is unclear.

HA is a negatively charged, linear glycosaminoglycan that is found throughout the ECM of all vertebrate tissues, on the cell surface, and even inside cells (Dicker et al., 2014). Individual HA molecules are typically made up of 2,000 to 25,000 disaccharides, with a high molecular weight of 10^6–10^7 Da and extended molecular lengths of 2 to 25 μm (Toole, 2004). These characteristics help regulate the hydration and viscosity of HA-containing tissues and contribute directly to the remodeling and cellular events that drive embryonic morphogenesis, tissue regeneration, and tumorigenesis (Itano, 2008; Tolg et al., 2017). Through interactions with HA-binding proteoglycans (*e.g.* aggrecan and versican), HA maintains extracellular and pericellular matrix structural integrity via provision of a hydrated zone which facilitates cellular invasion during development and tissue remodeling (Dicker et al., 2014; Toole, 2001).

In addition, HA acts as a signaling molecule and mediates cellular behavior by binding to cell surface receptors, including the cluster of differentiation 44 (CD44) (Aruffo et al., 1990) and the receptor for HA-mediated motility (RHAMM) (Hardwick et al., 1992; Turley et al., 2002). CD44 is an ubiquitous, multi-domain cell surface glycoprotein that is considered to be the principal HA receptor (Aruffo et al., 1990). The N-terminal extracellular "link module" directly binds to HA. The C-terminal cytoplasmic tail is important for CD44-mediated intracellular signal transduction (Dzwonek & Wilczynski, 2015; Ponta et al., 2003). Cell type, cytoplasmic tail phosphorylation

and receptor clustering affect the activation state of CD44 and subsequently binding with HA (Isacke & Yarwood, 2002). HA-CD44 binding influences diverse processes, including cell–cell and cell-matrix adhesion, cell migration during development, inflammation, tumor growth, and metastasis (Lesley et al., 1993; Misra et al., 2015). In particular, the interaction between HA and CD44 is required for early adhesive cell–cell interactions of limb bud mesenchyme during limb bud outgrowth (Maleski & Knudson, 1996). CD44 also regulates growth and tissue integrity by mediating the cellular uptake and degradation of HA (Kaya et al., 1997; Knudson et al., 2002).

RHAMM (also known as CD168) (Hardwick et al., 1992), an acidic, coiled-coil protein expressed by many cell types, localizes to the nucleus, cytoplasm, and cell surface (Maxwell et al., 2008). It is thought that RHAMM binds HA via a BX7B motif on the -COOH terminus (Toole, 2001; Yang et al., 1994). Nuclear RHAMM, when bound to extracellular signal-regulated kinase 1/2 (ERK1/2) and mitogen-activated protein kinase (MEK), participates in cell motility and inflammation (Tolg et al., 2014). Cytoplasmic RHAMM interacts with microtubules and actin filaments in the cytoskeleton either directly, or through binding with microtubule- and centrosome-related proteins, to affect cell polarity and direct cell migration (Assmann et al., 1999; Silverman-Gavrila et al., 2011; Tolg et al., 2014). Extracellular RHAMM influences cellular transformation and cell migration during tissue injury and repair in a HA-dependent manner (Turley et al., 2002). In addition, RHAMM interacts with CD44, HA, and growth factors to activate protein tyrosine kinase signaling cascades that activate the ERK1,2 –MAP kinase cascade, which increases random motility (Tolg et al., 2014).

Although RHAMM and CD44 can participate independently in regulating cellular behaviors, their relative contributions are not clearly understood. When knocked out *in vivo*, these receptors have redundant or overlapping functions that can compensate for each other as evidenced by the viability of CD44-knockout and RHAMM-knockout mice (Nedvetzki et al., 2004; Schmits et al., 1997; Tolg et al., 2003). For example, in a collagen-induced arthritis model, the development of arthritis depended on CD44 in wild-type mice. However, in CD44-knockout mice, RHAMM expression was upregulated to compensate for the loss of CD44 and the induction of arthritis was RHAMM-dependent (Nedvetzki et al., 2004). Muscle repair is also influenced by CD44, wherein CD44-knockout mice show delayed repair in a tibialis anterior injury model (Mylona et al., 2006). Subsequent *in vitro* studies with myoblasts isolated from these mice indicated that lack of CD44 negatively influenced cell migration and differentiation (Mylona et al., 2006). Although many

studies have shown RHAMM binds to HA to mediate cell migration (Gouëffic et al., 2006; Tolg et al., 2006), to date there have been no investigations into the role of RHAMM in skeletal muscle. Moreover, the relative contribution of the two types of HA receptors and the intracellular signaling pathways involved in HA-mediated effects in myogenesis remain unknown.

To investigate the role of HA, RHAMM and CD44 in myogenesis, we used the mouse forelimb as a model system. We hypothesized that HA instructs myogenic progenitor cell migration and proliferation by interacting with the receptors RHAMM and CD44. First, the distribution of all three molecules was visualized in the context of embryonic myogenesis *in vivo* using Pax3-Cre/ZsGreen1+ mice in which myogenic progenitors are GFP+. The gene expression of HA, RHAMM, and CD44, as well as the hyaluronic acid synthases (HAS1 – 3) and hyaluronidases (HYAL1 – 4), were compared between GFP+ myoblasts and the surrounding GFP- connective tissue cells. Then, the influence of endogenous HA on myoblast proliferation and migration was investigated *in vitro* using the HA polymerization inhibitor 4-methylumbelliferone (4MU). Antibodies against CD44 and RHAMM were used to specifically block the interaction of HA with these receptors to determine the role of each on myogenesis. Finally, CD44 and RHAMM were depleted using shRNA to further confirm their function. We found that CD44 and RHAMM have functional overlap in modulating cell behaviors and both receptors regulate motility and proliferation of myoblasts and connective tissue cells.

2.3 Materials and Methods

Unless otherwise specified, all reagents were of cell culture grade from Sigma-Aldrich.

2.3.1 Tissue acquisition

All murine experiments were approved by the Purdue Animal Care and Use Committee (PACUC; protocol #1209000723). PACUC ensures that all animal programs, procedures, and facilities at Purdue University adhere to the policies, recommendations, guidelines, and regulations of the USDA and the United States Public Health Service in accordance with the Animal Welfare Act and Purdue's Animal Welfare Assurance. Pax3-Cre (Engleka et al., 2005) and ROSA-ZsGreen1 transgenic mice (Soriano, 1999) were obtained from the Jackson Laboratory (Bar Harbor, ME, USA) and used to generate Pax3-Cre/ZsGreen1+ embryos in which all Pax3-

expressing cells and their progeny are GFP+. Within the forelimb, the majority of GFP+ cells are of the skeletal muscle lineage (>90%), whereas the remainder are endothelial cells (Hutcheson et al., 2009). Males heterozygous for the Pax3-Cre transgene were time-mated with females homozygous for ROSA-ZsGreen1 and noon on the day a copulation plug was found was designated as embryonic day (E)0.5. E10.5-E12.5 Pax3-Cre/ZsGreen1+ embryos were harvested from dams euthanized via CO_2 inhalation followed by cervical dislocation. The embryos were transferred to sterile phosphate-buffered saline (PBS) on ice prior to processing for immunohistochemistry or cell culture.

2.3.2 Cryosectioning and immunohistochemistry

Pax3-Cre/ZsGreen1+ embryos were fixed in 4% paraformaldehyde (PFA) for 1 hr, washed with PBS 3×30 min before embedding in Optimal Cutting Temperature compound (OCT, Sakura Finetek). Embryos were then frozen in dry ice-cooled isopentane (Fisher Scientific) and stored at −80°C until sectioning. Serial, 10 μm-thick cryosections were collected and stored at -20°C. Before staining, sections were washed with PBS for 5 min to remove any residual OCT. Each section was fixed in 4% PFA for 5 min and rinsed with PBS. Then, sections were blocked for 30 min [blocking buffer: 10% donkey serum (Lampire), 0.2% bovine serum albumin, 0.02% sodium azide in PBS]. To label HA, biotinylated hyaluronic acid binding protein (HABP; 4 μg/ml, Calbiochem, 385911) was used as described previously (Calve et al., 2010). Sections were incubated with HABP, and primary antibodies against RHAMM (33.3 μg/ml, abcam, ab185728), CD44 (33.3 μg/ml, Invitrogen, MA4405), Pax7 (13.3 μg/ml Developmental Studies Hybridoma Bank) and Tcf4 (50 μg/ml, Millipore, 05-511) at 4°C overnight, and washed with PBS for 3×5 min. Slides were blocked again for 10 min before staining with the appropriate secondary detection reagents [DyLight 550 anti-rat (1:250, Invitrogen), Alexa Fluor 546 anti-rabbit (1:500, Invitrogen), Alexa Fluor 546 Goat anti-Mouse IgG1 (1:500, Invitrogen), Alexa Fluor 647 anti-rabbit (1:500, Invitrogen), Alexa Fluor 647 Goat anti-Mouse IgG2a (1:500, Invitrogen), Alexa Fluor 647 streptavidin (1:500, Invitrogen), DAPI (1:500, Roche)] for 30 min. Sections were imaged at 5×, 10×, and 20× using a Leica DMI6000 inverted microscope and at 63× using a Zeiss 800 confocal microscope. Images were acquired using the same imaging parameters across the different time points or treatments, and processed under identical conditions using ImageJ (NIH).

2.3.3 Forelimb cell harvest and sorting

Forelimb buds from E10.5 – E12.5 Pax3-Cre/ZsGreen1+ embryos were removed with micro scissors. Forelimb buds from 2 – 3 animals were placed in a microcentrifuge tube, washed twice with PBS and incubated with 250μL pre-warmed 0.1% trypsin solution (2.5% HyClone trypsin protease, containing 0.2 g/L EDTA, diluted with PBS) at 37°C for 5 min. Limb buds were dissociated by pipetting up and down using a 200 μL tip. After inactivating the trypsin using growth medium [Dulbecco's modified Eagle's medium with L-glutamine (DMEM; Gibco) with L-glutamine, 10% fetal bovine serum (FBS; Gibco), 1% Pen/Strep/Fungiezone], the cell suspension was filtered through a 70μm strainer to remove large aggregates. Cells were centrifuged to remove the trypsin solution, resuspended in growth medium, stained with Trypan blue to identify dead cells and viable cells were counted by hemocytometer. To separate GFP+ and GFP- cells, samples were sorted using a FACS Aria III Cell Sorter (BD Biosciences, San Diego) at the Purdue University Center for Cancer Research (Bindley Bioscience Center). Isolated cells were expanded in culture for 2 days in DMEM+10% FBS growth medium, supplemented with 4 ng/mL basic fibroblast growth factor (PeproTech), before performing the following assays.

2.3.4 Cell culture

Cells were cultured *in vitro* using one of the following media: DMEM medium [DMEM with L-glutamine, 1% Pen/Strep/Fungiezone (HyClone)]; DMEM+10%FBS [DMEM with L-glutamine, 10% FBS, 1% Pen/Strep/Fungiezone], and adv DMEM [advanced DMEM (Gibco), 1% Pen/Strep/Fungiezone, 1% L-Glutagro (Corning)] at 37°C in 5% CO_2.

4MU treatment: 4-methylumbelliferone (4MU, Alfa Aesar) was dissolved in dimethyl sulfoxide (DMSO) to generate 0.5M and 1M stock solutions. For both migration and proliferation assays, cells were seeded on a 96-well plate at the density of 2×10^4 cells/cm^2 with 0mM, 0.5mM, or 1.0mM 4MU added to the growth medium, each having a final concentration of 0.1% DMSO.

Antibody treatment: Cells were seeded at 2×10^4 cells/cm^2 for 24 hrs before adding antibody-containing medium [100 μg/mL of anti-CD44, anti-RHAMM, rat IgG2b (Invitrogen), and rabbit IgG (Invitrogen) isotype controls or cell growth medium alone (blank control)]. After confirming that there is no difference between rat IgG2b and rabbit IgG as isotype controls in proliferation and migration assays, cells treated with rat IgG2b were used for normalization (denoted by IgG),

whereas for qPCR and ERK1/2 signaling, cells simultaneously treated with both isotype controls were used for normalization (denoted by IgGs).

2.3.5 Quantitative RT-PCR

Total RNA was extracted from either freshly sorted E10.5-E12.5 forelimb GFP+/- cells or GFP+/- cells after 24 hrs antibody treatment using a RNeasy Mini Kit (QIAGEN) according to the manufacturer's protocol. RNA concentrations were measured using a NanoDrop (Thermo Scientific), and nucleic acid purity was monitored by confirming the A260:A280 ratio was ~2.0. Equal amounts of total RNA were reverse-transcribed with a iScript cDNA synthesis kit (Bio-Rad). cDNA generated from 3 ng of RNA was combined with primers for genes of interest (Table 2.1) and SsoAdvanced Universal SYBR Green Supermix (Bio-Rad). Quantitative PCR was performed using a CFX96 real-time thermal cycler (Bio-Rad) with a program of 3 min at 95°C for enzyme activation, followed by 40 cycles with 10 s denaturing at 95°C and 30 s at 54°C or 55°C (depending on the primer pair) for annealing. The presence of single amplicons was validated by performing a melt-curve analysis. Target genes were normalized to the housekeeping gene β-actin. Expression of β-actin was constant across the time points investigated in this study. Fold change in gene expression was calculated by determining ΔΔCq values.

Table 2.1. Primers used for RT-PCR analyses of mRNA expression

Gene	Forward Primer 5′-3′	Reverse Primer 5′-3′	Size, bp	Ref Seq
CD44	ACCAAATGAAGTTGGCCCTGA	TCTTCTTCAGGAGGGGCTGAG	196	NM_009851.2
RHAMM	CCTTGCTTGCTTCGGCTAAAA	CTGCTGCATTGAGCTTTGCT	189	NM_013552.2
HAS1	GAGGCCTGGTACAACCAAAAG	CTCAACCAACGAAGGAAGGAG	158	NM_008215.2
HAS2	GAGCACCAAGGTTCTGCTTC	CTCTCCATACGGCGAGAGTC	154	NM_008216.3
HAS3	TGGACCCAGCCTGCACCATTG	CCCGCTCCACGTTGAAAGCCAT	156	NM_008217.4
Hyal1	TCATCGTGAACGTGACCAGT	GAGAGCCTCAGGATAACTTGGATG	98	NM_008317.4
Hyal2	GCAGGACTAGGTCCCATCATC	TTCCATGCTACCACAAAGGGT	116	NM_010489.2
Hyal3	TCTGTGGTATGGAATGTACCCT	TGCACACCAAAATGGGCCTTA	53	NM_178020.3
Hyal4	ATGCAACTATTGCCTGAAGGAC	GGAAGTCGGGCAGGTTTTAGG	122	NM_029848.1
Actb	CGACAACGGCTCCGGCATGT	CTAGGGCGGCCCACGATGGA	87	NM_007393.3

CD44 and RHAMM primers were designed using Primer-BLAST (NIH). Other primers were taken from (Calve et al., 2012).

2.3.6 Cell migration assay

The influence of 4MU or anti-CD44 and anti-RHAMM antibodies on the migration of GFP+ and GFP- cells was determined by imaging cultures every hour for 24 hrs at 37°C, 5% CO_2 on a Leica DMI6000 fluorescence live cell microscope. The total distance individual cells traveled was determined by using the Manual Tracking plugin in ImageJ. For each biological replicate, the influence of individual treatments on migration was averaged from three wells. The results are presented as a mean of n = 3 biological replicates ± S.E.

2.3.7 Cell proliferation assay

To analyze proliferation, cells cultured with either 4MU or antibodies were incubated with 5µM 5-ethynyl-2´-deoxyuridine (EdU; ThermoFisher) for 24 hrs. 10 mM EdU stock solution was prepared in DMSO, then further diluted in growth medium to 5µM. Cells were fixed and stained for EdU incorporation using a ThermoFisher Click-iT Plus EdU kit and co-stained with DAPI. Proliferation was expressed as the percentage of EdU+ nuclei relative to the total number of nuclei analyzed. For each biological replicate, the influence of individual treatments on proliferation was averaged from three wells. The results are presented as a mean of n = 3 biological replicates ± S.D.

2.3.8 Analysis of ERK1,2 Activation

For quantification of serum induced ERK1,2 activation after antibody treatment, isolated GFP+ cells were seeded on a 96 well plate for at least one day, serum starved for 5 hrs, incubated with primary antibodies as described above for 30 min then stimulated with 10% FBS by directly adding FBS to cultures. An ELISA for ERK1,2 (abcam) was carried out according to the manufacturer's instructions. For each biological replicate, the influence of individual treatments on ERK1,2 phosphorylation was averaged from three wells. The results are presented as a mean of n = 3 biological replicates ± S.D. The ratio of phospho-ERK1,2 protein to total ERK1,2 protein was normalized by IgGs control.

2.3.9 Transduction of cells with scrambled shRNA, shCD44 or shRHAMM

Depeletion of CD44 and RHAMM expression was achieved through TRC lentiviral-mediated transduction of TRCN0000065355 (shCD44-1), TRCN0000065357 (shCD44-2),

TRCN0000071588 (shRHAMM-1), TRCN0000071590 (shRHAMM-2), TRCN0000071592 (shRHAMM-3), or a scrambled control shRNA (GE Dharmacon, Lafayette, CO). Plasmid preparation and replication were conducted following the manufacturer's instructions. Lentiviral particles were produced in HEK-293 cells upon cotransfection with pMD2.G and psPAX2. Viral particle-containing supernatants were diluted 1:1 in growth medium. GFP+ and GFP- cells were transduced with lentiviral particles for 48 hrs in the presence of 5 μg/mL polybrene. After transduction, cells were allowed to recover for 24 hrs. In all cases, stable genomic integration of constructs was selected for using 1.25 μg/mL puromycin (Sigma-Aldrich, St. Louis, MI) for 10 days before conducting migration or proliferation assays. Gene depletion was verified by immunoblotting with antibodies against CD44 and RHAMM and qPCR.

2.3.10 Western blot analysis

Cells were lysed using a modified RIPA lysis buffer containing 50 mM Tris, 150mM NaCl, 0.25% sodium deoxycholate, 1.0% NP40, 0.1% SDS, 10mM activated sodium ortho-vanadate, 40 mM β-glycerolphosphate, 20mM sodium fluoride and protease inhibitor cocktail (Sigma Aldrich, St.Louis, MO). The concentration of protein was determined using the Pierce BCA Protein Assay (Thermofisher Scientific, Rockford, IL). Protein samples were mixed with 4x laemmli buffer and denatured by incubation at 98℃ for 5min. Lysates were separated by reducing SDS P.A.G.E. and transferred to PVDF membranes (Bio-Rad). The PVDF membrane was soaked in methanol, air-dried and incubated with CD44 (Thermofisher Scientific, Rockford, IL), RHAMM (Abcam, Cambridge, MA) or β-tubulin (DSHB, Iowa City, IA) in 5% milk in TBST (10X Tris Buffered Saline with Tween 20) at 4℃ overnight. Membranes were incubated with HRP-coupled secondary antibodies (Sigma Aldrich, St. Louis, MO) for one hour at room temperature. The membranes were washed with TBST and chemiluminescence was detected using home-made ECL Substrate. Image Lab 2017 Version 6.0 (Biorad) was used to quantify western blot bands.

2.3.11 Statistical analysis

Prism 7.0 (GraphPad Software, La Jolla, CA) were used for statistical analysis. One-way ANOVA and two-way ANOVA, followed by Tukey's post hoc analysis ($\alpha = 0.05$) were used to analyze qPCR, migration, proliferation and ERK ELISA data. Error bars represent the S.E. or S.D.

as indicated. Data were normalized by the control (as indicated in each figure) before statistical analyses were performed. A 95% confidence interval was accepted, and adjusted p value was reported, where $0.01 < p \leq 0.05$ was deemed significant (*), $0.001 < p \leq 0.01$ was deemed very significant (**), and $p \leq 0.001$ was deemed extremely significant (***).

2.4 Results

2.4.1 The distribution of CD44, RHAMM and HA spatially and temporally vary during forelimb development

Although HA is known to influence myogenesis (Hunt et al., 2013), the expression, distribution, and function of HA and its receptors CD44 and RHAMM during muscle development have not been fully characterized. To gain preliminary insight into the role that HA and its receptors play in myogenesis, a spatiotemporal map of these components in E10.5-E12.5 murine embryos was generated. Myogenic progenitors were labeled with GFP using embryos heterozygous for Pax3-Cre and ROSA-ZsGreen. Pax3 expression in the limb bud is largely restricted to myogenic progenitors; however, it has also been found in a small subset of endothelial cells that contribute to the vasculature of the limb (Hutcheson et al., 2009). These Pax3+ endothelial cells make up a small fraction of the limb vasculature and are predominantly found in the vessels below the epidermis (Hutcheson et al., 2009). Therefore, the majority of the GFP+ cells within the limb can be considered to be myoblasts.

HA, CD44, and RHAMM were widely distributed throughout the developing limb (Figure 2.1). Mononucleated GFP+ myoblasts migrated from the somites into the early forelimb bud by E10.5, separated into distinct dorsal and ventral muscle masses by E11.5 and started to elongate by E12.5 (Figure 2.1.A, F, K). CD44 was evenly distributed in the forelimb at E10.5 and E11.5 (Figure 2.1.B, G); however, at E12.5, CD44 aggregated around the dorsal (denoted as “d”) and ventral (denoted as “v”) muscle masses (Figure 2.1.L). RHAMM co-localized with the GFP+ muscle progenitor cells at all stages, but the expression decreased from E10.5 – E12.5 (Figure 2.1.C, H, M). HA was broadly distributed throughout the limb and around the myoblasts (Figure 2.1.D, I, N). Interestingly, HA expression was lower in dorsal and ventral muscle masses at E12.5, whereas HA was significantly upregulated around the newly forming joints and the distal tip of the limb (Figure 2.1.N). At higher magnifications, CD44 and RHAMM appeared to colocalize with HA (Figure 2.1.P, R, S, U, Y, X) and the surface of GFP+ muscle cells (Figure 2.1.Q, T, W).

At E12.5, in areas where myoblasts began taking on a more elongated phenotype, CD44 and RHAMM expression decreased (Figure 2.1.W).

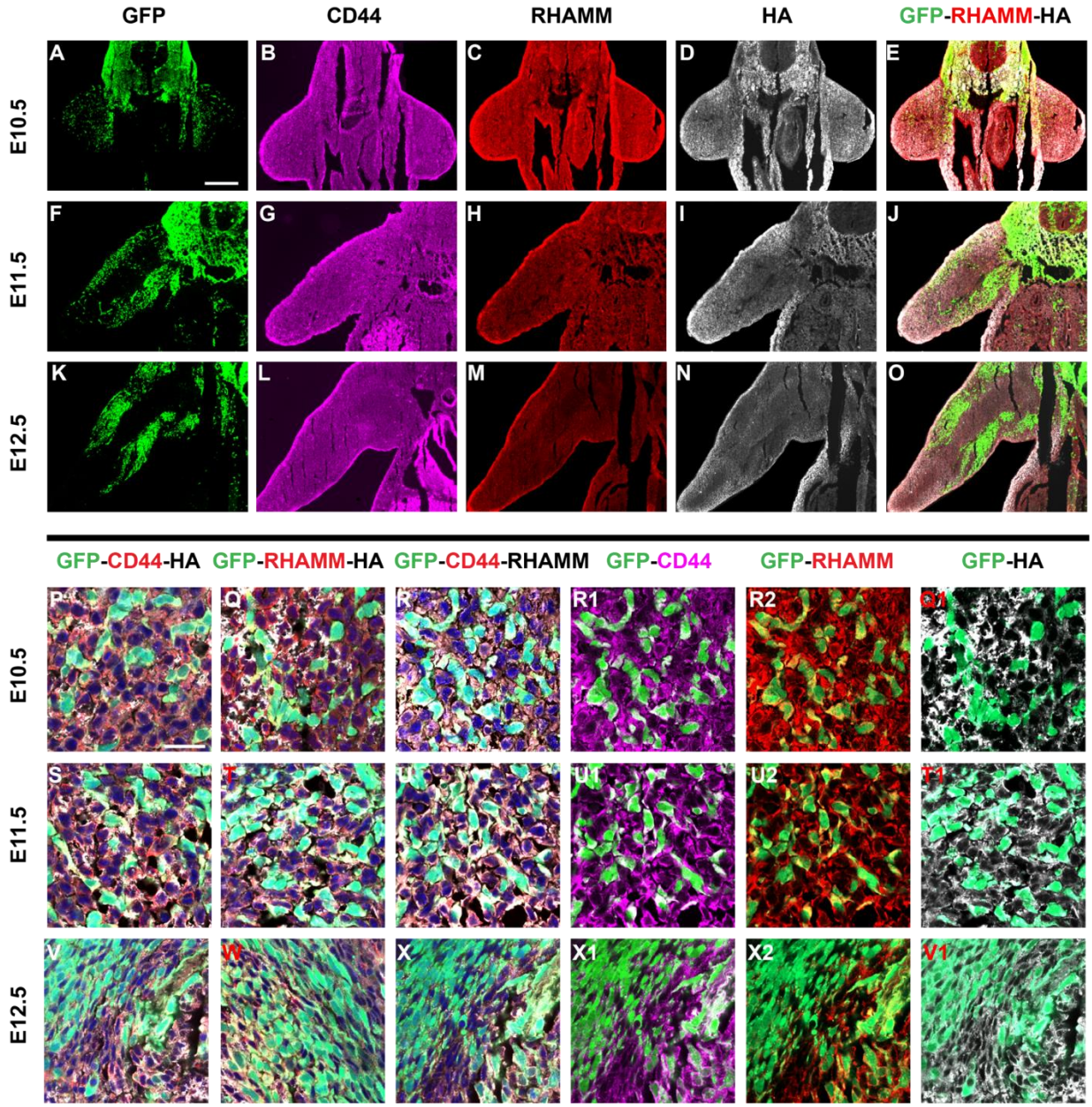

Figure 2.1. The overall distribution of CD44, RHAMM and HA in the developing forelimb from E10.5-E12.5. (A-O) Serial sections of Pax3-Cre:ROSA-ZsGreen E10.5-E12.5 forelimbs were fluorescently labeled for CD44 (magenta), RHAMM (red) and HA (white). 5×, bar = 300 μm. (P-X) Higher resolution images of E10.5-E12.5 forelimb muscles. 63×, bar = 25 μm.

To determine how muscle progenitors and the surrounding connective tissue cells differentially bind to, and regulate the metabolism of, HA during development, gene expression was analyzed using quantitative PCR. Cells from Pax3-Cre/ZsGreen+ E10.5-E12.5 forelimbs were separated into GFP+ and GFP- populations using FACS. Since the connective tissue in the embryo forelimb at these stages is primarily composed of fibroblasts (Mathew et al., 2011), we consider the GFP+ cells to be predominantly muscle progenitors and the GFP- cells to be predominantly fibroblasts. Target gene expression was normalized to the housekeeping gene *β-actin*. *CD44* was broadly expressed in both cell populations with ΔCq in the magnitude of 10^{-1} (Supplemental Figure A. 1). Two-way ANOVA revealed that developmental stage (E10.5/E11.5/E12.5; $p=0.001$) and the interaction between stage and cell type ($p<0.05$) significantly affected *CD44* expression.

The expression of the three HA synthases *HAS1–HAS3* and four hyaluronidases, *Hyal1–Hyal4*, were measured to evaluate how HA deposition was regulated in the developing forelimb. *HAS1* expression in GFP+ cells was significantly influenced by stage (shown by two-way ANOVA, $p<0.01$; Figure 2.2.C). *HAS2* in GFP+ cells was upregulated at E12.5 (Figure 2.2.D). GFP- cells expressed significantly more *HAS3* than GFP+ cells (shown by two-way ANOVA, $p<0.001$; Figure 2.2.E). The overall expression of *HAS2* was greater than the other synthases (Supplemental Figure A. 2.), which is consistent with previous reports describing it to be the predominant HAS during development (Spicer & McDonald, 1998). *Hyal2* was the dominant hyaluronidase expressed in murine forelimb; however, the expression of *Hyal1*, *Hyal2*, *Hyal3*, and *Hyal4* showed no significant difference as a function of developmental stage in either cell population (Figure 2.2, Supplemental Figure A. 2).

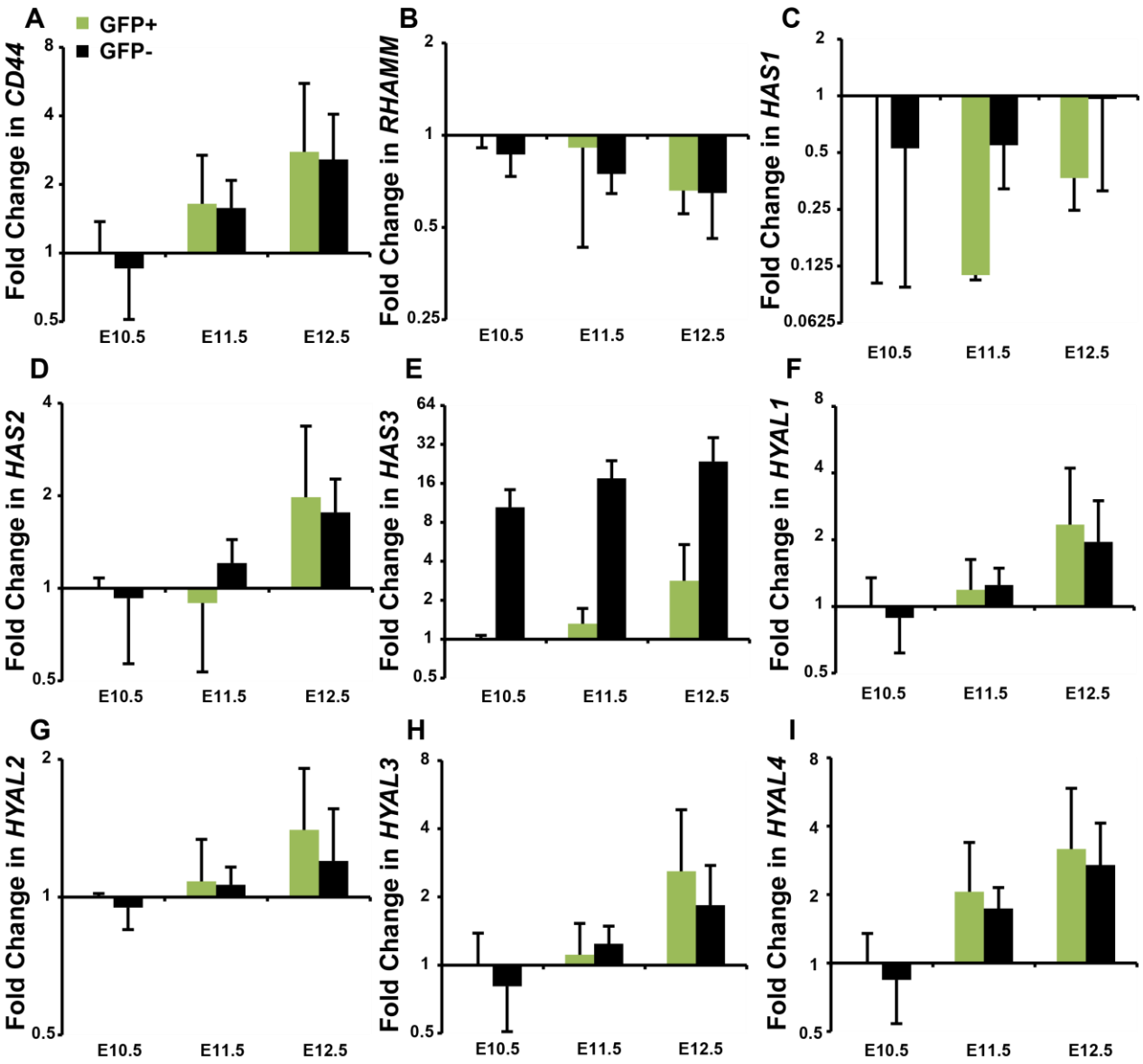

Figure 2.2. Differential expression of HA-related genes during forelimb development. GFP+ and GFP- cells were isolated by FACS and gene expression was analyzed using qPCR. The fold change in different genes was calculated via the ΔΔCq method using ß-actin as a housekeeping gene. To enable comparison between developmental stages, the expression of each gene was normalized to the fold change of E10.5 GFP+ cells. Log_2 scale; geometric mean of n≥3 biological replicates; error bars= S.D.

2.4.2 4MU reduces HA deposition and inhibits migration of embryonic forelimb cells

To investigate the role of endogenous HA in regulating muscle cell migration, we used 4-methylumbelliferone (4MU), an inhibitor of HA biosynthesis (Kakizaki et al., 2004). 4MU decreases HA deposition by depleting UDP-glucuronic acid (UDP-GlcUA), one of the saccharide

precursors for HA, and inhibits the transcription of HAS1 – HAS3 (Vigetti et al., 2009). Primary mesenchymal cells, comprising a heterogeneous population of GFP+ and GFP- cells, were isolated from E10.5/E11.5 Pax3-Cre/ZsGreen+ forelimbs, cultured *in vitro* with 0 – 1.0 mM 4MU, and imaged every hour for 24 hrs using time-lapse microscopy. Three types of culture media (DMEM, DMEM+10%FBS, and adv DMEM, see 2.4.4 for details) were used to exclude the effect of serum on migration. There was no apparent difference in cellular viability or morphology of GFP+ cells incubated in the absence or presence of FBS. For all three media, GFP+ cells co-cultured with 0.5mM 4MU and 1.0mM 4MU migrated significantly slower than the control ($p < 0.0001$; Figure 2.3.A). One-way ANOVA indicated that adding 4MU in all three culture medium significantly influenced GFP+ cells migration ($p<0.0001$). The inhibitory influence of 4MU on HA synthesis was confirmed by labeling with biotinylated hyaluronic acid binding protein (HABP) and indicated that 4MU reduced the deposition of HA in a dosage-dependent manner (Figure 2.3.B).

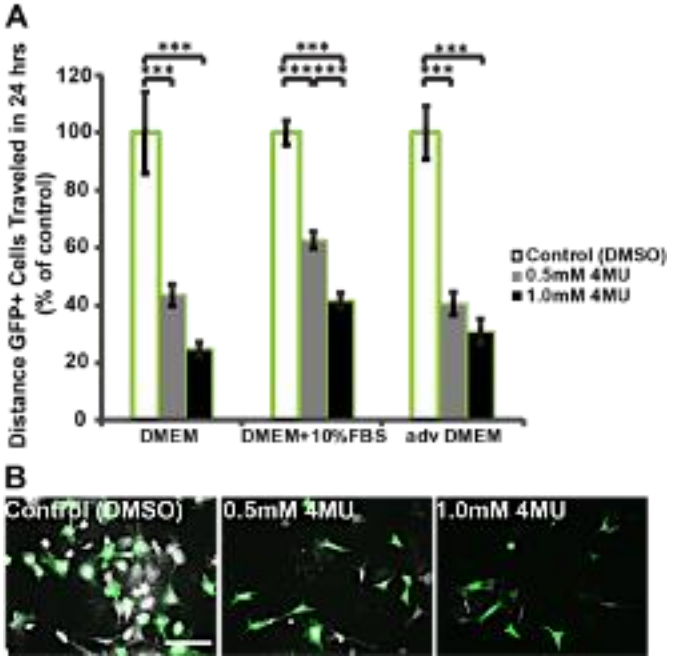

Figure 2.3. 4MU treatment significantly inhibited GFP+ cell migration. A) Cells isolated from E10.5/E11.5 Pax3-Cre/ZsGreen forelimbs were tracked for 24 hrs. ***$p<0.0001$, error bars = S.E.; $n \geq 55$ cells/condition across three biological replicates. B) Confirmation that the deposition of HA (white, HABP), in DMEM+10%FBS medium, was decreased by 4MU treatment. Green = GFP; bar = 100 µm; 20×.

2.4.3 Anti-RHAMM but not anti-CD44 inhibits myogenic progenitor migration

To investigate the involvement of two of the predominant HA receptors, CD44 and RHAMM, in controlling cell migration, the *in vitro* expression of these proteins and the effects of antibodies against CD44 and RHAMM on primary myoblast migration were studied. GFP+ and GFP- cells were isolated using FACS to rule out the influence of reciprocal signaling between the two populations on migration. Cells were cultured in growth medium for at least 16 hrs before adding antibodies to promote the deposition of HA. Then, we performed time-lapse imaging for cells in the presence of IgG control, anti-CD44, anti-RHAMM, or anti-CD44 + anti-RHAMM (all antibody concentrations = 100 μg/ml). Anti-RHAMM and anti-CD44 + anti-RHAMM significantly inhibited GFP+ cell motility ($p<0.0001$) whereas there was no difference between control and anti-CD44 treated cells (Figure 2.4.A). In contrast, both anti-CD44 and anti-RHAMM significantly decreased GFP- cell motility, but no additive effect was observed ($p<0.0001$; Figure 2.4.B). Two-way ANOVA showed that antibody treatment, cell type and their interaction had a significant impact on cell migration ($p<0.0001$). The same trends were observed in unsorted cell populations (Supplemental Figure A. 3). After the initial antibody treatment, a heterogeneous population of cells was treated again with primary antibodies and then stained with secondary labeling reagents to confirm there was no binding of the IgG control and to visualize the distribution of CD44 and RHAMM after 24 hrs antibody treatment. CD44 localized to the membrane in the majority of cells (Figure 2.4.C, E, F, H); however, the distribution and cellular localization of RHAMM was more variable (Figure 2.4.C), consistent with previous descriptions that RHAMM localizes to the nuclear, cytosolic, membrane-bound and extracellular compartments (Maxwell et al., 2008; Pilarski et al., 1994). Both receptors co-localized with HA (Figure 2.4.D, E, G, H). Interestingly, the expression of RHAMM appeared to increase after treatment with anti-RHAMM and anti-CD44 + anti-RHAMM (Figure 2.4.F, G).

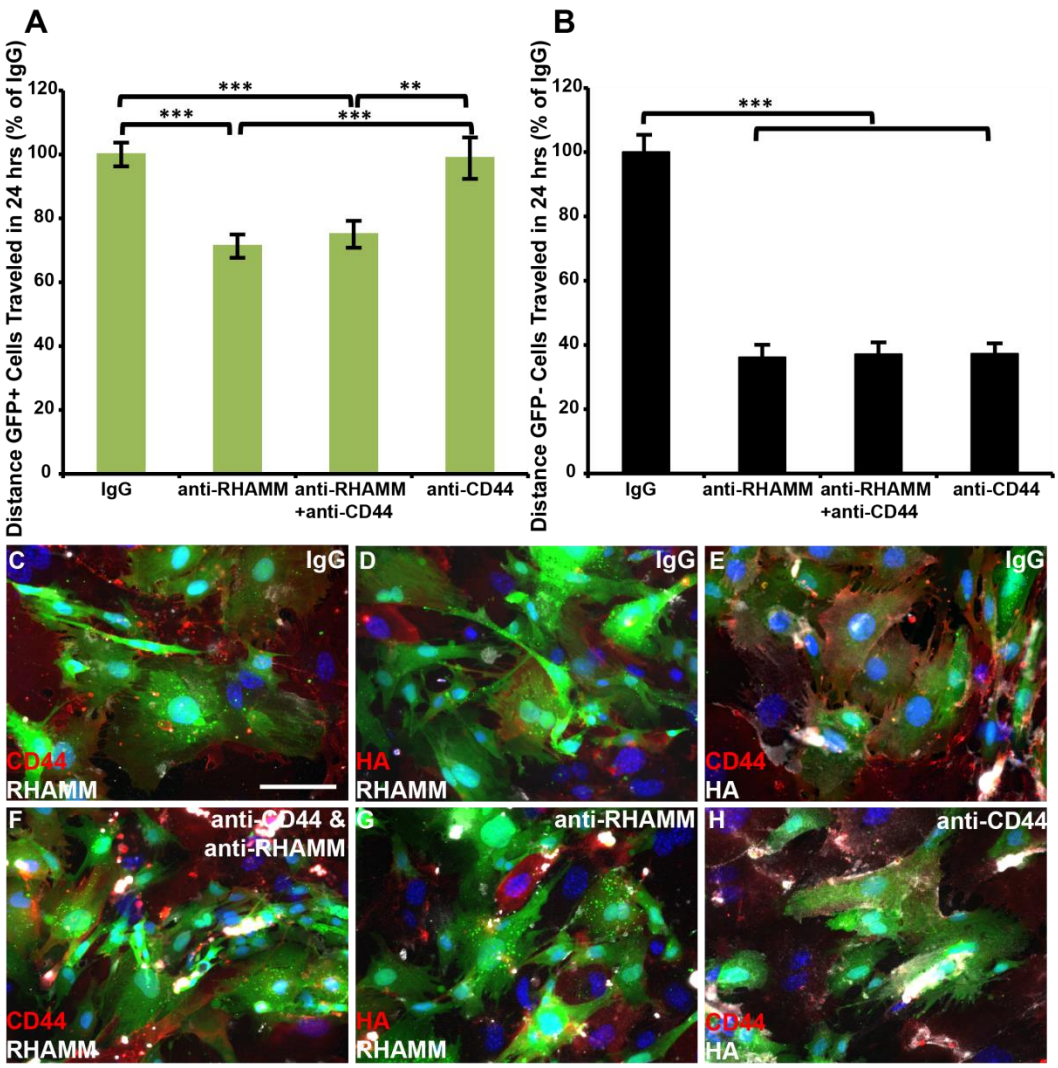

Figure 2.4. The influence of CD44 and RHAMM on migration varies between cell types. A, B) anti-RHAMM significantly decreased the total distance GFP+ cells migrated over 24 hrs, whereas both antibodies inhibited the migration of GFP- cells. (***$p<0.0001$, **$p<0.01$; error bars = S.E; $n \geq 80$ GFP+cells/condition and $n \geq 47$ GFP-cells/condition across the 3 biological replicates). C-H) The expression of HA, CD44 and RHAMM in control and antibody-treated cultures was confirmed by immunofluorescence analysis. Blue = DAPI; green=GFP; bar = 100 µm; 20×.

2.4.4 The transcription of HA-related genes changes after antibody treatment

RHAMM protein expression appeared to increase after treating cells with anti-RHAMM (Figure 2.4.F, G). Thus, we performed qPCR to assess how HA-related genes were affected by treatment with antibodies for 24 hrs (Figure 2.5, Supplemental Figure A. 4). Since *HYAL3* and

HYAL4 were expressed at low levels in the forelimb (Figure 2.2, Supplemental Figure A. 2), we did not include these two genes in this investigation.

For GFP+ cells, incubation with anti-RHAMM and anti-CD44 + anti-RHAMM promoted more *RHAMM* compared to IgG control (Figure 2.5), consistent with the immunohistochemical results (Figure 2.4). One-way ANOVA revealed that adding antibodies significantly influenced *RHAMM* expression in GFP- cells ($p<0.05$). Moreover, we found *CD44* and *HAS2* expression increased with anti-RHAMM and anti-CD44 + anti-RHAMM treatment. Cells upregulated the expression of *HYAL2* in response to anti-CD44 + anti-RHAMM compared with IgGs control (Supplemental Figure A. 4). Consistent with the GFP+ population, GFP- cells expressed more *RHAMM* after incubation with anti-RHAMM and anti-RHAMM + anti-CD44. However, GFP- cells were less affected by antibody treatment when compared to GFP+ cells. *HYAL1* expression was downregulated in anti-CD44 + anti-RHAMM treated cells compared to anti-CD44 (Supplemental Figure A. 4).

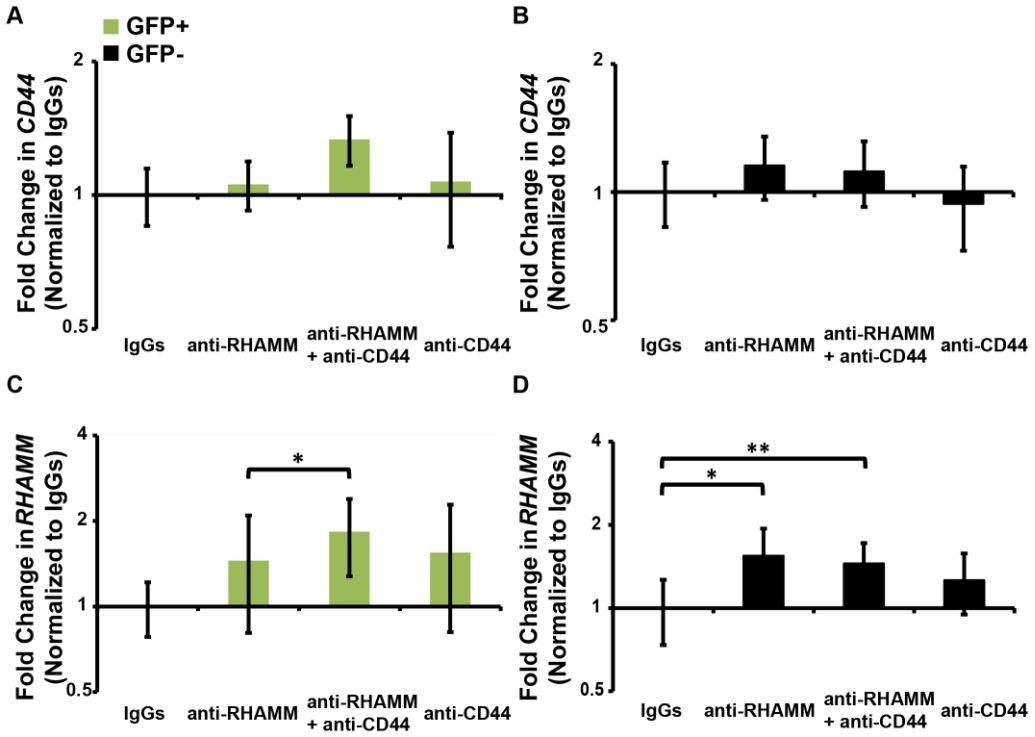

Figure 2.5. Differential expression of HA related genes in GFP+ and GFP- cells after antibody treatment. Geometric means and standard deviation are plotted on a $\log_2$ scale. One-way ANOVA followed by Tukey's post hoc test for assessing significant differences in fold changes between groups; *$p<0.05$, **$p<0.01$; error bars = S.D.; $n \geq 3$.

2.4.5 4MU inhibits proliferation of embryonic forelimb cells

In addition to migration, proliferation is crucial for establishing the musculature in the developing forelimb. To examine the role of HA in supporting cell proliferation, a heterogeneous population of GFP+ and GFP- cells isolated from E10.5/E11.5 forelimbs were cultured *in vitro* with 0mM - 1.0mM 4MU for 24 hrs. During this period of time, cells were also incubated with 5μM EdU to identify cells that have re-entered the cell cycle (Salic & Mitchison, 2008). 4MU significantly decreased EdU incorporation by both GFP+ and GFP- cells in a dose-dependent manner (Figure 2.6). Two-way ANOVA revealed the proliferation rate of GFP+ and GFP- cells were significantly affected by 4MU ($p<0.001$), wherein cell cycle re-entry was affected more in GFP+ cells than GFP- cells ($p<0.0001$).

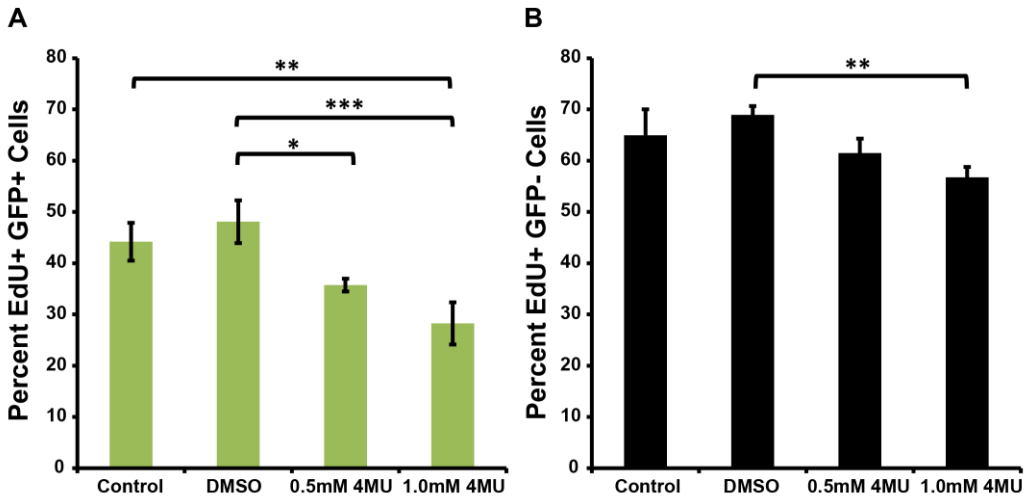

Figure 2.6. 4MU significantly decreased cell cycle re-entry of embryonic forelimb cells. EdU incorporation by GFP+ and GFP- cells over 24 hrs was affected by 4MU in a dose-dependent manner. Two-way ANOVA followed by Tukey's post hoc test, ***$p<0.001$, **$p<0.01$,*$p<05$; error bars = S.D.; $n \geq 7200$ cells/condition across the 3 biological replicates and 3 technical replicates.

2.4.6 Anti-CD44 but not anti-RHAMM inhibits myogenic progenitor proliferation

To examine if CD44 and RHAMM play a role in regulating cell proliferation *in vitro*, GFP+ and GFP- cells isolated using FACS were incubated with 5 μM EdU in combination with anti-CD44, anti-RHAMM, both antibodies or isotype controls for 24 hrs. Antibody treatment significantly affected the proliferation of GFP+ cells (one-way ANOVA, $p<0.05$). For GFP+ cells,

anti-CD44 but not anti-RHAMM inhibited proliferation ($p<0.05$, Figure 2.7). Interestingly, cells incubated in anti-CD44 + anti-RHAMM did not significantly inhibit DNA synthesis.

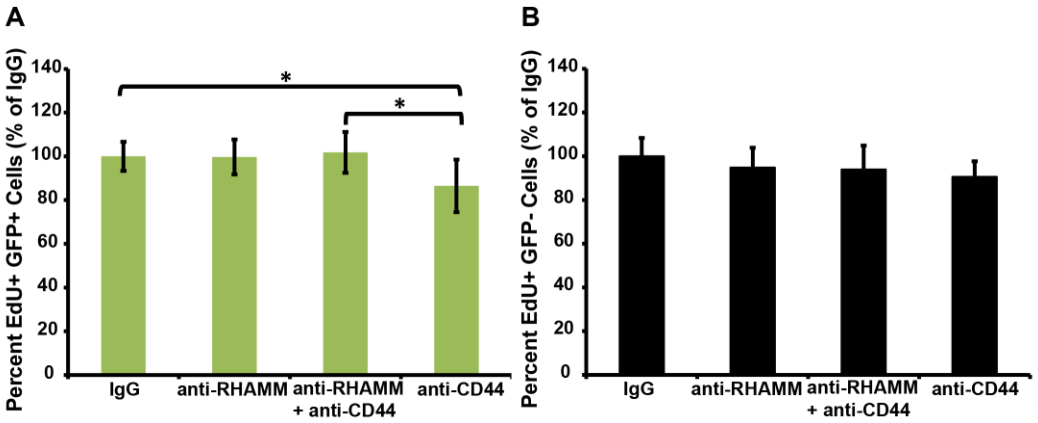

Figure 2.7. Anti-CD44 but not anti-RHAMM significantly affected the proliferation of embryonic forelimb progenitors. GFP+ and GFP- cells, isolated via FACS, were labeled with 5 μM EdU for 24 hrs while incubated with anti-CD44, anti-RHAMM or isotype controls. One-way ANOVA followed by followed by Tukey's post hoc test, *$p<0.05$; error bars = S.D.; n = 8267 GFP- cells and n = 13018 GFP+ cells/condition across the 3 biological replicates.

2.4.7 ERK1,2 phosphorylation in GFP+ myoblasts is affected by anti-CD44 and anti-RHAMM

To determine whether antibody treatment affected ERK1,2 phosphorylation in GFP+ cells, a known downstream effect of HA binding (Hatano et al., 2011; Misra et al., 2015; Tolg et al., 2006), we quantified serum induction of ERK1,2 activity using an ELISA. After stimulation with 10% FBS, ERK1,2 was activated in all the groups, but activity was significantly less in antibody treated cells (one-way ANOVA, $p<0.001$; Figure 2.8). Moreover, there was an additive effect when anti-CD44 and anti-RHAMM were combined. The difference in ERK1,2 activity between groups was not due to a decrease in total ERK1,2 protein levels because the cells in all four groups expressed similar amounts of ERK1,2 protein (data not shown). These results suggest that the activation of CD44 and RHAMM is required for sustaining ERK1,2 activity in culture.

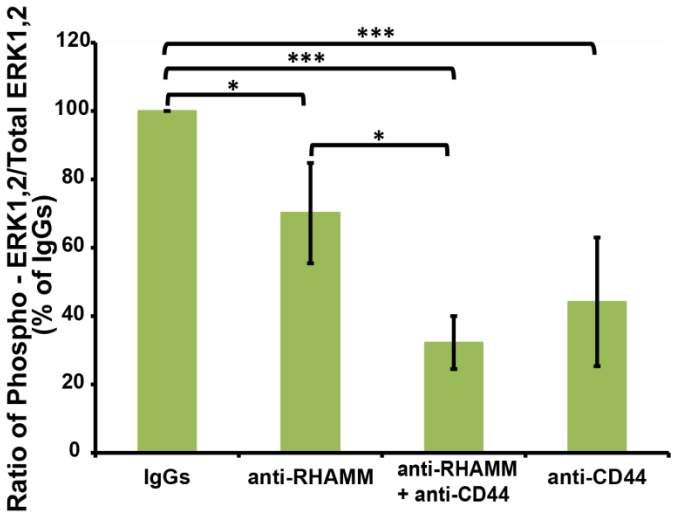

Figure 2.8. Serum-induced ERK1,2 activation in GFP+ cells was inhibited by anti-CD44 treatment and anti-RHAMM. The ratio of phospho-ERK1,2/Total ERK1,2 was measured immediately before and after 30 min serum stimulation. One-way ANOVA followed by Tukey's post hoc test across 3 biological replicates, *$p<0.05$, ***$p<0.001$, error bars = S.D.

2.4.8 shRNA-mediated depletion of CD44 and RHAMM inhibit myogenic progenitor migration and proliferation

Inhibition of CD44 and RHAMM using antibodies led to differential decreases in migration in proliferation, which contrasted with our 4MU results that showed knockdown of HA synthesis affected these cellular behaviors in both cell types. Antibody-blocking experiments may not fully inhibit receptor signaling as it primarily affects receptors located on the cell surface and may not be able to engage all isoforms or receptors within complexes. Therefore, GFP+ and GFP- cells isolated using FACS were transduced with lentiviral particles encoding shRNAs targeting CD44, RHAMM, or a nontargeting, scrambled shRNA as a control. Depletion of CD44 and RHAMM in both cells was verified using immuoblot (

Figure 2.9.A) and qRT-PCR (data not shown). In response to transduction with shCD44 or shRHAMM, both GFP+ and GFP- cells showed a significant decrease in total distance traveled and proliferation rate. For both types of cells, the decrease in cell migration was comparable to that observed after treatment with 4MU (Figure 2.3), whereas the inhibition in proliferation was more pronounced after shRNA-mediated depletion of CD44 and RHAMM compared to that observed after treatment with 4MU (Figure 2.6) and incubation with antibodies (Figure 2.7).

Taken together, our data indicate HA and its receptors, CD44 and RHAMM, play significant roles in mediating myogenic and connective tissue cell migration and proliferation during development.

Figure 2.9. CD44 and RHAMM depletion significantly affect both migration and proliferation of GFP+ and GFP- cells. A) Detection of CD44 or RHAMM depletion at protein level. Immunoblot analysis revealed reduction of CD44 and RHAMM protein using multiple shRNAs and the two most effective sequences were used for subsequent analysis. Detection of β-tubulin served as a loading control. B, C) Depletion of CD44 and RHAMM resulted in a significant reduction in the total cell migration (B) and proliferation (C) over 24 hrs. One-way ANOVA indicated shRNA treatment significantly affected migration and proliferation ($p<0.0001$). Tukey's post hoc test was used to compare between samples for migration and proliferation assays (***$p<0.0001$; For migration: error bars = S.E; $n \geq 352$ GFP+ cells/condition and $n \geq 205$ GFP- cells/condition across the 3 biological replicates. For proliferation, error bars = S.D.; $n \geq 15164$ GFP+ cells/condition and $n \geq 9089$ GFP- cells/condition across the 3 biological replicates).

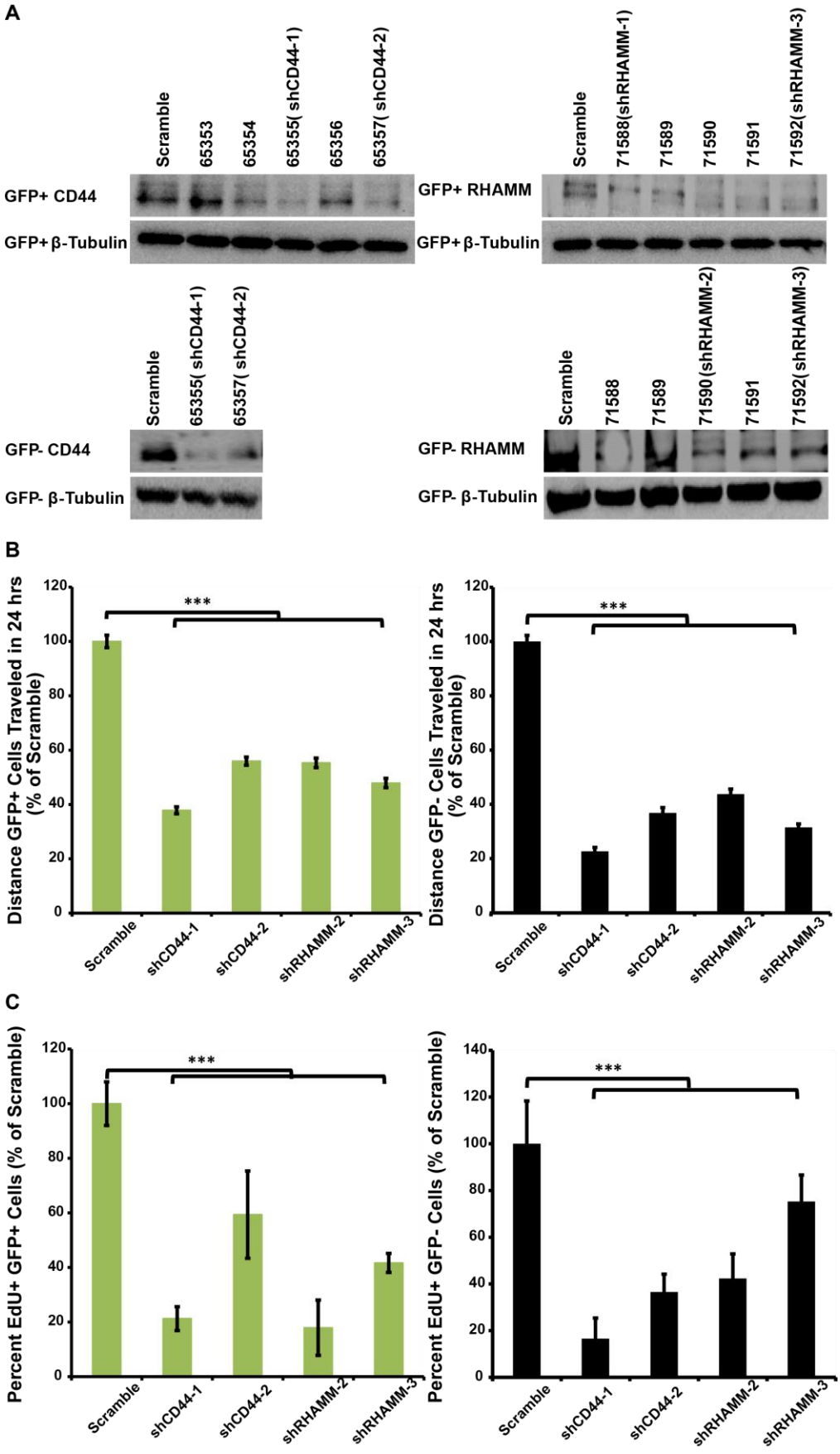
A
Scramble
65353
65354
65355(shCD44-1)
65356
65357(shCD44-2)
GFP+ CD44
GFP+ β-Tubulin
Scramble
71588(shRHAMM-1)
71589
71590
71591
71592(shRHAMM-3)
GFP+ RHAMM
GFP+ β-Tubulin
Scramble
65355(shCD44-1)
65357(shCD44-2)
GFP- CD44
GFP- β-Tubulin
Scramble
71588
71589
71590 (shRHAMM-2)
71591
71592(shRHAMM-3)
GFP- RHAMM
GFP- β-Tubulin
B
Distance GFP+ Cells Traveled in 24 hrs (% of Scramble)
***
Scramble
shCD44-1
shCD44-2
shRHAMM-2
shRHAMM-3
Distance GFP- Cells Traveled in 24 hrs (% of Scramble)
***
Scramble
shCD44-1
shCD44-2
shRHAMM-2
shRHAMM-3
C
Percent EdU+ GFP+ Cells (% of Scramble)
***
Scramble
shCD44-1
shCD44-2
shRHAMM-2
shRHAMM-3
Percent EdU+ GFP- Cells (% of Scramble)
***
Scramble
shCD44-1
shCD44-2
shRHAMM-2
shRHAMM-3

2.5 Discussion

The binding between HA and its receptors, CD44 and RHAMM, has been shown to control many types of cellular behavior (Acharya et al., 2008; Bourguignon et al., 2007; Hatano et al., 2011; Takahashi et al., 2005); however, the direct effect of these molecules on myoblast migration and proliferation during muscle development had not been previously investigated. Using a mouse model in which myoblasts are GFP+ and the remaining forelimb cells are GFP-, our study demonstrates that HA, CD44 and RHAMM play functional roles in embryonic myogenesis. Immunohistochemistry revealed that HA was widely expressed in the developing forelimb and myoblasts and the surrounding connective tissue cells expressed CD44 and RHAMM. Knockdown of HA *in vitro* using 4MU, and CD44 and RHAMM via shRNA, significantly inhibited the migration and proliferation of both cell types. In contrast, antibody blocking of CD44 and RHAMM induced differential effects on cell behavior, indicating that these receptors may be associated with different complexes depending on cell type. Collectively, our data show that cells within the limb utilize both CD44 and RHAMM to interact with HA during development.

This is the first study documenting both the expression dynamics and functional roles of CD44 and RHAMM in developing forelimb cells. Around E10.5, when muscle progenitors delaminate from the somite and migrate into the forelimb bud, RHAMM is highly expressed (Figure 2.1 and Figure 2.2). By E12.5, the expression of RHAMM is significantly downregulated (Figure 2.1 and Figure 2.2). At E12.5 myoblasts have begun to establish the basic pattern of the musculature and take on a more differentiated phenotype (Campbell et al., 2012). Our immunohistochemical and gene expression data, in combination with time-lapse imaging demonstrating that anti-RHAMM inhibits myoblast migration (Figure 2.4), supports this view and indicates that RHAMM is downregulated once the cells have reached the appropriate place within the limb to prevent further migration. A similar downregulation of RHAMM was correlated with osteoblastic cell differentiation (Hatano et al., 2012).

Our data indicate that HA promotes myoblast proliferation (Figure 2.6), which may be mediated by the ability of HA regulate cell shape during the G1, S, and G2 phases (Solis et al., 2012). In addition, this may be due to CD44 and RHAMM signaling as we found that anti-CD44, shCD44 and shRHAMM affected myoblast proliferation (Figure 2.7 and

Figure 2.9.C). Our results contrast with a previous study showing that myoblasts from CD44-knockout mice show no difference in proliferation compared with wild-type cells (Mylona et al., 2006). The disparity is likely due to differences in experimental protocols, as they labeled wild-type and CD44-knockout myoblasts with BrdU for only 1 hr (Mylona et al., 2006), whereas we incubated cells with EdU for 24 hrs. Additionally, the expression of other HA receptors likely increased in CD44-knockout cells to compensate. This type of compensation may also explain why lung fibroblasts from CD44-knockout mice also showed no difference in motility (Acharya et al., 2008), whereas our results showed that anti-CD44 significantly decreased the migration of GFP- cells (Figure 2.4). Surprisingly, cells treated with both anti-CD44 + anti-RHAMM did not show any difference in proliferation. We hypothesize that the addition of anti-RHAMM could affect the affinity of CD44 binding to the antibody, since CD44 and RHAMM are known to form complexes on the cell surface (Misra et al., 2015).

Based on our findings that both CD44 and RHAMM have significant impacts on embryonic myoblast behavior, whether mice deficient in CD44 or RHAMM have abnormal limb formation needs to be considered. During development, $CD44^{-/-}$ mice are viable with normal growth and appearance (Hilberg et al., 2018; Schmits et al., 1997; Sherman et al., 1998), which may be contributed to compensation by other molecules. However, an antibody-blocking experiment that interfered with CD44 variants CD44v3 and CD44v6 disrupted limb outgrowth in rat embryos cultured in vitro (Sherman et al., 1998). In that system, compensation for CD44 deficiency may no longer be possible when induced at later stages of development. RHAMM knockout mice are also viable without obvious deficiencies (Tolg et al., 2003), even though RHAMM has been described to be essential for a variety of several cellular events that are required for tissue formation such as cell migration, proliferation, and ECM remodeling (Tolg et al., 2014). Surprisingly, RHAMM-CD44 double-knockout mice did not develop any significant abnormalities, suggesting that there might be other HA receptors or molecules redundant with and compensate for RHAMM and CD44 (Tolg et al., 2006, 2017).

Our data are the first findings that describe changes in *HAS* and *Hyal* gene expression in skeletal muscle during forelimb development and indicate that myoblasts and the surrounding cells are capable of regulating the deposition of HA (Figure 2.2). *HAS2* mRNA was expressed at higher levels compared to other isoforms (Supplemental Figure A. 2), and increased by 2-fold from E10.5 to E12.5 in both cells (Figure 2.2). Multiple studies have shown that HAS2 plays a predominant role in inducible HA synthesis in muscle cells (Calve et al., 2012) and fibroblasts (Jacobson et al., 2000; Midgley et al., 2013; Wang et al., 2014). *HAS1* expression level was the lowest (Supplemental Figure A. 2)), and did not significantly vary over myogenesis. This corresponds to a previous study which showed *HAS1* is primarily found during gastrulation (E7.5–E8.5) (Tien & Spicer, 2005) and it maintains a basal level of HA synthesis during embryogenesis whereas HAS2 encourages cell migration and invasion (Adamia et al., 2005). Significantly more *HAS3* mRNA was expressed by GFP- cells compared to GFP+ cells (Figure 2.2 and Supplemental Figure A. 2)), which suggests a preferential synthesis of low molecular weight HA in GFP- since HAS3 produces HA chains less than 10^6 Da (Brinck & Heldin, 1999). The developing vasculature was likely the source of *HAS3* as our previous study showed HAS3 was localized to the vessels in adult muscle (Calve et al., 2012). Hyals are involved in tissue remodeling during development, of which Hyal1 and Hyal2 are the two most abundant and important (Fraser et al., 1997). Our results showed increased expression of Hyal1- Hyal 4 suggesting catabolism of high molecular weight HA is a feature of forelimb development. By breaking down HA, the interstitial barrier was hydrolyzed, tissue permeability was thereby increased (Ghatak et al., 2015). The overall increase of HAS2 and HAS3, concomitant with upregulated Hyal1- Hyal4, indicates rapid ECM remodeling tissue during myogenesis.

We used 4MU to investigate how knockdown of HA influenced the migration and proliferation of embryonic muscle precursors. Though commonly described as a specific inhibitor of HA synthesis by depleting the HA precursor UDP-GlcUA (Vigetti et al., 2009), 4MU has also been reported to affect the regulation of UDP-glucose dehydrogenase (UGDH), a key enzyme required for both HA and sulfated-glycosaminoglycan production (Clarkin et al., 2011). In addition, 4MU has been shown to downregulate the expression of CD44, RHAMM (Lokeshwar et al., 2010), and downstream effectors in the HA signaling cascade such as phospho-ErbB2, phospho-Akt, matrix metalloproteinases 2 and 9 (Twarock et al., 2011; Urakawa et al., 2012). However, our results viewed collectively indicate that the effect of 4MU on embryonic forelimb cell proliferation

and migration *in vitro* is linked to the knockdown of HA synthesis (Figure 2.3 and Figure 2.6). Through histology, we confirmed that 4MU substantially reduced HABP reactivity (Figure 2.3) and perturbation of cell – HA interactions via incubation with anti-CD44 and anti-RHAMM significantly affected cell migration and proliferation (Figure 2.4 and Figure 2.7).

After antibody treatment, we investigated how the expression of CD44, RHAMM and other HA-associated molecules changed. Immunohistochemistry revealed a higher level of RHAMM after treatment with anti-CD44 and anti-RHAMM compared with control (Figure 2.4). Quantitatively, *RHAMM* expression significantly increased in anti-RHAMM, and anti-RHAMM + anti-CD44 treated groups (Figure 2.5). Similar observations of RHAMM compensation have been documented in CD44-knockout mouse models (Jong et al., 2012; Nedvetzki et al., 2004). The overall increase in expression of both receptors in response to antibody treatment highlights the importance of RHAMM and CD44, and HA-specific signaling for cells.

Moreover, we showed that interfering with CD44 and RHAMM affects ERK signaling. CD44 and RHAMM are thought to play roles in controlling extracellular signal-regulated kinase (ERK), which has a significant role in HA-mediated cell motility and cellular proliferation (Tolg et al., 2006; Zhang et al., 1998). ERK1,2 acts downstream of cell surface CD44 and RHAMM in these pathways (Tolg et al., 2006, 2010). As expected, treatment of GFP+ cells with antibodies against CD44 and RHAMM led to attenuated activation of ERK1,2 in culture. Addition of both antibodies in combination exhibited a more inhibitory effect on ERK1,2 activation. These results together showed that HA-CD44 and HA-RHAMM interactions are crucial in regulating myoblast behavior during forelimb development.

ShRNA depletion confirmed that both CD44 and RHAMM are important mediators of HA signaling in myogenic and connective tissue cell migration and proliferation. Similar to cells treated with 4MU (Figure 2.3), migration was inhibited in CD44- and RHAMM-depleted cells compared to the controls (

Figure 2.9), whereas no significant effect was found in anti-CD44 treated GFP+ cells (Figure 2.4). The differential results between the antibody and shRNA depletion studies can mainly be explained by the limitation of the anti-CD44 we used. First, the antibody detects a standard 85kDa isoform of CD44 (Rudzki & Jothy, 1997); whereas there are many CD44 isoforms (Goodison et al., 1999; Misra et al., 2015). Second, anti-CD44 binds to the "link" domain on cell surface CD44. The "link" domain enables CD44 to bind to HA (Ponta et al., 2003); however, the affinity or the percentage of binding may not be that strong. Third, the blocking effect of the antibody against CD44 may act for less than 24 hrs (Huang et al., 2013). The variability of effectiveness using CD44 blocking antibodies between experiments has also been described (Tolg et al., 2017). These three reasons indicate the antibody may not fully interrupt the interaction between HA and CD44. In addition, HA is the principal, but by no means the only, ligand of CD44. Other ECM components can bind to CD44, including type I and type VI collagen (Faassen et al., 1992; Radotra et al., 1994), fibronectin (Jalkanen & Jalkanen, 1992), laminin (Hibino et al., 2005), and chondroitin sulfate (Hurt-Camejo et al., 1999). The antibody may not be able to interfere with the interaction between CD44 and these ligands. In contrast, shCD44 depletion impeded any CD44-binding ligands from influencing GFP+ cell migration.

For proliferation, the inhibitory effects of CD44 and RHAMM depletion were clear, *i.e.* there was about 80% reduction in the number of EdU+ cells (

Figure 2.9). Cells treated with 0.5mM and 1.0mM 4MU also showed a remarkable decrease in DNA synthesis, but to a lesser degree than those transfected with shCD44 and shRHAMM. Due to the limited solubility of 4MU in growth medium, we were unable to increase the concentration

of 4MU to have a similar effect. While CD44 antibody treatment decreased proliferation rate, it was less pronounced than in shCD44 and shRHAMM transfected cells. Again, since the blocking effectiveness using antibodies may not be complete, it is reasonable to have stronger inhibition results with shRNA-mediated depletion. The difference in proliferation between anti-RHAMM and shRHAMM may be attributed to the different function of cell surface RHAMM and intracellular RHAMM (Maxwell et al., 2008). Intracellular RHAMM, a mitotic spindle protein, has been shown to control mitotic spindle stability, and thus affecting cell proliferation. However, anti-RHAMM binding to surface RHAMM, may not affect the DNA synthesis of cells. Although a previous study reported that antibody blocking of cell surface RHAMM signaling resulted in anti-proliferative effect of fibrosarcoma cells through the G2/M DNA damage checkpoint (Mohapatra et al., 1996), the varied role of surface RHAMM may be attributed to differences in antibody, antibody efficiency, as well as other differences including cell type, HA origin and molecular weight. The different mechanisms behind how antibody and shRNA treatments affect cells may also explain other studies in which the differential effect of anti-RHAMM and anti-CD44 has been documented; RHAMM, but not CD44 was required for HA-mediated arterial smooth muscle cell (Gouëffic et al., 2006), endothelial cell (Savani et al., 2001), and B cell (Masellis-Smith et al., 1996) motility.

Our study established that CD44 and RHAMM activation promote myogenic and connective tissue migration and proliferation. These findings are in agreement with previous reports suggesting that CD44 and RHAMM have some overlapping functions in regulating cell behavior when interacting with HA (Hamilton et al., 2007; Nedvetzki et al., 2004). The discrepancies between our antibody blocking and shRNA depeletion studies indicate that many details regarding HA-receptor mediation of cell migration and proliferation remain to be characterized. For example, RHAMM is not an integral membrane protein and must cooperate with other receptors to compensate when CD44 activity is inhibited in order for HA-specific signals to be transmitted from the outside to the inside of the cell. However, the identities of these additional proteins have not yet been documented. Therefore, our future challenge is to further investigate how HA regulates cellular activities to gain a deeper understanding into how HA directs myogenesis.

3. EXTRACELLULAR MATRIX DEPOSITION PRECEDES MUSCLE-TENDON INTEGRATION

This chapter is a draft of a manuscript currently in preparation for publication.

3.1 Abstract

The development of a functional vertebrate musculoskeletal system requires the integration of contractile muscle to load-bearing tendon. Despite the different embryologic origins and initially independent determination of these two cells, muscle and tendon then seamlessly integrate as development progresses. A growing body of evidence demonstrates that ECM strongly affects muscle, tendon, and MTJ function. To investigate the spatiotemporal distribution of ECM composition and its role during the formation of muscle-tendon interface in early musculoskeletal assembly, we decellularized and cleared wild type, Pax3-Cre/Cre, and Pax3-Cre/ZsGreen1+ forelimbs, and stained for different ECM proteins. We observed that tendon ECM was correctly formed even when muscle was knocked out. At E11.5, a time point before the integration of muscle and tendon, an ECM-based template was deposited. These ECM fibers, including type I collagen, type V collagen, and fibrillin-2, also delineated the muscle deposition pattern. This new information regarding the instructive role of ECM in developing forelimbs offers the potential to establish guidelines for regenerative scaffolds aiming to restore these interfaces in diseased and damaged tissues.

3.2 Introduction

The extracellular matrix (ECM) is a three-dimensional (3D) network of cell-secreted molecules that provides cells, tissues, and organs with biochemical and structural supports. Cellular structure and function depend on dynamic interactions with ECM proteins (Yue, 2014). Tendon is an ECM-rich connective tissue that attaches muscle to the skeleton. Its ECM is mainly composed of collagens, laminins, and fibronectin (Kannus, 2000; Kjaer, 2004; Schweitzer et al., 2010). The collagen fibril proteins crosslink to each other to withstand the strong tensile forces of skeletal muscle (Banos et al., 2008; Thorpe et al., 2013). The transmission of these mechanical forces from muscle to bone is based on the interaction between muscle and the ECM components.

The primary site of force transmission is represented by the myotendinous junction (MTJ), a specialized ECM-rich structures located at the muscle-tendon interface (Charvet et al., 2012). Despite this important role, it is only over the last decade that the dynamic nature of the ECM of individual muscle and tendon tissue has begun to be appreciated. However, the roles of the ECM that integrates skeletal muscle and tendon at the MTJ during development are only partly understood.

The ECM of skeletal muscles is a complex meshwork organized in three layers: (i) the epimysium envelops the entire skeletal muscle, (ii) the perimysium bundles a variable number of muscle fibers, and (iii) the endomysium, representing the innermost level, outlines individual muscle fibers (Gillies & Lieber, 2011). The ECM contains various proteins, with collagens and proteoglycans being the most abundant (Purslow, 2002; Riso et al., 2016). At present, collagen, contains 28 different collagen types (Csapo et al., 2020; Ricard-Blum & Ruggiero, 2005). In skeletal muscle, types I, III, IV, V, VI, XI, XII, XIII, XIV, XV, XVIII, and XXII have been found at the gene expression and/or protein level, which provide muscular flexibility (Csapo et al., 2020; Jacobson et al., 2020). Besides the proteoglycans, several other proteins are found in the hydrophilic ECM, such as noncollagenous glycoproteins (Heinegård, 2009).

The ECM of tendon consists primarily of collagens, accounting for ~ 60–85% of the dry weight of the tissue (Kastelic et al., 1978). Among those, 95% of the collagen is type I, and the rest are types II, III, IV, V, VI, XI, XII, and XIV (Banos et al., 2008; Jacobson et al., 2020; Riley, 2004; Thorpe et al., 2013). Similar to muscle, tendon packed in a hierarchical fashion. The collagen-rich fiber-like structure (Birk et al., 1997) orients along the long axis of the tissue (the loading direction), giving the tendon high tensile strength (Screen et al., 2015). Collagen fibrils, the principal tensile element in tendon, are packed into fibers, fascicles, and finally the whole tendon (Asahara et al., 2017). Each level of the hierarchy also includes a small number of non-collagenous matrix components, such as laminins, fibrillins, and fibronectin (Kastelic et al., 1978; Thorpe et al., 2013; Yoon & Halper, 2005).

Muscle and tendon have different embryological origins (Baldino et al., 2016). The limb muscle originates from Pax3-expressing myogenic progenitors in the somite that migrate into the limbs, and give rise to muscle in following successive phases (Buckingham et al., 2003; Hutcheson et al., 2009). In mouse limb, the basic pattern of muscles is established during embryonic myogenesis, when embryonic myoblasts differentiate into primary muscle fibers (about embryonic

day (E)10.5-12.5 in the mouse limbs) (Biressi et al., 2007). During fetal myogenesis (E14.5-postnatal day (P)0), fetal myoblasts both fuse to primary fibers and fuse to one another to make secondary myofibers, and innervation begins to be established (Ontell & Kozeka, 1984). As for neonatal myogenesis (P0-P21), myofibers grow rapidly by increasing myonuclear number (White et al., 2010). Adult myogenesis is necessary for postnatal growth and repair of damaged muscle without changes in myonuclear number (Mathew et al., 2011). Limb tendon originates from the lateral plate mesoderm inducting from proximal to distal progressively (Chevallier et al., 1977). Scleraxis (Scx), the an early tendon marker, is first detected in limb buds at E10.5 and labels tendon progenitor cells, eventually giving rise to tendons. (Huang et al., 2015; R. Schweitzer et al., 2001). However, Scx mutant mice are viable and mobile, indicating Scx is not the only master regulatory gene of the tendon lineage (Murchison et al., 2007). The limb tendon pattern is evident around E12.5, when loosely arranged tendon progenitors align between differentiating muscle and cartilage (Murchison et al., 2007). Then, tendon progenitor cells condense at E13.5 and express differentiation markers, such as Tnmd (Shukunami et al., 2001, 2006), Mkx (Ito et al., 2010; Liu et al., 2010), Egr1, and Egr2 (Lejard et al., 2011). By E14.5, the basic tendon patterning is mostly completed (Huang et al., 2015; Huang, 2017; Watson et al., 2009).

The MTJ, a specialized zone between tendon and muscle, is enriched with the ECM components laminins, types I and IV collagen, and thrombospondins (Jacobson et al., 2020; Subramanian & Schilling, 2015). At the junction, muscle cells and tendons interact with the ECM via transmembrane proteins, including integrins and utrophin (Charvet et al., 2012). Structurally, the MTJ forms finger-like processes between the muscle sarcolemma and tendon ECM to increase the attachment surface area and are crucial in force transmission (Knudsen et al., 2015). The formation of the MTJ during embryogenesis is as follows: nondifferentiated tendon and muscle progenitors condense at the site of future MTJ development. In the late fetal and early neonatal stage, tenocytes and ECM proteins start to orient themselves to the direction of the contractile force in the developing muscle (Baldino et al., 2016; Kostrominova et al., 2009; Narayanan & Calve, 2020).

Although many studies have described the formation of muscles (Buckingham et al., 2003; Christ & Brand-Saberi, 2002; Helmbacher & Stricker, 2020), tendons (Subramanian & Schilling, 2015), and MTJ (Charvet et al., 2012; Valdivia et al., 2017) during vertebrate embryonic development, there is limited knowledge regarding the role and overall composition of the ECM

in muscle, tendon, and MTJ during morphogenesis. Here, we explored the role, composition, and spatial distribution of the ECM proteins in muscle and tendon integration during murine limb development between E10.5 – E14.5. Our research, for the first time, provided evidence that an ECM-based template guided the formation of these tissues and directed the proper assembly of the MTJ during early development. Overall, we expect our identification of the regulatory properties of this template will be instrumental for advancing the design of replacement constructs that aim to rebuild functional tissues (muscle, tendon, and MTJ).

3.3 Materials and Methods

3.3.1 Embryo harvest and tissue acquisition

All murine experiments were approved by the Purdue Animal Care and Use Committee (PACUC; protocol #1209000723). PACUC ensures that all animal programs, procedures, and facilities at Purdue University adhere to the policies, recommendations, guidelines, and regulations of the USDA and the United States Public Health Service following the Animal Welfare Act and Purdue's Animal Welfare Assurance. Pax3-Cre (Engleka et al., 2005) and ROSA-ZsGreen1 transgenic mice (Soriano, 1999)were obtained from the Jackson Laboratory (Bar Harbor, ME, USA) and used to generate Pax3-Cre/ZsGreen1+ embryos in which all Pax3-expressing cells and their progeny are GFP+ for observing muscle cells *in situ* clearly (

Figure 3.1. A). Within the forelimb, approximately 90% of GFP+ cells are of the skeletal muscle lineage, whereas the rest are endothelial cells (Hutcheson et al., 2009). Males heterozygous for the Pax3-Cre transgene were time-mated with females homozygous for ROSA-ZsGreen1 and noon on the day a copulation plug was found was designated as E0.5. Similarly, Pax3-Cre/Cre (Pax3 knockout) embryos were obtained by the timed mating of Pax3-Cre/+ mice or two Pax3-Cre/ZsGreen1+ mice. Specifically, Pax3-Cre/Cre embryos generated via two Pax3-Cre/ZsGreen1+ mice were used to easily visualize the region with absent limb muscle in whole-

mount sample or cryosectioning sample since the GFP+ endothelial cells still migrated into the limb. Pax3-Cre/Cre embryos were identified by their neural tube and neural crest defects (Engleka et al., 2005) (

Figure 3.1. B) and confirmed by genotyping. E10.5-E14.5 embryos were harvested from dams euthanized via CO2 inhalation followed by cervical dislocation. The embryos were transferred to 1x phosphate-buffered saline (PBS) on ice. Removal of the yolk sac and amnion was performed under a dissecting microscope (DFC450, Leica Microsystems) to avoid damaging the embryos. After dissection, forelimbs were immediately harvested and either fixed in 4% paraformaldehyde (PFA) (Fisher Scientific, J19943K2) at 4 °C overnight and then washed with PBS for the preparation of whole-mount or cryosectioned samples or processed for decellularization to enhance the visualization of the ECM.

3.3.2 Forelimb decellularization

After dissection, fresh forelimbs were mounted in 1% low gelling temperature agarose (Sigma-Aldrich, A9045) in a 10 mm x 10 mm x 5 mm biopsy cryomold (Tissue-Tek, 4565). The agarose cubes containing forelimbs were submerged in 1 mL 0.05% sodium dodecyl sulfate (SDS) (VWR, 0837) buffer and 2% Penicillin-Streptomycin (PS) in PBS, and gently rocked at room temperature (RT). The SDS-PS solution was replaced every 24-48 hours (h) until decellularization was complete, after 3-6 days (d) (

Figure 3.1. D, E). Upon decellularization, the agarose cubes were washed in 1x PBS buffer for 1 h, fixed with 4% PFA in PBS for 1 h, then washed with PBS for 1 h again with gentle rocking at RT. The decellularized forelimbs were extracted from the agarose by first trimming the surrounding agarose with a scalpel blade, then carefully removing the remaining agarose with forceps under a dissecting microscope, and stored in 1x PBS buffer at 4 °C for no more than 7 d until stained and imaged as described below (3.3.5). Tissue after decellularization was compared with fructose cleared sample to show that the maintenance of the ECM structure (Supplemental Figure B. 1.)

Figure 3.1. Experimental overview. (A) Pax3-Cre and/or ROSA-ZsGreen1 transgenic mice were used to generate Pax3-Cre/ZsGreen1+ and/or Pax3-Cre/Cre embryos. (B) Homozygous Pax3 (Pax3-Cre/Cre) embryos (E13.5 in B), carry loss-of-function Pax-3 alleles, develop neural tube defects, and die around E14.5 (Franz, 1989). Scale bar = 2 mm. (C) Immunohistochemistry of E13.5 limb muscles using My32 (myosin) antibody (red). The absence of muscles in Pax3-Cre/Cre forelimb was confirmed. (D) Harvested murine forelimbs were embedded in 1% low gelling agarose, and then decellularized in sodium dodecyl sulfate (SDS) with penicillin-streptomycin for 3-6 days. (E) Forelimbs were cleared following (Calve et al., 2015; Ke et al., 2013). Briefly, tissues were equilibrated to increasing concentrations of fructose (20%, 40%, 60%, 80%, 100%, and 115% wt/vol) by incubating in each formulation for at least 24 h under gentle rocking at RT. (F) Comparison of control and decellularized E13.5 forelimbs. Control and cleared samples were imaged using the same acquisition parameters on using a Leica M80 stereomicroscope. Scale bar = 2 mm. (G) Optically cleared E11.5 embryo. The transmittance of light was greater after clearing. Scale bar = 2 mm.

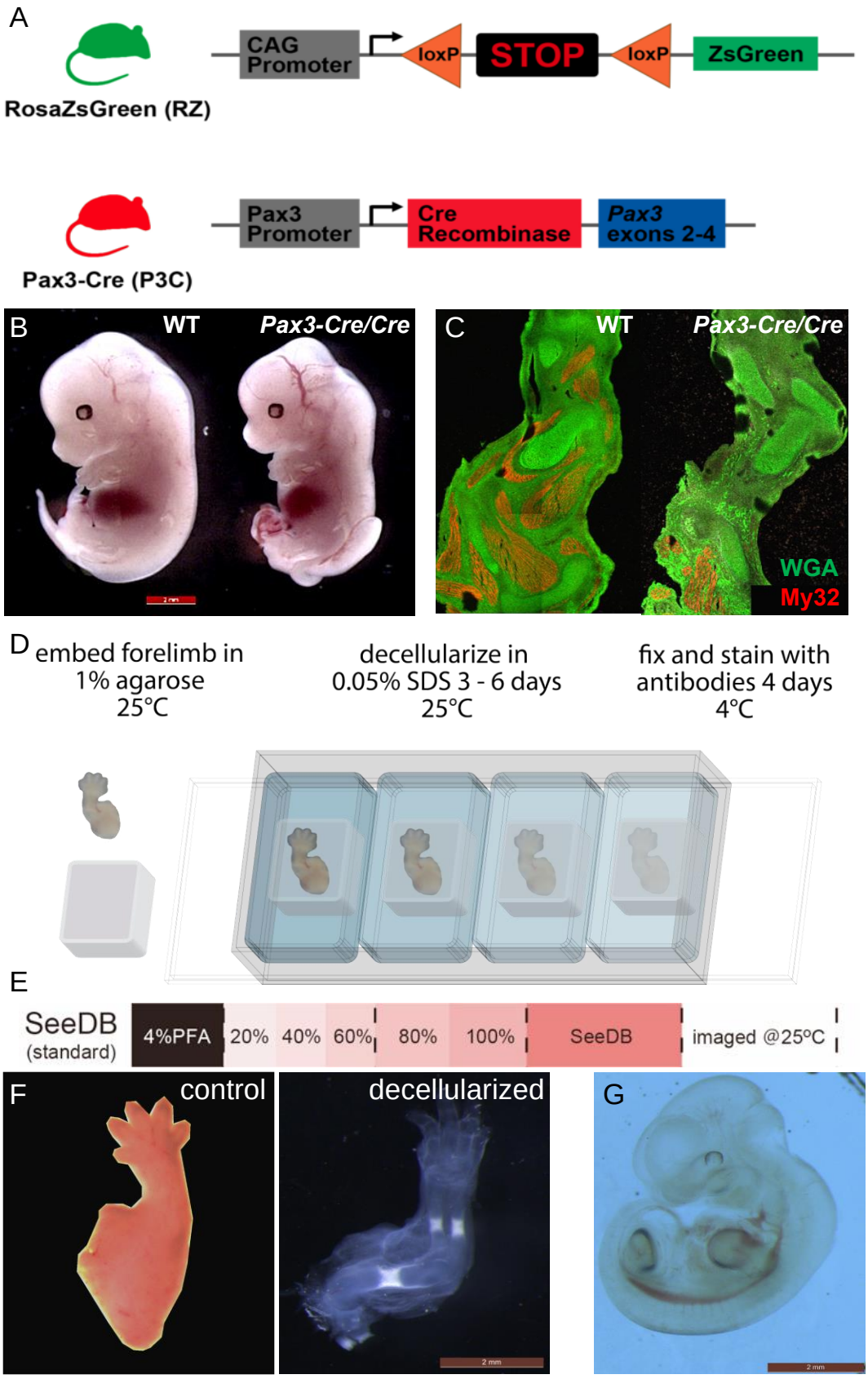
A
RosaZsGreen (RZ)
CAG Promoter
loxP
STOP
loxP
ZsGreen
Pax3-Cre (P3C)
Pax3 Promoter
Cre Recombinase
Pax3 exons 2-4
B
WT
Pax3-Cre/Cre
C
WT
Pax3-Cre/Cre
WGA
My32
D
embed forelimb in 1% agarose 25°C
decellularize in 0.05% SDS 3 - 6 days 25°C
fix and stain with antibodies 4 days 4°C
E
SeeDB (standard)
4%PFA
20%
40%
60%
80%
100%
SeeDB
imaged @25°C
F
control
decellularized
G

3.3.3 Cryosectioning and immunohistochemistry

Forelimbs from Pax3-Cre/Cre and wild type (WT) embryos were fixed in 4% PFA for 1 h, washed with PBS 3 × 30 minutes (min) before embedding in Optimal Cutting Temperature compound (OCT, Sakura Finetek), frozen with dry ice-cooled isopentane (Fisher Scientific), and stored at -80 °C. 10 µm-thick cryosections were collected on His-bond glass slides (VWR) and processed following (Leng et al., 2019). Sections were incubated with primary antibody against My32 (1:200, Invitrogen, MA5-11748) at 4 °C overnight, and washed with PBS for 3 × 5 min. Then, the slides were stained with the DAPI (1:500, Roche), Alexa Fluor 488 wheat germ agglutinin (WGA, to label proteoglycans, 1:250, ThermoFisher, W11261), and secondary detection reagent Alexa Fluor 546 Goat anti-Mouse IgG1 (1:500, Invitrogen). Sections were imaged at 10× water (W) using a Zeiss LSM 880 confocal.

3.3.4 Vibratome Sectioning

Fixed forelimbs were embedded in 3.5% low melting point agarose (Amresco) in 1x PBS and set at RT for 30 min to solidify. Agarose-embedded samples were then positioned in the appropriate plane and attached to the sample holder of a Leica VT-1000S vibratome with Loctite super glue and the chamber was filled with PBS to maintain sample hydration. Forelimbs were sliced into 250 µm thick sections and were stored in a tissue culture dish filled with PBS on ice. Extra agarose was dissected away from the tissue by forceps. Samples were stained for ECM molecules the same day following 3.3.5.

3.3.5 Fluorescent labeling of ECM and imaging

After PFA fixation, decellularized forelimbs or vibratomed sections were incubated in blocking buffer [10% donkey serum diluted in 1x PBS with 1% Triton X-100 (PBST) and 0.02% sodium azide] for 16 h at 4°C to increase the ability of antibody stains to permeate through the sample and to block non-specific binding. Samples were then incubated with primary antibodies (concentrations defined in Table 3.1.) diluted in blocking buffer, and gently rocked at 4 °C for 48 h. Samples were rinsed 3 x 30 min with 1% PBST at 25 °C, and then incubated with secondary staining reagents diluted in blocking buffer, placed in a lightproof container, and rocked again at 4 °C for 48 h. Finally, after rinsing 3 x 30 min with 1% PBST at 25 °C, samples were stored in 1x

PBS at 4 °C until imaged. Samples were imaged using one of the following confocal microscopes: an inverted Zeiss LSM 880 confocal using either the 10x EC-Plan NeoFluar (NA = 0.3, working distance = 5.2 mm), or 25x multi-immersion LD LCI PlanApochromat (NA = 0.8, working distance = 0.57 mm) or an upright Zeiss LSM 800 confocal using 20x W immersion Plan-Apochromat (NA = 1.0, working distance = 2.4 mm). Upon imaging, the biceps and triceps were the main areas of interest. Z-stack and tile function were used to capture the entirety of the muscles. Widefield images were acquired using a Leica M80 stereo microscope.

Table 3.1. Antibodies and stains used for fluorescent labeling of embryonic ECM.

Antibody or stain	**Host**	**Dilution**	**Source**	**Product #**
fibrillin-2	rabbit	1:100	Dr. Robert Mecham	
fibronectin	mouse IgG1	1:50	Sigma	F7387
type I collagen	goat	1:25	Santa Cruz	SC-8784
type IV collagen	rabbit	1:100	Novus Biologicals	NB120-6586SS
type V collagen	goat	1:100	Southern Biotech	1350-01
tenascin-C	rat	1:25	R&D	MAB2138
laminin alpha 1	rabbit	1:100	Novus Biologicals	NB300-144
rat DyLight 550	donkey	1:250	Invitrogen	SA5-10027
goat AF555	donkey	1:500	Invitrogen	A32816
mouse IgG1 AF546	goat	1:500	Invitrogen	A21123
rabbit AF647	donkey	1:500	Invitrogen	A31573
WGA AF488		1:100	Invitrogen	W11261

3.3.6 Forelimb optical clearing

To visualize the 3D morphology and spatial patterning of muscle cells embedded deep within the developing limb, and confirm that ECM structure was maintained after decellularization, fructose-based clearing solutions were utilized (

Figure 3.1.E). Forelimbs were cleared following (Calve et al., 2015). Fructose solutions of varying concentrations (20%, 40%, 60%, 80%, 100%, and 115% wt/vol) were generated by dissolving D-(-)-fructose (JT Baker, Center Valley, PA) in Milli-Q water with 0.5% α-thioglycerol (Sigma-Aldrich St. Louis, MO) to prevent browning. Fixed and stained tissues were equilibrated to increasing concentrations of fructose by incubating in each formulation for 8-24 h following (Calve et al., 2015; Ke et al., 2013) under gentle rocking at RT.

3.3.7 Image processing

In FIJI (NIH), confocal stacks were rendered in 3D; channels were separated; brightness and contrast were adjusted. For vibratome sections, image stacks were processed into maximum z-projections using FIJI. To remove some of the optical distortion inherent to confocal microscopy, the Nearest Neighbor Deconvolution function within the ZenBlue software package (Carl Zeiss Microscopy) was applied. Figures were assembled by taking snapshots of 3D-rendered image volumes or selecting 2D slices from stacks and were arranged using Adobe Photoshop and Illustrator.

3.4 Results and Discussion

3.4.1 Tendons are correctly formed without muscle

Due to the close association between muscles and tendons during limb development, we wanted to investigate the involvement of muscle in tendon patterning formation and map the ECM organization during forelimb muscle development by taking advantage of the existence of the Pax3-Cre mouse model. Although the role of transcription factors and signaling molecules in instructing myogenesis has been well studied (Bentzinger et al., 2012; Griffin et al., 2010; Kuang et al., 2008), the following questions remain: what is the role of ECM in guiding the myofibers to their sites of attachment? How do the myofibers form their final muscle shape? To find some answers to these question, we compared the forelimb from Pax3-Cre/Cre mouse embryo with the forelimb from WT mouse embryo. Pax3 is a transcription factor expressed in the dorsal neural tube and somite of the developing embryo (Stuart et al., 1994). Pax3 knockout embryos display

neural tube defects, specifically, exencephaly and/or spina bifida (Epstein et al., 1993), heart outflow tract defects (Morgan et al., 2008), lack limb musculature (Mansouri et al., 2001), and die midgestation (Epstein et al., 1993). In our experiments, Pax3 knockout embryos were generated by crossing Pax3 heterozygous mice. In the Pax3-Cre mouse, the first coding exon of Pax3 gene is replaced with a gene encoding Cre recombinase. This functions as a null allele and no Pax3 protein is expressed in Pax3-Cre/Cre embryos (Engleka et al., 2005). In this mouse embryo, the lack of Pax3 inhibits the muscle progenitor migration from trunk to forelimb. Whereas heterozygous offspring is healthy and characterized by white spots in the belly, back, tail, and feet due to localized deficiencies in pigment-forming melanocytes resulting from defects in neural crest cells (Boudjadi et al., 2018; Wu et al., 2008).

The presence of tendon in Pax3-Cre/Cre mice has already been reported (Bonnin et al., 2005; Edom-Vovard et al., 2002; Schweitzer et al., 2010), but without identification of the spatial organization, or the surrounding 3D ECM structure. We focused on two large muscles (i.e. biceps and/or triceps) in the forelimb as representative regions for the whole study. Previous confocal-based investigations of the 3D distribution of ECM in the developing musculoskeletal system have been limited to depths of less than 100 μm due to light scattering from cells and lipids (Orlich & Kiefer, 2018; Richardson & Lichtman, 2015). To enhance the resolution of ECM networks, we modified a previous decellularization method (Acuna et al., 2018) that maintains the matrix geometry of developing embryos. Using method 3.3.2 to make the forelimb transparent, the 3D structure of ECM could be visualized. Based on Z-stack imaging of decellularized forelimbs, the successive separations of these muscle masses can be visualized. The biceps lies on the front of the upper arm between the shoulder and the elbow. Both heads of the muscle arise on the scapula and join to form a single muscle belly which is attached to the upper forearm (Bogart & Ort, 2007). The triceps, a three-headed (lateral, medial, and long head) muscle, is located on the dorsal side of the humerus. As the largest muscle in the upper arms, it connects the humerus and scapula to the ulna (Barco et al., 2017; Platzer & Kahle, 2003). We analyzed the tendon pattern in Pax3-Cre/Cre samples (corresponding to biceps and triceps regions) using WGA. WGA binds to proteoglycans containing sialic acid and N-acetylglucosamine and provides a global label for musculoskeletal tissue ECM (Kostrominova, 2011). Both WT and Pax3-Cre/Cre forelimbs were visualized between E12.5-E14.5. In E13.5 WT control limbs, the tendon at the distal side of biceps is attached to the radial tuberosity, and the tendons for the short head and long head of the biceps are inserted at the

coracoid process and supraglenoid tubercle of the scapula (Figure 3.2. A). The three heads of the triceps merged to form a single tendon which had an insertion attachment point on the posterior aspect of the olecranon (the bony prominence of the elbow) on the upper ulna. The proximal attachments of the triceps inserted into the infraglenoid tubercle on scapula, the lateral humerus shaft, and the posterior/medial humerus shaft for the long, lateral, and medial heads, respectively (Figure 3.2. C). In Pax3-Cre/Cre limbs, the tendons organized in a similar pattern (Figure 3.2. B, D). This stereotyped organization of tendon is consistently observed in the forelimbs of mouse embryos starting at E12.5.

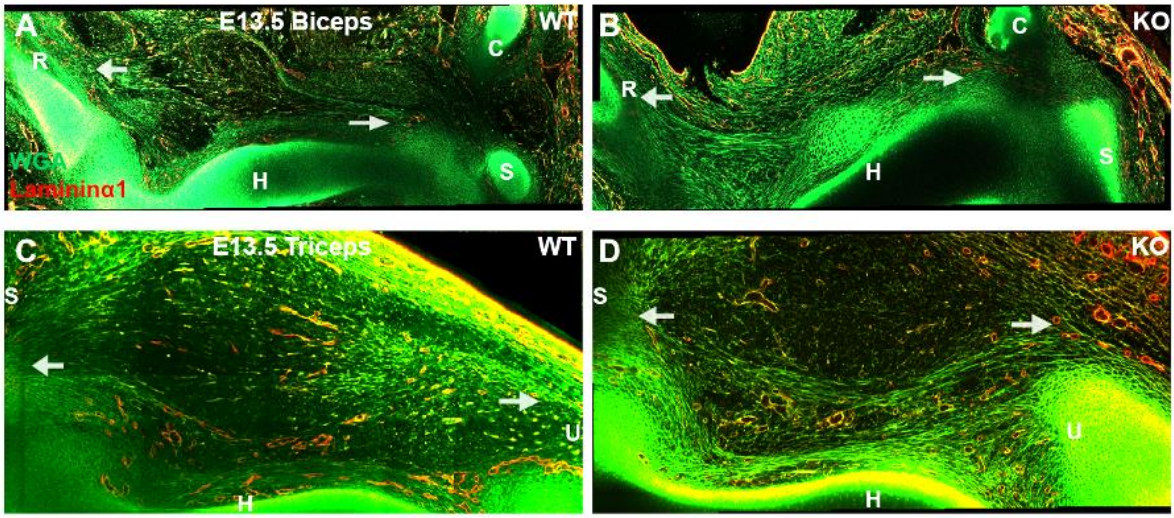

Figure 3.2. Biceps and triceps tendons were developed correctly in the absence of muscles. (A, B) Biceps region in WT and Pax3-Cre/Cre forelimbs. (C, D) Triceps region in WT and Pax3-Cre/Cre forelimbs. Arrows indicate the tendon at the ends of the corresponding muscle. (WGA: green; Laminin α1: red; C: clavicle; H: humerus; R: radius; S: scapula; U: ulna. Tiled 20x)

Taking a closer look at long triceps in E12.5-E14.5, we found that in both WT and Pax3-Cre/Cre forelimbs, ECM fibers were localized to the region where the long triceps attached to ulna or scapula. Individual fibers appeared to have a similar thickness in both WT mouse forelimbs and Pax3-Cre/Cre mouse forelimbs. In an E12.5 WT forelimb, tendon progenitors are organized as cellular aggregations between skeletal tissues and muscle (Schweitzer et al., 2010). After decellularization, initial fiber bundles were seen at this stage (Figure 3.3. A'). Recent studies implicated the induction of tendon is associated with fibroblast growth factors (FGFs) (Brent et al., 2003, 2005; Brent & Tabin, 2004; Edom-Vovard et al., 2002) and transforming growth factor β (TGFβ) (Pryce et al., 2009). Compared to WT, the number of tendon ECM fibers in Pax3-

Cre/Cre forelimbs was less than the number of tendon ECM fibers in WT forelimb. Pax3-Cre/Cre tendon was more loosely arranged with some discontinuity of the fiber (Figure 3.3. B', B''). By E13.5, fibers bundles were located at where the progenitor cells condensed and further organize into structurally aligned tendon fibers connecting the muscle and cartilage (Figure 3.3. C', C''). At E14.5, the fiber further elongated with increased density and differentiated into overtly distinct tendon bundles (Figure 3.3. arrows in E', E''). Generally speaking, previous studies have shown that the early events in tendon determination are independent of muscle cells. Experiments with muscle-less limbs have shown that the early expression of Scx (until E12.5) is normal (Blitz et al., 2009; Huang et al., 2015; Schweitzer et al., 2001). However, the differentiation of tendon progenitor cells into a fully mature tendon requires subsequent interaction with muscles (Kardon, 1998). The less robust ECM bundles observed in Pax3-Cre/Cre samples could because of the degradation of tendons in these Pax3 knockout forelimbs. As researchers have shown, limb tendons degenerate in embryos carrying null mutations in Myod1 (Brent et al., 2005) and Pax3 (Bonnin et al., 2005) that lack the entire limb musculature. The degradation could because of lacking mechanical forces transmitted via the ECM and the connection of the muscle fibers to the tendon (Subramanian et al., 2018; Subramanian & Schilling, 2015).

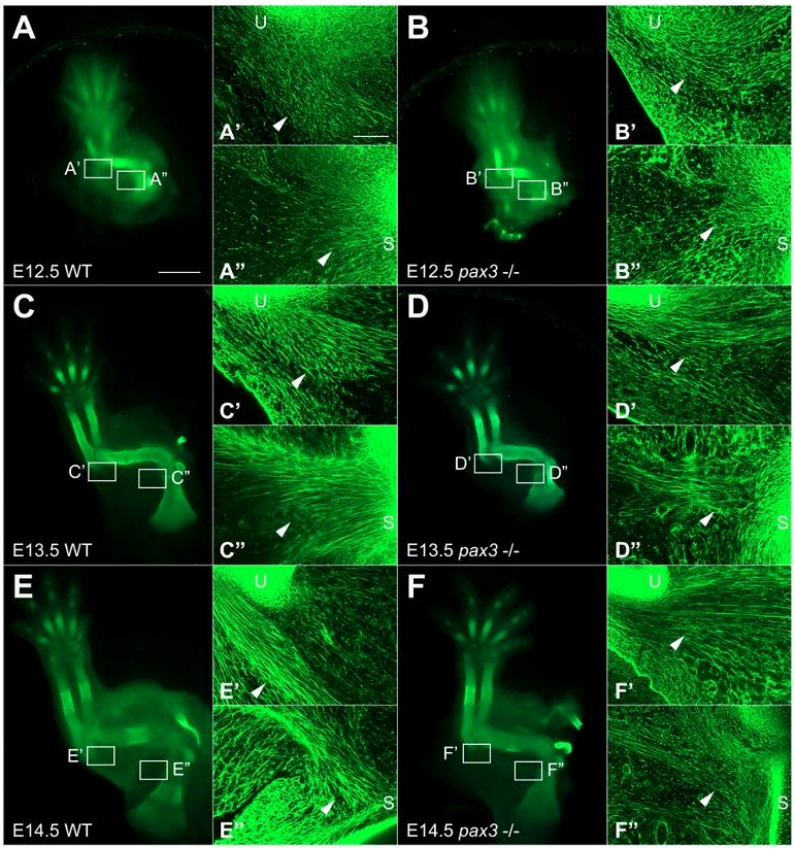

Figure 3.3. Long triceps tendon was developed correctly in the absence of muscles in E12.5-E14.5. (A-F) Decellularized forelimbs from E12.5-E14.5 WT (A, C, E) or Pax3-Cre/Cre (B, D, F) embryos were stained with WGA. (A'-F') The insertion of the long triceps into the ulna was rich in ECM in both WT and Pax3-Cre/Cre mouse forelimbs. (A"-F") Similarly, the origin of the long triceps at scapula existed both in WT and in Pax3-Cre/Cre forelimbs. Even though the tendon fibers were located at the correct position without muscle cells, the fiber bundles looked less dense in Pax3-Cre/Cre forelimbs comparing to WT forelimbs. Arrowheads indicate the region of the developing tendon. U = ulna, S = scapula. Panel A scale bar = 1 mm (B-F have the same magnification as A); Panel A' scale bar = 100 μm (B'-F' and B" – F" have the same magnification as A'). A' and A'' are a single Z-plane image taken at the same magnification (20x).

3.4.2 ECM exists before muscle-tendon integration

The correct morphogenesis and positioning of muscle, tendon, and their integrated unit are crucial to building a functional musculoskeletal system. However, there is still limited knowledge about how the muscle-tendon interface is formed and how these cells of different embryological origins find each other in the developing limb. As tendon formed appropriately in muscle-less limb (Schweitzer et al., 2010) and muscle cells aggregated in the correct spot even when tendon is disrupted (Pryce et al., 2009), these results imply that the muscle-tendon crosstalk might be directed by factors other than muscle and tendon progenitor cells, such as other cell sources and/or the ECM. To investigate when and what are the roles of ECM fibers associated with the initial establishment of connecting muscle and tendon progenitors at the interface, E11.5 WT mouse forelimb were analyzed, a time point before tendon progenitors organized between the muscle masses of the proximal limb (Hasson, 2011). Here, we focus again on the triceps region. At E11.5, the scapula and long triceps have not formed (Capellini et al., 2010). We found ECM fibers already attached to the ulna where the presumptive long triceps should be forming (Figure 3.4. B). Specifically, type I collagen (ColI), the predominant ECM component in tendon (Subramanian & Schilling, 2015), was assembled in a linear fibrillar structure (Figure 3.4. B'). Z-projection of 48 μm image stack showed WGA+ fibers from different z-plane were organized into highly ordered bundles at the position of future tendon (Figure 3.4. B'''). The scapula appears at E12, when we could find the ECM fibers which link triceps to scapula (E12 decellularized forelimb image data). These ECM proteins deposited in between muscle and tendon cells are said to interact with the two cells through integrin and provide mechanical integrity to the MTJ (Brown, 2000).

In Pax3-Cre/ZsGreen1+ mice, Pax3 expressing cells are GFP+. Although Pax3 expression in the limb bud is largely restricted to myogenic progenitors, a small subset of Pax3+ endothelial cells contribute to the limb vasculature and are predominantly found in the vessels below the epidermis (Hutcheson et al., 2009). In fructose cleared E11.5 WT forelimb, most of the Pax3 positive cells were loosely aggregated with no obvious organization in a central domain. The orientation of these early muscle precursors was not completely random. At the edge of the center cluster to the distal side, we detected the first evidence of these muscle progenitors being orientated along the proximal-distal axis of the limb. Significantly, these cells seemed to adhere to and elongate along the ECM fibers. These fibers, extended more toward the distal side comparing to the migrating cells, seemed to provide a trail to guide the cell migration and deposition along a "predetermined" path (as arrows in Figure 3.4. C, D). Similar to a recent study (Besse et al., 2020), our data indicated that muscle cells have some degree of alignment before the formation of muscle fibers. This alignment along a particular orientation vector was highly consistent with the orientation of ECM fibers, particularly fibrillin-2 (Fbn2). Given the remarkable similarity between elongating muscle cells and migrating cells, a hypothesis that the adhesion of cell to the ECM is necessary for cell elongation. Observations in both mouse and zebrafish clearly demonstrated that adhesion to laminin is necessary for muscle progenitor elongation (Bajanca et al., 2006; Snow et al., 2008). Moreover, fibronectin (Fn) is highly enriched during the myoblast elongation and is required for embryonic muscle attachments (Koshida et al., 2005). As Fbn2 fibers are highly aligned in the direction of force loading (Acuna, 2020), combining with the data (Figure 3.4. D), it is reasonable to hypothesize that Fbn2 also guides the orientated elongation of myocytes. Besides Fbn2, abundant tenascin-C and type V collagen (ColV) were observed around the muscle cells, demonstrating that the ECM fibers were broadly distributed even in the early developing limb, and also suggesting an instructive role of ECM prior to muscle-tendon integration. In conclusion, these results demonstrate the intimate association between ECM template specification and the early muscle alignment process.

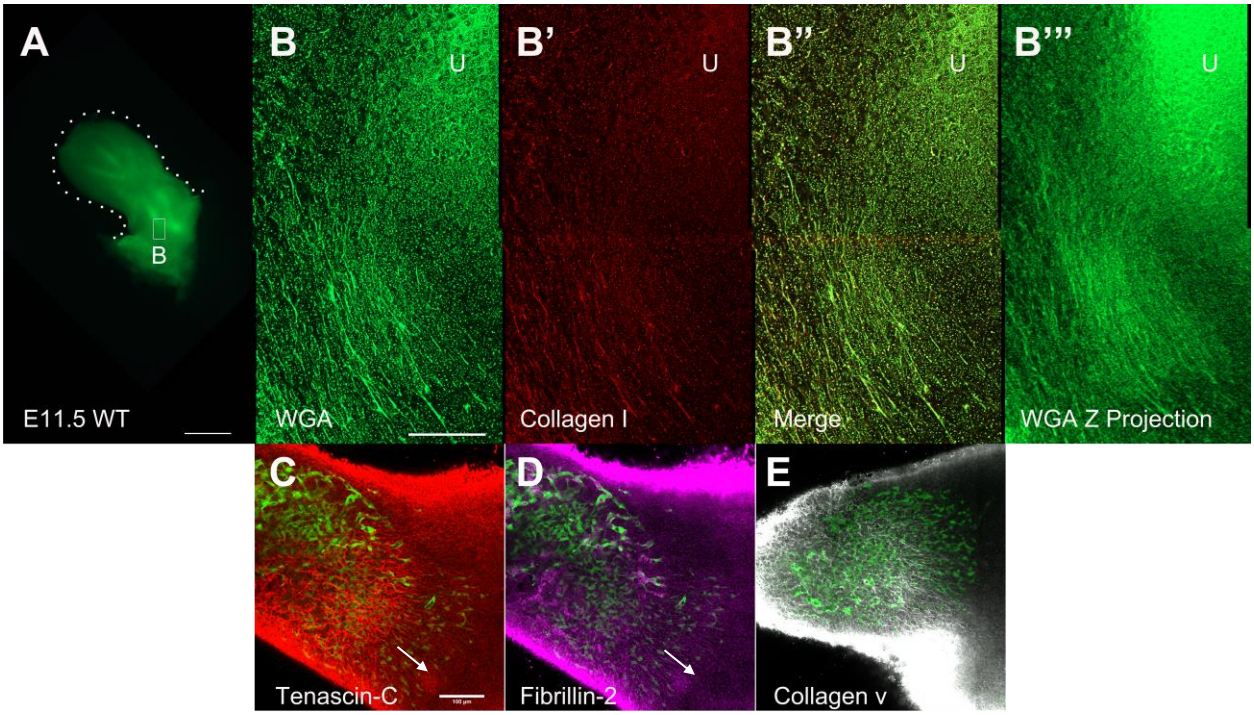

Figure 3.4. The alignment of GFP+ muscle cells and ECM fibers at E11.5 (a time point prior to the formation of a functional muscle-tendon unit) were visualized *in situ* after decellularization and fructose clearing. (A) Decellularized forelimb from WT embryos at E11.5, was stained with WGA. (B-B") Immunostaining for collagen I (red) showed the colocalization with WGA (green) (B'") Z projection of B images, (XY plane, 40 slices). Panel A scale bar = 1mm; Panel B scale bar = 100 µm. (C-E) Fructose cleared forelimb showed a relative distribution of Pax3 positive cells with respect to different ECM fibers. Arrows in C and D indicated the orientation of the ECM fibers and how muscle cells aligned. Red = tenascin-C; Magenta = fibrillin-2; Grey = type V collagen. U = ulna. Single z plane image from fructose cleared forelimb with the magnification = 25x (oil). Panel C scale bar = 100 µm. The left side of the image is proximal, and the right is distal.

3.4.3 ECM fibers delineate muscle deposition pattern

When muscle cell attaches to the tendon cells with the help of ECM fibers at E12.5 as suggested in Figure 3.4, they integrate with each other to form distinct muscle masses. What directs these myofibers to form a specific muscle shape? After decellularization, a highly organized ECM network in the muscle regions, visualized by WGA, was clearly detected. In the WT control forelimb, the extending fibers continued with the tendon-formed-networks and had the appearance of a fibril scaffold. An abundance of ECM fibrils from ulna to scapula surrounding the long triceps muscle belly, which forms parallel network contouring the shape of the muscle was also observed. Inside the muscle belly, the ECM fibril bundles serve as a template for the polarized deposition of

the fusiform myofibers; thereby generating a parallel aligned architecture of the muscle tissue, where direction dependence is essential for function. Light and electron microscopy results have revealed that the ECM spaces are increased in the muscle splitting sites. Cells are progressively dissociated within the myotube cluster, myoblasts are phagocytized, whereas mesenchymal stellate cells take their place (Schroeter & Tosney, 1991b). Astonishingly and significantly, in the decellularized muscle-less Pax3-Cre/Cre mouse forelimb, there was still complete compartmentalization of the corresponding muscle space by the ECM (dotted line area in Figure 3.5. B, D) at the exact site with the same shape as in the WT. This cavity zone had become obvious at E12.5. As embryogenesis progressed, the fibril number increased, and the margin of the muscle became sharply defined. Notably, the WGA+ fibril bundles, though not as robust as in WT, were still present in these mutants even without myofibers. These bundles outlined the supposed deposition sites of muscle mass along the whole length of the cavity. These data indicated that these fibrillar networks delineated the developing sites of muscle before muscle differentiation and organized themselves in early embryogenesis independently of muscle. A reasonable source of these ECM fibers is connective tissue cells. During the process of muscle splitting, connective tissue builds up in the freshly cleaved site (Schroeter & Tosney, 1991a). Many studies have demonstrated that muscle connective tissue participates in muscle patterning (Chevallier et al., 1977; Chevallier & Kieny, 1982; Kardon, 1998). Ectopically split limb muscle and abnormal tendon patterning were observed when normal muscle connective tissue was disrupted in Tbx5 deletion forelimbs (or in Tbx4 deletion hindlimbs) (Hasson et al., 2010). Conditional knockout of Tbx3 in connective tissue cells (Prx1-Cre) (Colasanto et al., 2016), or knockout of Osr1(which is expressed in connective tissue cells) (Vallecillo-García et al., 2017), leading to changes in the forelimb muscle shape. In chick limb, misexpression of Tcf4, a marker of muscle connective tissue cells that colocalized with ColI, causes defects in muscle patterning (Kardon et al., 2003). These results imply the involvement of the connective tissue in the muscle patterning and splitting process. The regulation of generating cleavage in muscles could be attributed to several mechanisms (Hasson, 2011). Combined with our image data, we hypothesized that connective tissue cells regulate muscle development partially through their ECM fibers in the forelimb.

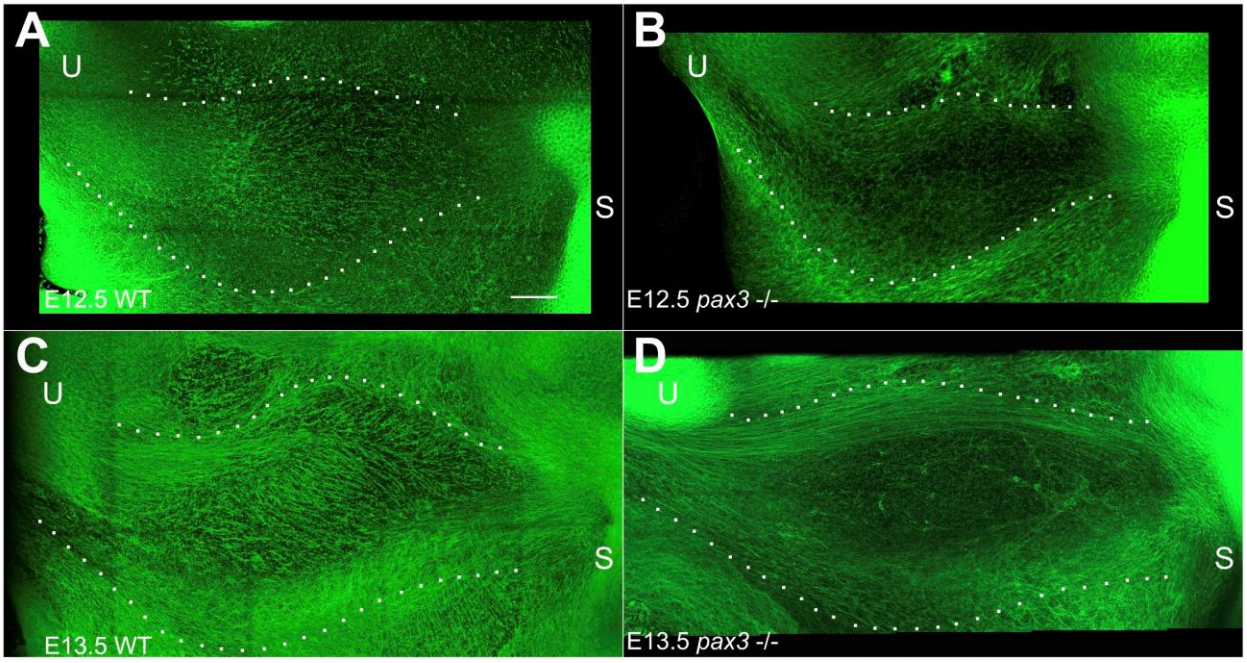

Figure 3.5. The compartmentalization of the skeletal muscle spaces by ECM fibrils. (A-D) Decellularized forelimbs from E12.5-E13.5 WT or Pax3-Cre/Cre mouse embryos were stained with WGA and visualized in 3D. In WT forelimbs (A, C), ECM fibers from ulna to scapula define the shape of the long triceps muscle (dotted outline). In Pax3-Cre/Cre forelimbs (B, D), although no muscle exists, the ECM delineates a space for the long triceps. U = ulna, S = scapula. Z projection from 230 µm thick image stack. Scale bar = 100 µm.

3.4.4 ECM fibers are rich in type I collagen, type V collagen, and fibrillin-2

Understanding which ECM proteins mediate the muscle cell elongation and muscle-tendon interface is required to obtain a complete understanding of mechanisms guiding muscle fiber morphogenesis. To investigate the participation of different ECM molecules in the ECM-based foundation for muscle, tendon, and MTJ development, decellularized WT or Pax3-Cre/Cre mouse embryos were stained with WGA and antibodies against ColI, ColV, Fbn2, and laminin alpha-1 (Lama1). These ECM proteins were shown to be broadly distributed in both WT and muscle-less forelimbs (Figure 3.6.). In general, ColI, ColV, and Fbn2 formed fibrillar bundles in the muscle and tendon region, whereas Lama1 mainly labeled the basement membrane of blood vessels, (Hallmann et al., 2005). In WT samples, these fibrillar proteins form a highly ordered network surrounding individual muscle fibers. ColI was concentrated in tendon region and highly aligned with muscle fibers crossing through the whole belly areas. These fibers became aligned along a

common proximal boundary but clustered into bundles with their own distinct orientation vectors. In the mutant limb, ColI was more on the edge of the region due to the absence of myofibers. ColV fibrils formed both linear and branched meshwork in the control limb. However, a sparser distribution was seen in Pax3 knockout embryos. There are three hypotheses that could potentially explain the lower amount of ECM fibers in the cave region: (1) the ECM fibers that were deposited by connective tissue cells in the cave region were weak and fragile without myofibers and thus were broken and washed out by SDS during decellularization or too thin to visualize clearly; (2) similar to the framework of the folded paper lanterns, the ECM fibers secreted by fibroblasts were squeezed to the edge of the cave without the filling of muscle cells; (3) the ECM fibers in the cave region were mainly secreted by muscle cells. In both muscle and tendon, ColI is the major tensile load bearing fibrillar collagen, and ColV is also fibril forming and can be found in smaller amounts than ColI and type III collagen (ColIII) (Trotter, 2002). ColV is known to be important to the assembly of ColI–containing fibrils (Wenstrup et al., 2004) and may have a role in controlling the collagen fiber diameter (Birk, 2001; Birk et al., 1990). It is said that ColV forms the core of the fiber whereas ColI and ColIII polymerize around the core (Gelse et al., 2003; Purslow, 2002). With Col5a1 knockout in the tendon, abnormal fiber organization was found in tendon and ligament in mice (Sun et al., 2015). While collagens have been widely studied, the other ECM proteins, especially fibrillins, in muscle, tendons, and MTJ have been poorly investigated. Here, our data showed that Fbn2, a glycoprotein highly expressed during embryogenesis, was organized into highly ordered and denser fibril bundles comparing to ColI and ColV, and concentrated mostly in tendon and the middle area of the muscle belly or “muscle” region. Similar to other data (Ritty et al., 2002, 2003), Fbn2 was abundant inside the tendon. These microfibrils derived from tenocytes run along with the tendon cell arrays. In Fbn2 knockout mice, collagens, even with the same total content as in WT, exhibited decreased crosslinking in the digital flexor tendons (Boregowda et al., 2008). In this study, certain colocalization of Fbn2 and WGA+ fibers were observed in both WT and Pax3 knockout forelimbs, which is in agreement with a previous study that reported specific segments of the fibrillins interact *in vitro* with numerous extracellular signaling and cell surface molecules (Olivieri et al., 2010). In conclusion, these proteins, co-stained with WGA+ fibrils, participated in defining and contouring the skeletal muscle region during development.

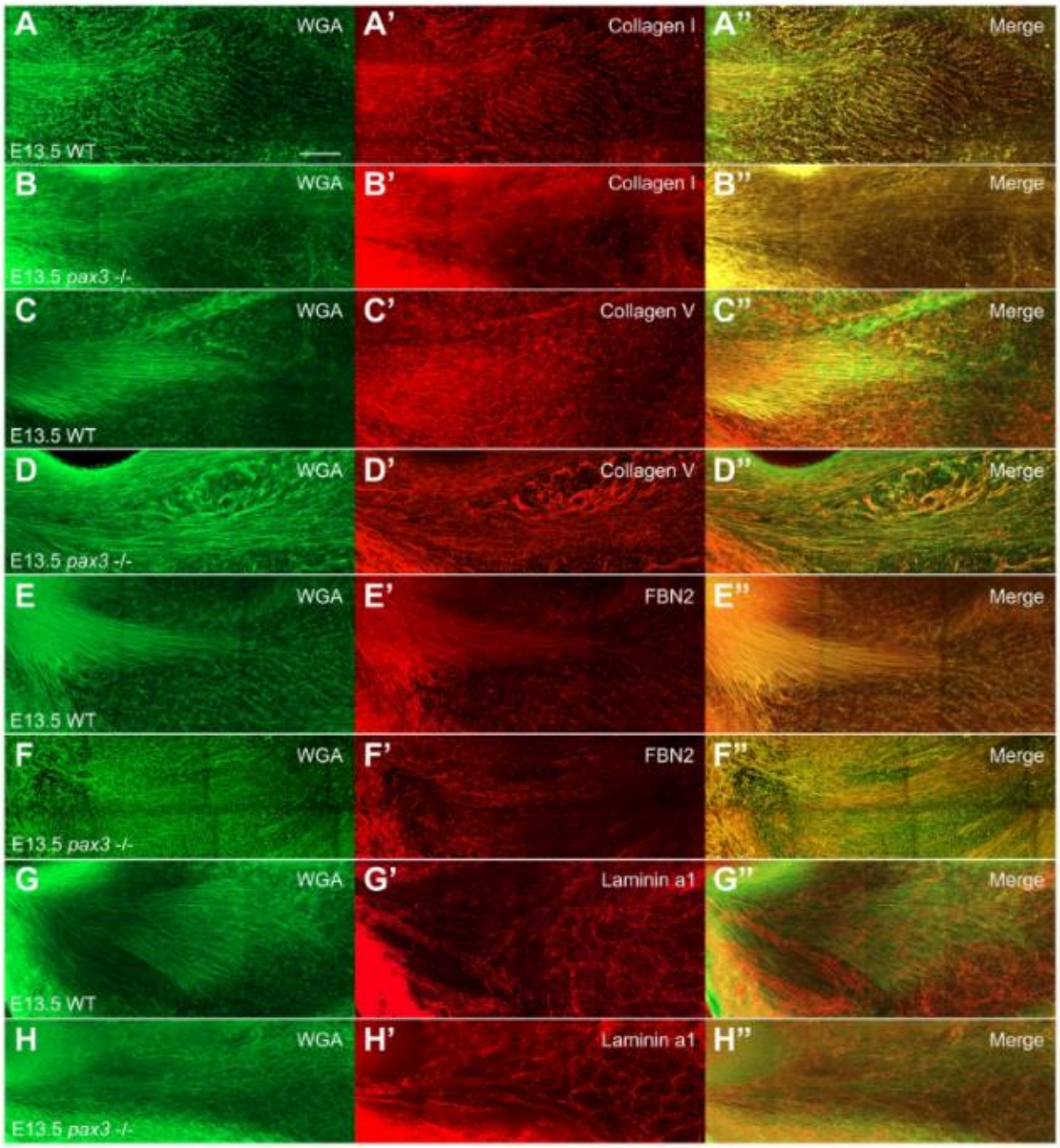

Figure 3.6. ECM fibers rich in type I collagen, type V collagen, and fibrillin-2. Decellularized forelimbs from WT (A, C, E, G) or Pax3-Cre/Cre mouse embryos (B, D, F, H) at E13.5 were stained with collagen I (A, B), collagen V (C, D), fibrillin-2 (FBN2) (E, F), and laminin α1 (G, H). Magnification = 20x. Scale bar = 100 µm.

3.5 Conclusion

The goal of this study was to identify the potential role of the ECM during early musculoskeletal development (E11.5 – E14.5) using the Pax3-Cre/Cre and Pax3-Cre/ZsGreen1+ mouse model. We used optical clearing and decellularization methods to see how individual ECM components are spatially distributed in the developing muscle, tendon, and MTJ. Importantly, we provided evidence that an ECM-based template, deposited before the formation of muscle, tendon, and MTJ at E11.5, played a role in directing the proper combinations between muscle and tendon, and delineated space for muscle formation, indicating ECM is a macromolecular network with not only structural but also instructive functions. Understanding how the links between muscle and tendon, and the role of ECM at their interface is essential in providing critical insight into the mechanisms that orchestrate musculoskeletal assembly and establish guidelines for developing regenerative medicine strategies that aim to restore these interfaces in diseased and damaged tissues. Our future research aims to investigate more finely the role of individual ECM components during forelimb musculoskeletal assembly within the developing embryo.

4. PREDICTING THE MECHANICAL PROPERTIES OF FIBRIN USING NEURAL NETWORKS TRAINED ON DISCRETE FIBER NETWORK DATA

This chapter is a draft of a manuscript currently in preparation for publication.

4.1 Abstract

Fibrin is an important extracellular matrix (ECM) component in the body, providing structural integrity to various tissues. It is also a common scaffold material used in tissue engineering. In this study, we proposed a new approach to develop microstructure-sensitive, yet flexible and numerically efficient macroscopic models by using representative volume element (RVE) simulations of discrete fiber networks (DFN) for the training of physically meaningful fully connected neural networks (FCNN). The FCNN was able to predict the mechanical behavior of fiber networks with various microstructures under different loads while imposing convexity on the strain energy function for numerical stability. Then, the trained FCNN was embedded in a commercial finite element (FE) software via a user material subroutine. This model thus linked the macroscopic, tissue-level scale and the microscopic, fiber-level scale. The training data consisted of stress-strain pairs obtained from micromechanical RVE simulations of uniaxial and multiple biaxial configurations of a wide range of fibrin microstructures. Following training, we tested the FCNN by comparing the prediction of the strain energy for a certain loading and microstructure to the ground-truth value from the DFN model. Finally, we implemented the FCNN in a general user material subroutine in the popular FE package Abaqus and tested the correct convergence of basic uniaxial and shear tests, as well as a more representative simulation related to ECM remodeling, which occurs during development, wound healing and regeneration. Our work demonstrates that neural networks can be trained by micromechanical simulations, which capture ECM network behavior based on microstructural mechanisms.

4.2 Introduction

It is well known that the biomechanical macroscopic behavior of both native and engineered tissues is largely determined by the properties of their underlying microstructural components.

Therefore, to allow for a better design of engineered tissues, it is meaningful to investigate the underlying microstructures and how they relate to the overall mechanical response of tissues. Fibrin is an important extracellular matrix (ECM) component in the body, providing structural integrity to various tissues. It is also a common scaffold material used in tissue engineering (Li et al., 2015). The fibrin network structure can be described by variables such as the thickness of the fibers, the number of branch points, the fiber length, and the volume fraction (Stylianopoulos & Barocas, 2007).

Due to its inherent multiscale nature, with the tissue dimension being in the centimeter length scale and the underlying fibrin network being in the micrometer length scale, our understanding of the tissue at the macroscopic scale depends on the mechanical behavior of the fibrin network at the microscopic scale. To enable the multiscale description, models of discrete fiber networks (DFN) in a representative volume element (RVE) have often been proposed. Such a micromechanical model based on volume average theory is assuming that the overall mechanical response of the material derives from the sum of the micro-behavior of its constituents, and thus provide the linkage between the fiber-level mechanics and the tissue-level behaviors (Agoram & Barocas, 2001; Driessen et al., 2005; Stylianopoulos & Barocas, 2007). This model, considering the heterogeneity and the fibers interactions, predicts the mechanical behavior of three-dimensional fibrin networks. Then this model is coupled to mechanical loads and deformations of the macroscopic tissue scale through a multiscale formulation. The coupling involves a homogenization procedure for the RVE models (Liu et al., 2016). The macroscale mechanics can be expressed with a continuum balance of linear momentum for large deformations applicable to soft materials and tissues. Numerically, the macroscale response can be efficiently modeled with the finite element (FE) framework. For a fully coupled model, there exists one RVE associated with each of the integration points of the FE simulation. However, this strategy of nesting DFN models within the FE framework for large-scale heterogeneous structures is extremely expensive and computationally prohibitive. Not surprisingly, their use has been limited (Alber et al., 2019; Reimann et al., 2019).

A myriad of strategies for model reduction has been implemented to predict the mechanical properties that balance computational cost and accuracy (Bhattacharjee & Matouš, 2016; Kerfriden et al., 2013; Liu et al., 2015; Michel & Suquet, 2016; Oliver et al., 2017). Particularly, machine learning (ML) methods have been extended to various problems of mechanics modeling and

multiscale simulations, e.g., modeling macroscopic material behavior by stress-strain curves obtained from micromechanical simulations (Reimann et al., 2019); approximating the surface response and deriving the macroscopic stress and tangent tensor components (Le et al., 2015); capturing the multiscale hydro-mechanical coupling effect of porous media with pores of varying sizes (Wang & Sun, 2018), and predicting the entire stress-strain behavior of binary composites (Yang et al., 2020), etc.

Since ML techniques, in particular, the neural network (NN) method, are capable of building meaningful relationships in data; With a sufficient amount of training data, this method is efficient in automatically discovering and capturing the underlying complex high-dimensional mapping from the feature vector (input) to the desired output without the need of manually deriving specific functional forms (Peng et al., 2020; Tepole et al., 2020). In this paper, we propose a novel multiscale modeling approach to develop microstructure-sensitive, yet flexible and numerically efficient macroscopic models by using RVE simulations of DFN for the training of fully connected neural networks (FCNN). The FCNN is then able to predict the mechanical response of various microstructures under different loads intelligently. In this way, the trained FCNN represents a new macroscopic constitutive relation. Firstly, the training data, which consisted of different stress-strain and strain–energy relationships obtained from micromechanical RVE simulations of uniaxial testing and biaxial testing of a wide range of fibrin microstructures were generated. In order to get derivatives of strain energy with respect to the strain invariants, a Gaussian process (GP) surrogate was trained. Then, the derivatives obtained from GP was adjusted in the optimization function. With these data, we trained a FCNN model to predict the mechanical properties (e.g. stress, energy, and their derivatives) of a composite based on its microstructures. Notably, the convexity, which is essential to ensure the model is physically meaningful with unambiguous mechanical characteristics and therefore improves numerical stability, especially when the FCNN is used in finite element simulations, was considered in the training process by defining the loss function specifically (i.e. requiring symmetric positive definiteness of the Hessian). Following training, we test the FCNN by comparing the prediction of the properties for a certain loading and microstructure to the ground truth DFN model. Finally, we implemented the FCNN in a general User Material Subroutine (UMAT) in the popular FE package Abaqus. The UMAT is defined for arbitrary FCNN, and the architecture of the FCNN, as well as the weights and biases defining the FCNN are specified in the input file as material properties. Our work

demonstrates that neural networks can be trained by micromechanical simulations, which capture ECM network behavior accurately and efficiently based on various complex microstructural mechanisms. The main features of our model are: the physics-based building block RVE with interpretable fitting parameters, the capability to extrapolate the structure-property relationship with elastic training data, and the convexity on the strain energy function for numerical stability. We anticipate that this work will enable the widespread use of multiscale simulations by reducing the computational cost without compromising accuracy.

4.3 Materials and Methods

4.3.1 Fibrin gels preparation and imaging

Porous polyethylene blocks were adhered to 6 mm × 12.5 mm frames using Loctite Super Glue Gel Control and used as anchor points for 2mg/mL fibrin gel. A custom three-dimensional (3D) printed mold was used to align the frame and to control the shape of fibrin gel as it polymerized so that a rectangular gel would form between the two porous polyethylene blocks. 14.15 mg/mL human fibrinogen (FIB3, Enzyme Research Laboratories) and 1 mg/mL Alexa Fluor 488 conjugated human fibrinogen (F13191, Molecular Probes) were thawed in a 37 °C water bath, mixed at a 1:10 fibrinogen content ratio, and diluted in PBS to achieve a 2 mg/mL fibrinogen solution. 1 µL 2M CaCl2 was added to the fibrinogen solution. 3.54 mg/mL, 3046 NIH units/mg of human alpha thrombin (HT 1002a, Enzyme Research Laboratories) was thawed, diluted to 1 Thrombin units (UT)/µL, and introduced to the 2 mg/mL fibrinogen solution at a concentration of 0.0004 UT/mg fibrinogen to initiate the fibrin gel polymerization. A total volume of 75 µL was added to the mold and allowed to gel for 15 minutes (min) at room temperature (RT). The gel structure was imaged using an upright Zeiss LSM 800 confocal (Carl Zeiss Microscopy) with a 20× water immersion Plan-Apochromat (NA = 1.0) objective. Confocal stacks were rendered in 3D using FIJI (NIH) (Figure 4.1).

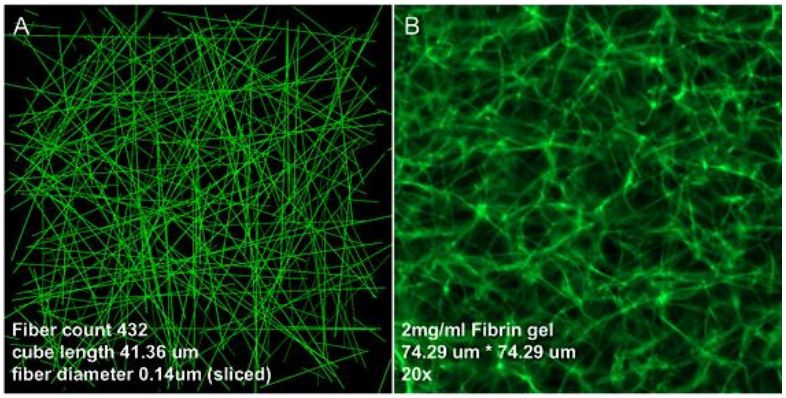

Figure 4.1. A microscale network model (A), was used to simulate the fibrin networks (B).

4.3.2 Discrete fiber network models

Fibrin networks consist of fibers of varying diameters, but usually between tens to hundreds of nanometers. In the model, the fibers are linked to each other through cross-links, and they can stretch, compress, or rotate at these points. Bending forces are not considered during fiber deformation as fibers are typically thin and long. The procedure for the generation of the networks was in a similar manner to previous efforts (Clague & Phillips, 1997; Stylianopoulos & Barocas, 2007). Namely, we seeded the three-dimensional RVE with random uniformly distributed nucleation points. Each point gave rise to two segments, which grow oppositely along with a randomly chosen direction sampled from a uniform distribution on the sphere. During fiber growth, the length of segments increased by a unit at each step. Also, at each step, a segment is checked to decide if it has exceeded the boundaries of the cube or has collided with another segment. At the point of the identified intersection or collision, a node was introduced, and the segment stopped growing. When the growth of all the segments stopped, the fibrillar network was defined.

Applying forces or deformations to the boundaries of the RVE leads to the deformation of the fibers inside of the network. The deformation of the network results in the generation of forces and energy on the fibers such that energy is minimized, and mechanical equilibrium is achieved at the RVE level. The energy in each fiber is

$$\psi_{\mathrm{f}} = \frac{\mathrm{k_f}}{2}\left(\lambda_f^2 - 1\right), \text{ with } \lambda_f = \frac{||\boldsymbol{x}_1 - \boldsymbol{x}_0||}{||\boldsymbol{X}_1 - \boldsymbol{X}_0||} \tag{4.1}$$

where $\boldsymbol{x}_0, \boldsymbol{x}_1$ are the deformed coordinates of the nodes making up the fiber, $\boldsymbol{X}_0, \boldsymbol{X}_1$ are the original coordinates, and k_f is a material constant that denotes stiffness of the fiber. The mechanical

equilibrium is obtained by searching for the deformed nodal coordinates of the fibers that minimize the total energy of all fibers combined. Only the inner crosslinks are allowed to move in order to find the equilibrium configuration. After finding the equilibrium configuration, the homogenized stress on the RVE is calculated based on the averaging volume theory (Stylianopoulos & Barocas, 2007). As the eq. (4.2) shows, the global (homogenized) value is the sum of the local element value multiplied with the corresponding volume, which is then scaled by the total volume of the RVE.

$$\boldsymbol{\sigma}_{\mathrm{ij}} = \frac{1}{\mathrm{V}} \int \hat{\sigma}_{ij}\, dV \tag{4.2}$$

In a discrete form,

$$\boldsymbol{\sigma}_{\mathrm{ij}} = \frac{1}{\mathrm{V}} \sum x_{\mathrm{i}}^{b} F_{j}^{b} \tag{4.3}$$

where V is the volume of the RVE, $\hat{\sigma}_{ij}$ is the microscopic stress tensor, $\boldsymbol{x}^b$ and $\boldsymbol{F}^b$ are the coordinates and forces at the boundary nodes. Based on the network geometry, two quantities of interest were identified as the best descriptors for microstructure: the volume fraction θ, and the fiber diameter φ. The range of the model parameters was obtained to span similar networks to those in the literature (Lai et al., 2012; Stylianopoulos & Barocas, 2007). Namely, the diameter φ was in the range of 20 nm to 500 nm, and the volume fraction θ was in the range 0.05% to 1.0%.

4.3.3 Hyperelastic mechanical behavior at the macroscale

In the multiscale formulation, the average stress $\boldsymbol{\sigma}$ of the homogenized RVE is linked to the average deformation gradient $\boldsymbol{F}$. The macroscopic deformation gradient, in turn, is also linked to the microscale. The tensor $\boldsymbol{F}$ describes the deformation of the RVE boundaries. Thus, the deformation of the RVE entails the existence of a microscale deformation field which in an average sense can be linked to a macroscopic deformation $\boldsymbol{F}$. In this manner, the macroscopic relationship $\boldsymbol{\sigma}(\boldsymbol{F})$ can be evaluated through the RVE model.

Under the assumption that the macroscopic material behavior is that of a hyperelastic material (Mihai et al., 2017a; Mihai & Goriely, 2015), we pose that the total strain energy Ψ obtained from the sum of all the fibers is itself a function of the macroscopic deformation invariants of the left Cauchy Green deformation tensor $\boldsymbol{b} = \boldsymbol{F}\boldsymbol{F}^T$. Furthermore, assuming a decoupled formulation for the strain energy, it can be split into

$$\Psi = \Psi_{iso}\left(\hat{I}_1, \hat{I}_2\right) + \Psi_{vol}(J) \tag{4.4}$$

where $\hat{I}_1 = \widehat{\boldsymbol{b}}: \boldsymbol{I}$, $\hat{I}_2 = \frac{1}{2}(\hat{I}_1^2 - \widehat{\boldsymbol{b}}^2: \boldsymbol{I})$, $\widehat{\boldsymbol{b}} = J^{-2/3}\boldsymbol{b}$, J = det(**F**). Soft tissues are assumed to be nearly incompressible due to their high immovable water content. Restricting our attention to plane stress loading of the RVE, and enforcing full incompressible behavior through the corresponding pressure Lagrange multiplier, the overall stress of the RVE takes the form

$$\boldsymbol{\sigma} = p\boldsymbol{I} + 2\psi_1 J^{-1}\widehat{\boldsymbol{b}} + 2\psi_2 J^{-1}(\hat{I}_1\widehat{\boldsymbol{b}} - \widehat{\boldsymbol{b}}^2) \tag{4.5}$$

where $\psi_1 = \partial\Psi_{\text{iso}}(\hat{I}_1, \hat{I}_2)/\partial\hat{I}_1$ and $\psi_1 = \partial\Psi_{\text{iso}}(\hat{I}_1, \hat{I}_2)/\partial\hat{I}_2$ are the derivatives of the isochoric part of the strain energy with respect to the invariants of $\widehat{\boldsymbol{b}}$.

Therefore, the goal of the homogenization process under the assumption of a macroscopic hyperelastic behavior entails learning the functions $\psi_1(\hat{I}_1, \hat{I}_2)$ and $\psi_2(\hat{I}_1, \hat{I}_2)$. As opposed to previous approaches that have proposed analytical forms for the strain energy and its derivatives (Mihai et al., 2017b; Mihai & Goriely, 2017), in this manuscript, the RVE is subject to different deformations $\boldsymbol{F}^{(i)}$ to learn the corresponding mechanical response without an analytical approximation. The deformation gradients imposed on the RVE satisfy a priori the incompressible condition. For each imposed deformation i the invariants $\hat{I}_1^{(i)}, \hat{I}_2^{(i)}$ can be computed. The stress from the RVE is then forced to satisfy the plane stress condition by solving for the pressure Lagrange multiplier for that deformation $p^{(i)}$. The result is a total stress tensor computed from the RVE simulation $\boldsymbol{\sigma}^{(i)}$, a definition of the stress tensor for a hyperelastic material eq. (4.5), and the total strain energy accumulated on the fibers $\Psi^{(i)}$. The values of the two functions of interest, $\psi_1(\hat{I}_1, \hat{I}_2)$ and $\psi_2(\hat{I}_1, \hat{I}_2)$, are not directly available. In order to learn these functions, we first use the known quantities $\boldsymbol{\sigma}^{(i)}$ and $\Psi^{(i)}$ calculated for the different deformations $\hat{I}_1^{(i)}, \hat{I}_2^{(i)}$ to determine the corresponding ψ_1 and ψ_2 values. Then these values are used to train a FCNN.

4.3.4 Obtain derivatives by Gaussian Process and optimization

A GP is a stochastic process whose value at any collection of data points can be described with a multivariate normal distribution (Seeger, 2004). We start by assuming that we have a data set comprised of input-output pairs D = $\{(\hat{I}_1, \hat{I}_2), \Psi\}$. Specifically, we let each component of $\Psi(\hat{I}_1, \hat{I}_2)$ be a Gaussian process. That is, the vector $[\Psi(\hat{I}_1, \hat{I}_2)]$ has a multivariate normal distribution for any collection of points I_1, I_2; and thus a realization of the vector $[\Psi(\hat{I}_1, \hat{I}_2)]$ can be interpreted as a realization of Ψ_i (i.e. a sample function) that is evaluated at I_{1_i}, I_{2_i}. As a

Gaussian process is fully determined by a mean function and a covariance function, we standardized the dataset and worked with zero-mean Gaussian process priors of the form f ∼ GP (0, k(𝕀, 𝕀′)), where 𝕀 = ($\hat{I}_1$, $\hat{I}_2$) and 𝕀′ = ($\hat{I}'_1$, $\hat{I}'_2$). and k(𝕀, 𝕀′) is a covariance kernel function. The most commonly used kernel in machine learning (implemented in GPy (*SheffieldML/GPy: Gaussian Processes Framework in Python*, 2018)) is the Gaussian-form radial basis function (RBF) kernel (Schölkopf & Tsuda, 2019). It is also commonly referred to as the exponentiated quadratic or squared exponential kernel. Using such a kernel for GP regression and increasing the length scale would mean making the regression smoother. After fitting with Gaussian process regression (GPR) to the total strain energy Ψ, the initial derivatives ψ_1^0 and ψ_2^0 were acquired from the gradient of the strain-energy density function, which took advantage of derivative information since the derivative of a GP is also a GP which is analytically available (Frankel et al., 2019). Specifically, the covariance between the derivatives of the stress-energy density between two different points in invariant space, 𝕀 and 𝕀′, can be evaluated as

$$\mathrm{Cov}\left(\frac{\partial \Psi(\mathbb{I})}{\partial \hat{I}_i}, \Psi(\mathbb{I}')\right) = \frac{\partial \mathrm{k}(\mathbb{I},\mathbb{I}')}{\partial \hat{I}_i} \tag{4.6}$$

$$\mathrm{Cov}\left(\frac{\partial \Psi(\mathbb{I})}{\partial \hat{I}_i}, \frac{\partial \Psi(\mathbb{I}')}{\partial \hat{I}'_j}\right) = \frac{\partial^2 \mathrm{k}(\mathbb{I},\mathbb{I}')}{\partial \hat{I}_i \partial \hat{I}'_j} \tag{4.7}$$

Using these relations, a GP may be formed simultaneously over Ψ at the grounding point and its derivatives over the dataset by using the block covariance matrix

$$k_\Psi(\mathbb{I}, \mathbb{I}') = \begin{bmatrix} \frac{\partial^2 \mathrm{k}}{\partial \hat{I}_1 \partial \hat{I}'_1} & \frac{\partial^2 \mathrm{k}}{\partial \hat{I}_1 \partial \hat{I}'_2} \\ \frac{\partial^2 \mathrm{k}}{\partial \hat{I}_2 \partial \hat{I}'_1} & \frac{\partial^2 \mathrm{k}}{\partial \hat{I}_2 \partial \hat{I}'_2} \end{bmatrix} \tag{4.8}$$

These derivatives, however, ignore the stress information that was obtained from solving the RVE simulation. As described in the previous section, the stress from the RVE satisfies incompressible plane stress behavior and is also linked to the derivatives of the strain energy, providing additional constraints. Then, we obtained the corrected values of the functions ψ_1^*, ψ_2^* by minimizing Eq_1^2 + Eq_2^2 + Eq_3^2 + Eq_4^2 + Eq_5^2 with the open-source Python package SciPy (Virtanen et al., 2020).

Eq_1: -ρ + 2 ψ_1 λ_x^2 - 2 ψ_2 λ_x^{-2} - σ_{xx}

Eq_2: -ρ + 2 ψ_1 λ_y^2 - 2 ψ_2 λ_y^{-2} - σ_{yy}

Eq_3: -ρ + 2 ψ_1 λ_z^2 - 2 ψ_2 λ_z^{-2} - σ_{zz}

Eq_4: ψ_1 - ψ_1^0

Eq_5: ψ_2 - ψ_2^0 (4.9)

where ρ is the pressure Lagrange multiplier needed for plane stress, λ_x, λ_y are the variables controlling the deformation of the RVE and are in the range of 1.0 to 1.25, and $\lambda_z = \frac{1}{\lambda_x * \lambda_y}$ is needed for incompressibility. The first three constraints in eq. (4.9) are a reformulation of eq. (4.5) for a biaxial deformation given by the principal stretches λ_x, λ_y. In other words, to generate the data we do not sample directly the invariants of the Cauchy Green deformation tensor, instead, we impose different combinations of $\lambda_x^{(i)}$, $\lambda_y^{(i)}$. For each of these deformations, the RVE model is solved for the stress, the pressure, and the total energy. The total energy is fitted with the GP to obtain preliminary guesses for the derivatives ψ_1^0 and ψ_2^0. The final values of the derivatives Ψ_1^* and Ψ_2^* are solved through the optimization problem in eq. (4.9).

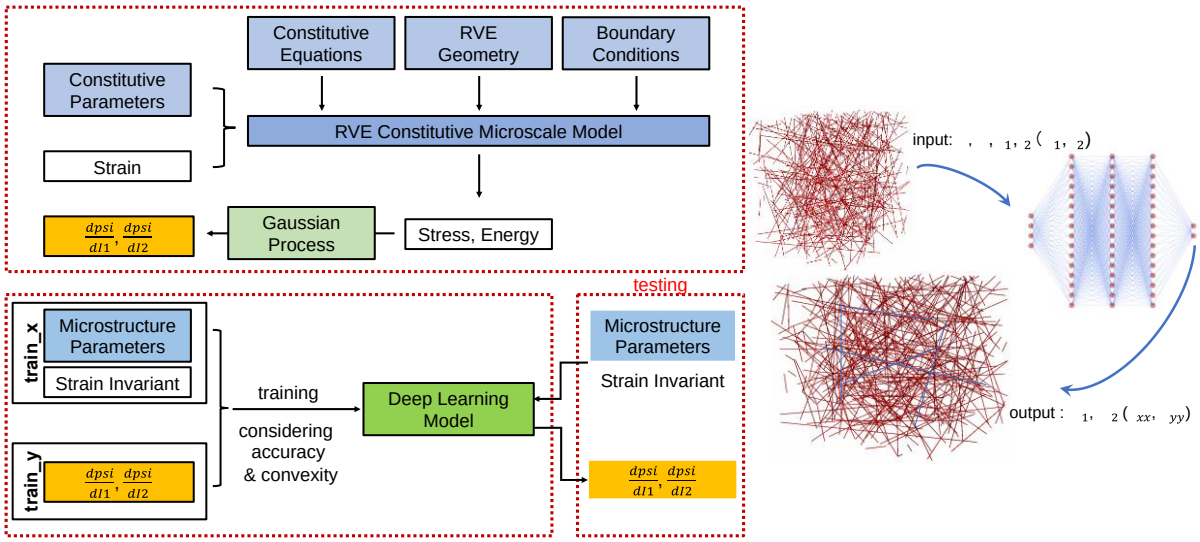

Figure 4.2. The framework for training a ML-based microscale model.

4.3.5 Fully connected neural network

We constructed a NN that predicts the stress tensor directly when the principal stretches λ_1 and λ_2 are the input (shown in

Figure 4.4. A and B). However, this network only works directly in the coordinate system for which the state of stress is a plane-stress biaxial state of deformation. This model would have limited applicability in a FE solver. Instead, it would be desirable to have a strain energy function in terms of the strain invariants $\Psi(\hat{I}_1, \hat{I}_2)$. then, the derivatives of the strain energy $\psi_1 = \partial\Psi(\hat{I}_1, \hat{I}_2)/\partial\hat{I}_1$, and $\psi_2 = \partial\Psi(\hat{I}_1, \hat{I}_2)/\partial\hat{I}_2$ can be used to compute the stress. The invariant approach is independent of the coordinate system and thus convenient for the FE implementation. Therefore, while we still construct the NN to predict stress, most of the analyses and the FE implementation is done with the invariant-based NN. Thus, unless otherwise specified, the "FCNN model" referred to the one used for strain energy ψ_1 and ψ_2 prediction.

Creating a customized loss function for biaxial testing

The goal of the FCNN model was to establish the nonlinear mapping between $[\hat{I}_1, \hat{I}_2, \theta, \varphi]$ and $[\psi_1, \psi_2]$ (Figure 4.2). As convex strain energy function plays significant roles in material stability and numerical stability, physics-related constraints needed to be incorporated into the training process to ensure that convexity of the strain energy density (i.e., the strain energy density should be at a minimum (zero) when there is no deformation) was achieved by the FCNN constitutive model. Thus, we constructed customized loss functions not only considered the accuracy of the prediction but also required symmetry positive definiteness of the tangent stiffness matrix (Hessian matrix). Since predicting the mechanical behavior is a regression problem, the difference between the ground truth and the predicted ψ_1, ψ_2 was measured by a weighted combination of mean squared error (MSE), mean absolute error (MAE), and mean absolute percentage error (MAPE) loss function,

$$L^{(n)}_{MSE\_\psi 1} = (\psi_1^{(n)} - \widehat{\psi_1^{(n)}})^2$$

$$L^{(n)}_{MAE\_\psi 1} = \left|\psi_1^{(n)} - \widehat{\psi_1^{(n)}}\right|$$

$$L^{(n)}_{MAE\_\psi 2} = \left|\psi_2^{(n)} - \widehat{\psi_2^{(n)}}\right|$$

$$L^{(n)}_{MAPE\_\psi 1} = 100\% * \left|\frac{\psi_1^{(n)} - \widehat{\psi_1^{(n)}}}{\psi_1^{(n)}}\right| \tag{4.10}$$

where n is the data point index, $\widehat{\psi_{1\ or\ 2}^{(n)}}$ is the predicted value ψ_1, ψ_2 for the ith sample, and $\psi_{1\ or\ 2}^{(n)}$ is the corresponding ground-truth value.

$$L_{Accuracy}^{(n)} = 100 * L_{MAE\_\psi 2}^{(n)} + 10 * L_{MAE\_\psi 1}^{(n)} + L_{MSE\_\psi 1}^{(n)} + L_{MAPE\_\psi 1}^{(n)} \quad (4.11)$$

As a result, a weighted sum of the above terms was set as the loss function to measure the accuracy of a model. The weights were determined by taking took two things into consideration: (1) the relative equal importance of ψ_1 and ψ_2; (2) the overall accuracy performance on the training set and validation set.

As for ensuring the convexity, the Hessian matrix (H) of the strain energy function can be expressed as:

$$\mathrm{H} = \begin{bmatrix} \frac{\partial^2 \Psi}{\partial \hat{I}_1 \partial \hat{I}_1} & \frac{\partial^2 \Psi}{\partial \hat{I}_1 \partial \hat{I}_2} \\ \frac{\partial^2 \Psi}{\partial \hat{I}_2 \partial \hat{I}_1} & \frac{\partial^2 \Psi}{\partial \hat{I}_2 \partial \hat{I}_2} \end{bmatrix} = \begin{pmatrix} \frac{\partial \psi_1}{\partial \hat{I}_1} & \frac{\partial \psi_1}{\partial \hat{I}_2} \\ \frac{\partial \psi_2}{\partial \hat{I}_1} & \frac{\partial \psi_2}{\partial \hat{I}_2} \end{pmatrix} \quad (4.12)$$

Positive definiteness for H requirements (Prussing, 1986): $\frac{\partial^2 \Psi}{\partial I_1 \partial I_1} > 0$ and $\frac{\partial^2 \Psi}{\partial \hat{I}_1 \partial \hat{I}_1} * \frac{\partial^2 \Psi}{\partial \hat{I}_2 \partial \hat{I}_2} - \frac{\partial^2 \Psi}{\partial \hat{I}_1 \partial \hat{I}_2} * \frac{\partial^2 \Psi}{\partial \hat{I}_2 \partial \hat{I}_1} > 0$; thus the positive definiteness was taken care of by a loss function at each data point n:

$$L_{posd}^{(n)} = \max(0, -\frac{\partial^2 \Psi}{\partial \hat{I}_1 \partial \hat{I}_1}) + \max(0, -(\frac{\partial^2 \Psi}{\partial \hat{I}_1 \partial \hat{I}_1} * \frac{\partial^2 \Psi}{\partial \hat{I}_2 \partial \hat{I}_2} - \frac{\partial^2 \Psi}{\partial \hat{I}_1 \partial \hat{I}_2} * \frac{\partial^2 \Psi}{\partial \hat{I}_2 \partial \hat{I}_1})) \quad (4.13)$$

Symmetry requirement for H: $\frac{\partial^2 \Psi}{\partial \hat{I}_1 \partial \hat{I}_2} = \frac{\partial^2 \Psi}{\partial \hat{I}_2 \partial \hat{I}_1}$, thus symmetry was taken care of by a loss function at each data point n: $L_{symm}^{(n)} = \left| \frac{\partial^2 \Psi}{\partial \hat{I}_1 \partial \hat{I}_2} - \frac{\partial^2 \Psi}{\partial \hat{I}_2 \partial \hat{I}_1} \right|$ (4.14)

Hence, the final loss function of the convexity constraints can be obtained by adding $L_{MAPE}^{(n)}$, $L_{posd}^{(n)}$, and $L_{symm}^{(n)}$ with a weight α_1 and α_2:

$$L = \frac{1}{N} \sum_{n=1}^{N} (100 * L_{MAE\_\psi 2}^{(n)} + 10 * L_{MAE\_\psi 1}^{(n)} + L_{MSE\_\psi 1}^{(n)} + L_{MAPE\_\psi 1}^{(n)} + \alpha_1 L_{posd}^{(n)} + \alpha_2 L_{symm}^{(n)}) \quad (4.15)$$

where N is the number of data points in the training dataset. As α_1 controls the convexity of the function, the value of α_1 (the importance of $L_{posd}^{(n)}$) should be larger than or equal to α_2. The final α_1 and α_2 were chosen using a grid search based on validation results. Consequently, the combined loss function is a function of the weights of each layer in the FCNN model. The goal of training is to find the optimal weights in the FCNN model by minimizing the loss function on the training dataset.

FCNN Architectures and training

A FCNN network was trained to predict the network mechanical behaviors based on the given microstructure and loading. The training input to the FCNN was a vector containing $\hat{I}_1$, $\hat{I}_2$, θ, and φ. These values were normalized to have a mean of 0.0 and a standard deviation of 1.0 to smoothen, stabilize the training process and make better predictions (Ioffe & Szegedy, 2015). The training output was either stress σ (

Figure 4.4. A, B) or ψ_1, ψ_2. The Adam optimization algorithm (Kingma & Ba, 2015) was applied to train the networks and update the FCNN weights during backpropagation (Rumelhart et al., 1986). The initial learning rate was set as 0.0001 with a momentum decay of 0.9. The training and validation data splits were 85% and 15%. The total number of observations was 132,000 for 1,100 DFN networks (data that had extreme ψ_1, ψ_2, or was unsolvable with SciPy during optimization was filtered out before training).

A typical FCNN consists of an input layer, one or more hidden layers, and an output layer. Here we trained and evaluated an FCNN with 3 hidden layers of dimensions 8, 8, and 16 respectively, and 1 output layer. The activation function used was ReLu (Nair & Hinton, 2010)(Table 4.1).

The training was implemented using Keras (Chollet et al., 2018) with a TensorFlow (Abadi et al., 2016) backend on a hardware platform with the following specifications: Overclocking 5.0 GHz Intel i9 processor, 32 GB DDR4/2666 MHz memory, and Nvidia GeForce GTX 1080. The batch size, which controls the number of samples to be propagated through the network at a time

was set as 64 to avoid local minima, enhance generalization performance, and improve the optimization convergence (Keskar et al., 2016).

Table 4.1. The structure and trainable parameters for the FCNN model.

```
Model: "sequential"
_________________________________________________________________
Layer (type)                 Output Shape              Param #
=================================================================
dense (Dense)                (None, 8)                 40
_________________________________________________________________
activation (Activation)      (None, 8)                 0
_________________________________________________________________
dense_1 (Dense)              (None, 8)                 72
_________________________________________________________________
activation_1 (Activation)    (None, 8)                 0
_________________________________________________________________
dense_2 (Dense)              (None, 16)                144
_________________________________________________________________
activation_2 (Activation)    (None, 16)                0
_________________________________________________________________
dense_3 (Dense)              (None, 2)                 34
_________________________________________________________________
activation_3 (Activation)    (None, 2)                 0
=================================================================
Total params: 290
Trainable params: 290
Non-trainable params: 0
```

FCNN testing data

The testing data used in 4.4.3. was generated separately from the training and validation data. Specifically, testing data was gathered either by using five pairs of seeds number and DFN cubic length, while keeping the fiber diameter φ to be 100 nm, to generated 100 DFNs with volume fraction $\theta \approx 0.3\%$ (

Figure 4.4. A, C, E), or by first choosing different pairs of φ and θ, then for each microstructure, 20 DFNs was generated (

Figure 4.4. B, D, F-J). Thus, the mean value and variance of mechanical responses for different microstructure could be captured. Note that the exact volume fraction θ (e.g. a network with θ exactly equal to 0.3%) could not be controlled while generating a network due to some randomness. What we control were the seeds number, fiber diameter, and RVE cubic length, which produced a network of very similar θ to what we want but not exact. Thus, we use "≈" to indicate a θ with almost exactly the same value as a given number.

4.3.6 Finite element implementation

The FCNN was implemented in the nonlinear FE package Abaqus Standard (Rhode Island, United States). A User Material Subroutine (UMAT) was implemented. Rather than hard-coding the specific FCNN, the UMAT function takes in the network architecture, and the weights and biases values as material parameters which are assigned outside of the UMAT function, in the input file. In the UMAT function, the FCNN is constructed and evaluated based on these material properties. This approach gives flexibility, such that different regions in a finite element model can be assigned different FCNNs as their material behavior without the need for multiple user subroutines. In the UMAT, the deformation gradient $\boldsymbol{F}$ is also passed as an input. Based on this deformation gradient, the corresponding right Cauchy Green deformation $\widehat{\boldsymbol{b}}$ and its invariants $\hat{I}_1, \hat{I}_2$

are computed. The microstructure parameters θ, φ are also passed as material properties. The vector $\theta, \varphi, \hat{I}_1, \hat{I}_2$ is the input to the FCNN, which is then evaluated to compute ψ_1 and ψ_2. Briefly, for a given layer i of the FCNN, the output is the vector

$$y_i = g(W_i^T x_i + b_i) \tag{4.16}$$

where x_i is the input vector, W_i is the matrix of weights for this layer, b_i is the vector of biases, and $g(\cdot)$ is the activation function. In addition to computing the functions ψ_1 and ψ_2, their derivatives are needed for the elasticity tensor needed in the Newton iterations of the FE solver. For a given layer, the gradient output is

$$J_i = \text{diag}(g'(W_i^T i_i + b_i))W^T J_{i-1} \tag{4.17}$$

with the initial gradient for the first layer is just the identity matrix. For the case of four inputs, the first gradient is the 4×4 identity matrix. The function $g'(\cdot)$ is the derivative of the activation function. At the end of the evaluation, the gradient contains the derivative of the functions ψ_1 and ψ_2 with respect to all inputs. In this case, since there are 4 inputs, the final gradient output from the FCNN is a 2×4 matrix. However, only the last two columns are needed for the elasticity tensor. The last two columns of this gradient contain the Hessian in eq. (4.12). After evaluation of the FCNN, the isochoric stress is evaluated as

$$\boldsymbol{\sigma_{iso}} = \frac{1}{J}\mathbb{P}:\bar{\boldsymbol{\sigma}} \tag{4.18}$$

where the projection tensor is $\mathbb{P} = \mathbb{I} - \frac{1}{3}\boldsymbol{I} \otimes \boldsymbol{I}$, $\mathbb{I}$ is the fourth-order identity tensor and $\boldsymbol{I}$ is the second-order identity tensor. Additionally

$$\bar{\boldsymbol{\sigma}} = 2\left(\psi_1 + \hat{I}_1\psi_2\right)\hat{\boldsymbol{b}} - 2\Psi_2\hat{\boldsymbol{b}}^2 \tag{4.19}$$

The full stress tensor is the sum of this isochoric contribution and a volumetric contribution. The isochoric contribution can be calculated based on the FCNN evaluation. The volumetric contribution was not learned from the RVE simulations since incompressibility was imposed. This part of the strain energy and corresponding stress is implemented independently of the FCNN. For instance, currently, the volumetric part of the stress is computed as

$$\boldsymbol{\sigma_{vol}} = p\boldsymbol{I}, p = \frac{\partial \Psi_{vol}}{\partial J} = 2K(J-1)J \tag{4.20}$$

with K the bulk modulus parameter. The consistent tangent can be derived independently of the material model, simply by knowing the second derivatives of the strain energy function, which are also output from the FCNN. The following terms are used for ease of notation of the total tangent

$$\delta_1 = 4(\psi_2 + \psi_{11} + 2\hat{I}_1\psi_{12} + \hat{I}_1^2\psi_{22})$$
$$\delta_2 = -4(\psi_{12} + \hat{I}_1\psi_{22})$$
$$\delta_3 = 4\psi_{22}$$
$$\delta_4 = -4\psi_2 \tag{4.21}$$

where $\psi_{11}, \psi_{12}, \psi_{21}, \psi_{22}$ are the second derivatives that appear in the Hessian in eq. (4.12). The isochoric part of the elasticity tensor is

$$J\mathbb{c}_{iso} = \delta_1\left(\hat{\boldsymbol{b}} \otimes \hat{\boldsymbol{b}} - \frac{1}{3}\hat{I}_1(\hat{\boldsymbol{b}} \otimes \boldsymbol{I} + \boldsymbol{I} \otimes \hat{\boldsymbol{b}}) + \frac{1}{9}\hat{I}_1^2\boldsymbol{I} \otimes \boldsymbol{I}\right)$$
$$+\delta_2\left(\hat{\boldsymbol{b}} \otimes \hat{\boldsymbol{b}}^2 + \hat{\boldsymbol{b}}^2 \otimes \hat{\boldsymbol{b}} - \frac{1}{3}\mathrm{tr}\hat{\boldsymbol{b}}^2(\hat{\boldsymbol{b}} \otimes \boldsymbol{I} + \boldsymbol{I} \otimes \hat{\boldsymbol{b}}) - \frac{1}{3}\hat{I}_1(\hat{\boldsymbol{b}}^2 \otimes \boldsymbol{I} + \boldsymbol{I} \otimes \hat{\boldsymbol{b}}^2) + \frac{2}{9}\hat{I}_1\mathrm{tr}\hat{\boldsymbol{b}}^2\boldsymbol{I} \otimes \boldsymbol{I}\right)$$
$$+\delta_3\left(\hat{\boldsymbol{b}}^2 \otimes \hat{\boldsymbol{b}}^2 - \frac{1}{3}\mathrm{tr}\hat{\boldsymbol{b}}^2(\hat{\boldsymbol{b}}^2 \otimes \boldsymbol{I} + \boldsymbol{I} \otimes \hat{\boldsymbol{b}}^2) + \frac{1}{9}(\mathrm{tr}\,\hat{\boldsymbol{b}}^2)^2\boldsymbol{I} \otimes \boldsymbol{I}\right)$$
$$+\delta_4(\hat{\boldsymbol{b}} \,\overline{\otimes}\, \hat{\boldsymbol{b}} - \tfrac{1}{3}(\hat{\boldsymbol{b}}^2 \otimes \boldsymbol{I} + \boldsymbol{I} \otimes \hat{\boldsymbol{b}}^2) + \tfrac{1}{9}(\hat{\boldsymbol{b}}{:}\hat{\boldsymbol{b}})\boldsymbol{I} \otimes \boldsymbol{I}) \tag{4.22}$$

where the following special dyadic product was used $(\cdot)_{ij}\,\overline{\otimes}\,(\circ)_{kl} = (*)_{ikjl}$. The volumetric contribution of the elasticity tensor is

$$\mathbb{c}_{vol} = \left(p + J\frac{dp}{dJ}\right)\boldsymbol{I} \otimes \boldsymbol{I} - 2p\boldsymbol{I}\,\overline{\otimes}\,\boldsymbol{I} \tag{4.23}$$

Finally, Abaqus requires a correction of the elasticity tensor

$$\mathbb{c}_{abauqs} = \mathbb{c}_{iso} + \mathbb{c}_{vol} + \tfrac{1}{2}(\boldsymbol{\sigma}\,\overline{\otimes}\,\boldsymbol{I} + \boldsymbol{I}\,\overline{\otimes}\,\boldsymbol{\sigma} + \boldsymbol{\sigma}\,\underline{\otimes}\,\boldsymbol{I} + \boldsymbol{I}\,\underline{\otimes}\,\boldsymbol{\sigma}) \tag{4.24}$$

in which an additional tensor product is defined as $(\cdot)_{ij}\,\underline{\otimes}\,(\circ)_{kl} = (*)_{ilk}$. In summary, the architecture, weights, and biases of the FCNN are passed to the UMAT subroutine as material parameters, and the FCNN is evaluated given the current deformation gradient to output ψ_1, ψ_2 and their derivatives, which are enough to compute the stress and elasticity tensor needed for the FE solver.

4.4 Results

4.4.1 Evaluation of the training data

Uniaxial simulation

Our approach to model the fibrin fiber network was similar to previously published work (Lai et al., 2012; Lin & Gu, 2015; Stylianopoulos & Barocas, 2007). A single fiber was modeled as elastic beams that resist stretching, and crosslinks were modeled as a free rotating joint. Thus,

comparing the results from our model to the curve from these models allows us to check our DFN model against well-established methods. As a comparison, similar stress was observed when the RVE was stretched to a similar ratio as in the literature, which provides confidence in the implementation of the DFN model in the RVE. As a small network (small cubic length) with a smaller number of fibers could have the same volume fraction as a large network (large cubic length) with a larger number of fibers, a network with the same pair of microstructure parameters θ and φ, could be generated in many different ways. We found that networks with the same homogenized microstructure variables showed variability in uniaxial simulation results. For 110 networks with $\theta \approx 0.3\%$ (0.297% to 0.303%) and $\varphi = 100$ nm, the nonlinear relationship of stress over stretch was seen with a higher slope under higher stretch. Homogeneous deformations were obtained. At a stretch of $\lambda_x = 1.2$, for example, the mean (± S.D.) stress was 1.45 kPa ± 0.33 kPa (Figure 4.3.A). The uncertainty in the value of stress was dependent on the relative number of degrees of freedom, *i.e.* the number of inner nodes with respect to total nodes (Figure 4.3.B). A decreased variance with a higher degree of freedom was observed. While for a given microstructure θ, φ, there was variability, a consistent trend was observed with changes in microstructure: decreasing fiber diameter led to increased stress, almost independently of volume fraction (Figure 4.3.C). While this may seem counterintuitive, we remarked that the stiffness k_f was kept constant (0.02 kPa), and thus decreasing φ resulted in more, equally stiff fibers.

Biaxial simulation

In addition to the uniaxial simulation, a biaxial test was also performed. λ_x and λ_y, representing the stretch ratio in the x and y direction, were varied from 1.00 up to 1.25 with an interval of 0.025. Thus, 121 data points were collected for each network structure. As a result of 110 networks with $\theta \approx 0.3\%$ and $\varphi = 100$ nm, the strain energy density function Ψ for varying λ_x, while $\lambda_y = 1.0$ (off-biaxial) was depicted in Figure 4.3.D. In the figure, the data were shown as the mean value in the dashed blue line with the range of corresponding confidence interval in red shading. When $\lambda_x = 1.0$, the strain was not applied to the simulated network, all fibrils were perfectly straight and oriented in random directions, stress and strain energy were equal to zero for all the networks without any variation. As strain was increasingly applied, the strain energy increased, which was consistent with the nonlinearity in the stress curve. There was some

uncertainty in the mechanical responses, and these uncertainties increased as the stretch increased, which was expected due to the stress being a linear combination of the possibly nonlinear functions ψ_1, ψ_2 and the nonlinear deformation tensor $\boldsymbol{b}$. As for the relationship between strain energy density and the percentage of degrees of freedom, a slight decrease in the variation of Ψ could be found as the degree of freedom increased. This trend of convergence was not as obvious as in the stress (Figure 4.3.B). When the microstructure varies, there was no obvious changing pattern for Ψ. In general, networks with low volume fraction exhibited higher energy density and vice versa. Networks with higher fiber diameter tended to have lower energy density. The overall plots for ψ_1 and ψ_2 had similar trends. As ψ_1 and $\psi_2$were the derivate of Ψ respect to $\hat{I}_1, \hat{I}_2$ respectively, the value did not change much, and the standard deviation remained relatively constant across the different stretch ratios (Figure 4.3.G, J). This is consistent with the notion that the derivative functions ψ_1 and ψ_2 represent the material behavior and should have a constant variance independent of deformation, whereas the stress has increasing variance due to the nonlinear deformation $\boldsymbol{b}$. The plots for the percentage of degree of freedoms also revealed a similar stable pattern for the derivatives of the strain energy. The values of ψ_1 and ψ_2 were concentrated when the percentage of degree of freedom increased from 20% to 90% (Figure 4.3.H, K). The relationships between ψ_1, ψ_2 and microstructure (Figure 4.3.I, L) had a similar transition to observations from the stress (Figure 4.3.C). Basically, the data for ψ_1, ψ_2 were found to decreased as the diameter of fiber φ increased.

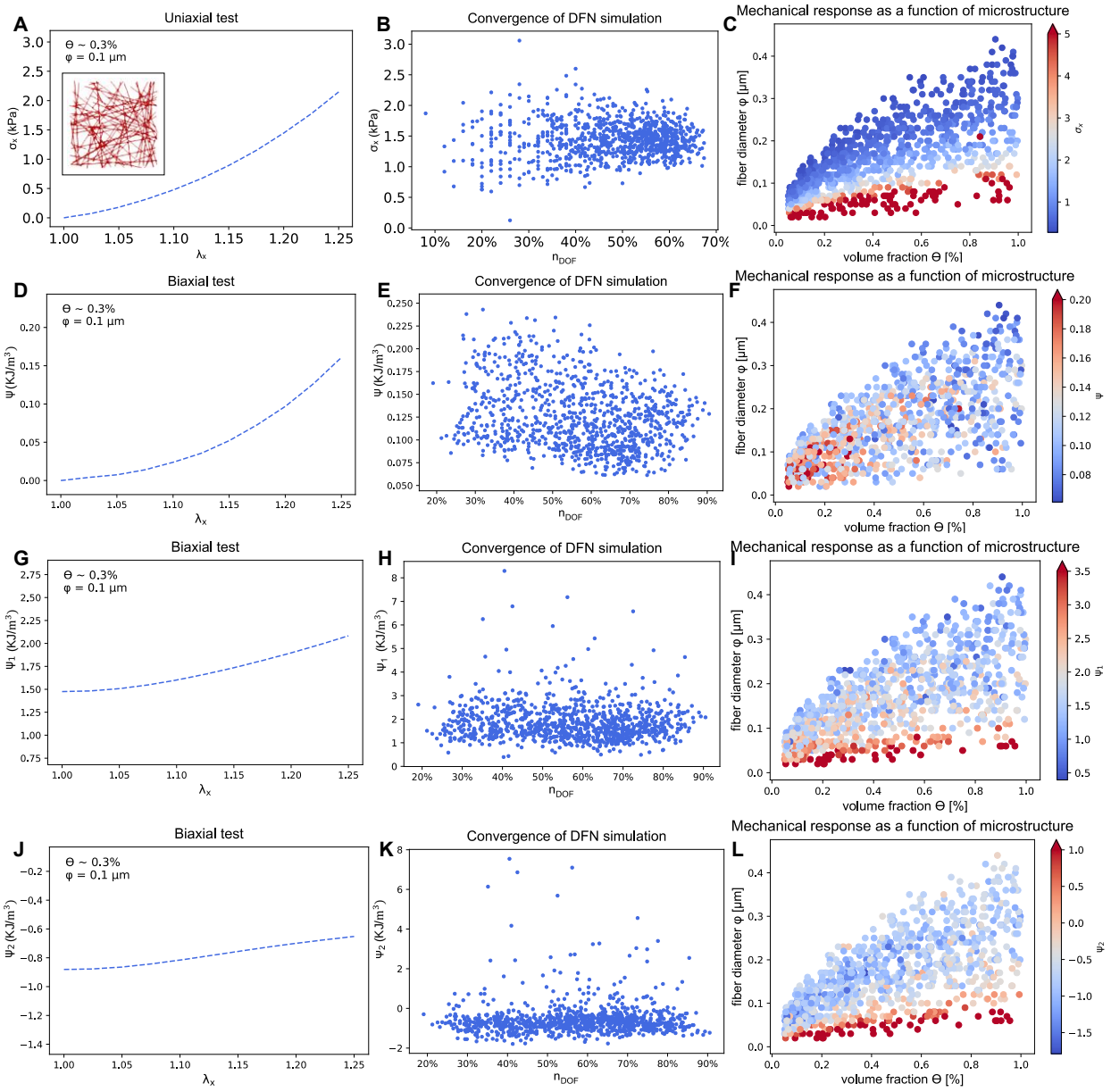

Figure 4.3. Analysis on the variation and distribution of the training data. In uniaxial test, (A) uncertainty of stress σ_x from 110 DFN with the same homogenized microstructure, the dashed blue line was the mean stress under stretch and the shading area represented the confidence interval, (B) dependence of the variation of σ_x on degrees of freedom for DFN with different microstructure, (C) effect of microstructure (θ and φ) on σ_x. In biaxial test, (D, G, J) the uncertainty of Ψ, ψ_1, and ψ_2 from 110 DFN with the same homogenized microstructure when $\lambda_y = 1.0$, (E, H, K) the variation of Ψ, ψ_1, and ψ_2 on degrees of freedom when $\lambda_x = \lambda_y = 1.15$, and (F, I, L) effect of microstructure on Ψ, ψ_1, and ψ_2 when $\lambda_x = \lambda_y = 1.15$.

4.4.2 FCNN based microscale model design, training, and validation

In this study, we demonstrated the capability and flexibility of using the FCNN to replace DFN in a RVE as a microscale model for uniaxial and biaxial testing. Traditionally, a single MSE is used for a regression type of question. Here, a weighted combination of different popular loss functions was used to reach the best performance based on validation results. Particularly, multiple losses were used for ψ_1 in order to take both relative percentage error and real difference into consideration. Regarding ψ_2, using relative percentage error would put too much emphasis on the accuracy of those ψ_2 that were near zero, as dividing a small true value would lead to a large error. A single mean absolute error was used to evaluate the prediction on ψ_2. Moreover, to ensure the accuracy loss for ψ_1 and ψ_2 have similar magnitude (similar importance of ψ_1 and ψ_2), a factor of 100 was multiplied to the mean absolute error of ψ_2. Special care was taken to impose convexity on the strain energy function in order to satisfy physical constraints and improve numerical stability in the finite element simulations. Using the training and validation data, a grid search was performed to select the weights α_1 and α_2 for enforcing positive definiteness and symmetry. Performance within 500 training epochs was used to examine each pair of parameters for convenience and computational efficiency. We examined the convexity of the strain energy density with respect to two invariants by evaluating whether it was a positive definite symmetric matrix. As the positive definiteness was a major perspective for determining the satisfaction of the convexity condition, we considered the importance of α_1, which controlled the principal minors of the hessian matrix, should be no less than α_2, which was responsible for the symmetry. The results for grid search on strain values in the validation set were shown in Table 4.2. There was a tradeoff between the accuracy and the convexity of the model. In general, as we assigned more weights to convexity (larger α_1 and α_2), the convexity loss was decreased at the cost of an increasing loss of model accuracy. This compensation was most obvious when we started to value convexity (α_1 and α_2 from 0 to 1). Once the α_1 and α_2 were large enough, the benefits of getting more convex were marginal; the extra loss on accuracy was not that much as well. The marginal difference between those training results might also partially come from different weights initialization of the neural network. Moreover, even we would like to impose more weights on enforcing positive definiteness than symmetry, we found a higher α_2 while keeping α_1 the same could also help with making the matrix more positive definite. The set of weights $\alpha_1 = \alpha_2 = 10^4$, was selected since it yielded an overall good validation accuracy while satisfied the convexity

condition. After the selection of α_1 and α_2, a final model was generated using both training and validation set by selecting the best performance with the different number of epochs and different initializations. Finally, a model with accuracy loss = 69.4763, MAPE_ψ_1 = 25.9746, MSE_ψ_1 = 0.8767, MAE_ ψ_1 = 0.4985, MAE_ ψ_2 = 0.3764, positive definiteness loss = 1.43E-16, and symmetry loss = 2.43E-06 was chosen as the final FCNN model to predict ψ_1, and ψ_2 for a given microstructure. The overall accuracy of this model in terms of the average errors for ψ_1 and ψ_2 were also good.

Table 4.2. Validation results obtained from grid search with different α_1 and α_2.

AccuracyLoss = MAPE_ψ1 + MSE_ψ1 + 10*MAE_ψ1 + 100*MAE_ψ2

ConvexityLoss = α1 * PosDefiniteLoss + α2 * SymmetryLoss

TotalLoss = AccuracyLoss + ConvexityLoss

Importance: α1 >= α2		Validation Results						
PosDefinite(α1)	Symmetry(α2)	AccuracyL	MAPE_ψ1	MSE_ψ1	MAE_ψ1	MAE_ψ2	PosDefiniteL	SymmetryL
0	0	49.4247	21.7636	0.2081	0.3313	0.2414	4.394738	3.449158
1	1	57.8122	24.5983	0.6449	0.3869	0.287	0.3068	0.2419
1.00E+02	1	67.9785	31.3028	2.2057	0.672	0.2775	8.39E-04	0.0579
1.00E+02	1.00E+02	68.233	31.4478	2.1432	0.6732	0.2791	5.95E-04	0.0022
1.00E+04	1.00E+02	70.3917	29.8627	1.392	0.6037	0.331	5.457E-10	4.67E-05
1.00E+04	1.00E+04	70.2603	26.0511	0.9152	0.5024	0.3827	1.35E-10	2.32E-05
1.00E+06	1.00E+04	74.66	26.2792	0.9248	0.5056	0.424	4.36E-09	5.09E-06
1.00E+06	1.00E+06	76.7037	28.2308	0.9799	0.5333	0.4216	1.39E-17	6.63E-09

4.4.3 Performance of FCNN model on newly generated testing data

The FCNN model was trained using the training and validation data of 1100 networks to enhance robustness. Testing data was generated separately following 4.3.5. Notably, at least 20 fiber networks were generated for different microstructure, so that the prediction from the FCNN model could be compared with the mean response of these DFNs. We first built a model to predict stress σ_{xx} in a strip-biaxial loading using 60 DFNs with equivalent microstructure ($\theta \approx 0.3\%, \varphi = 0.1\ \mu$m). As stress was directly calculated by solving equilibrium of DFN and it is the main quantity of interest for the FE simulation as well, this output was used as the quantity of interest for validation instead of energy or other energy-derived quantities of the RVE model. In strip biaxial loading, the prediction from the neural network was compared against the average response of different networks. We found that the FCNN predictions (red solid line) laid well

within the confidence interval (blue shading) and were very close to the mean value (blue dashed line) based on the simulations of the equivalent microstructure (

Figure 4.4. A). We next tested the dependence of the error ε as a function of microstructure, and found the prediction error of stress varied with volume fraction θ (

Figure 4.4. B). Namely, a higher error was observed for a network with either a high θ or a low θ. Note that the FCNN thus ignores the variance in the data and predicts the average response of the different DFN microstructures.

To evaluate the performance of FCNN for ψ_1 and ψ_2, the predicted value (solid line) was compared to the means (dashed line) and confidence intervals (shading area) of 100 networks that had the almost same microstructure but was generated by 5 different pairs of seeds and cubic length. Unlike the stress, the recovered values of ψ_1 and ψ_2 had a wider distribution even with the same

microstructure. Networks generated with more seeds in a larger cubic tended to have a higher ψ_1 and a lower ψ_2 (

Figure 4.4. C and E). Take seeds = 450 and $\lambda_x = 1.0$ as an example, the mean ψ_1 was 1.89 with standard deviation equaled to 0.17; the mean ψ_2 was -1.14 with a standard deviation equaled to 0.18. Whereas the overall mean of ψ_1 at $\lambda_x = 1.0$ for these 100 networks was 1.61 with a standard deviation of 0.41 and the mean of ψ_2 was -0.86 with a standard deviation of 0.29. As the FCNN model only took microstructure parameters θ and φ as inputs, for a DFN defined by $\theta \approx 0.3\%$ and $\varphi = 0.1$ μm, the predictions were almost the same (θ slightly varied) under a given stretch no matter how the seeds number varied and thus the solid lines overlapped with each other. In general, the model captured the overall mean of ψ_1 and ψ_2 for these DFNs pretty well under lower stretch. As the deformation increased, the predictions slightly deviated from the overall mean with lower predicted values. This was caused by requiring the convexity of the FCNN model. Once the convexity constrain was removed, the predictions on both ψ_1 and ψ_2 followed the increasing trends pretty well (supplemental Figure C. 1). The relationship between predicted values and network microstructure was evaluated in

Figure 4.4. D and F. The error represented the difference between the predicted response from the FCNN model and the mean response of 20 RVE networks with almost the same microstructure. In general, the model predicted ψ_1 and ψ_2 with small errors for most networks. Higher errors were seen on the edge of the plot, namely, for those networks with extreme value volume fractions and lower fiber diameters. While most of the values for ψ_1 and ψ_2 were small and concentrated after GP and optimization process, some 'outlier' values were noticed. As expected, the model predictions to those edges ψ_1 and ψ_2 were not very ideal (

Figure 4.4.G-J), which was generally the case for regression.

Figure 4.4. Performance of the FCNN against the testing set. (A, B) performance of a neural network for the prediction of stress in strip biaxial loading. The prediction error as a function of microstructure was examined, (C, E) trained FCNN model in predicting ψ_1 and ψ_2 for networks with equivalent microstructure ($\theta \approx 0.3\%$, $\varphi = 0.1$ μm), (D, F) the relationship between prediction error and microstructure, (G-J) the prediction with the large or small true value of ψ_1 and ψ_2 had a higher error.

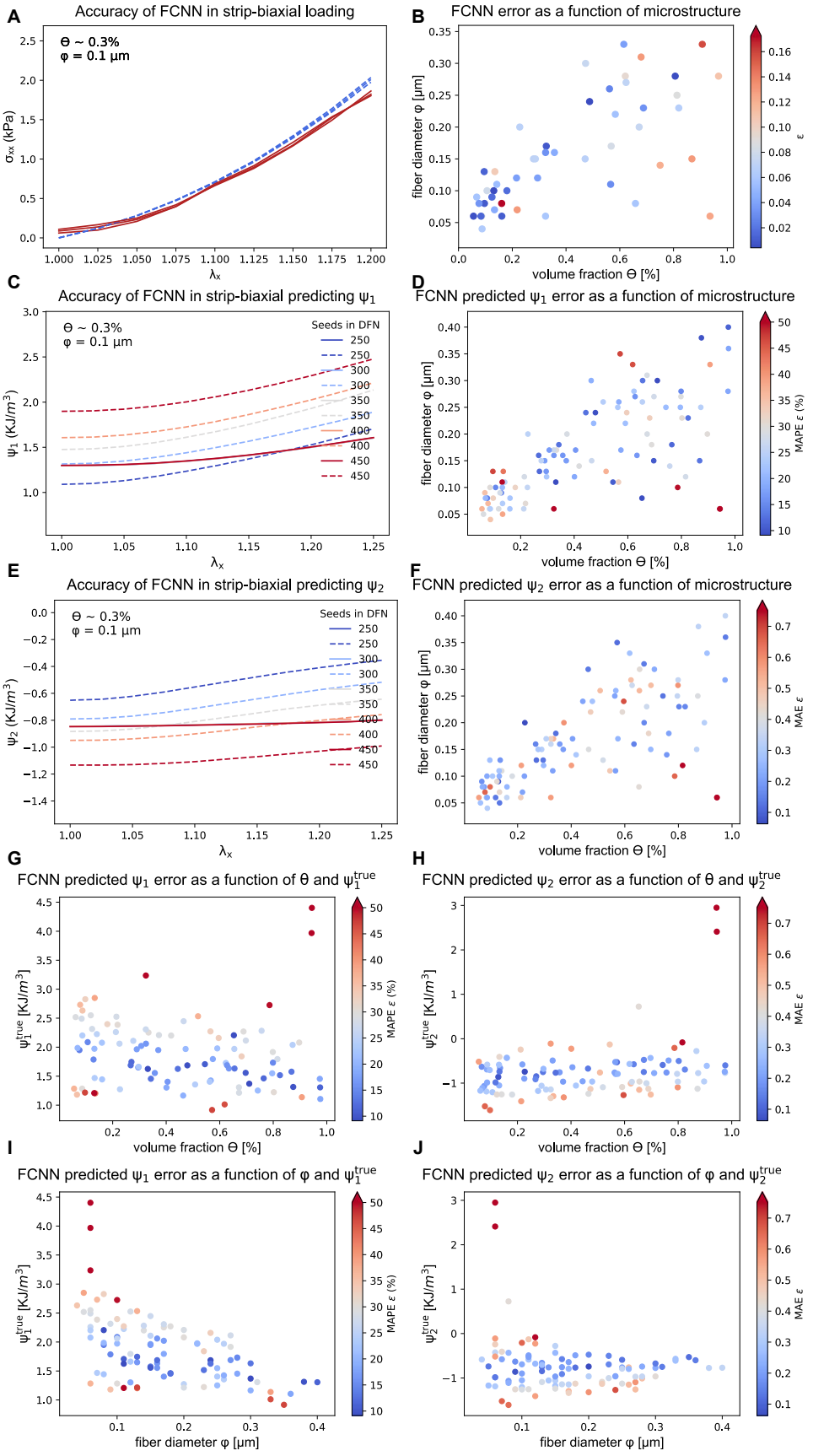
A
Accuracy of FCNN in strip-biaxial loading
Θ ~ 0.3%
φ = 0.1 μm
σxx (kPa)
λx
B
FCNN error as a function of microstructure
fiber diameter φ [μm]
volume fraction Θ [%]
ε
C
Accuracy of FCNN in strip-biaxial predicting ψ1
Θ ~ 0.3%
φ = 0.1 μm
Seeds in DFN
250
250
300
300
350
350
400
400
450
450
ψ1 (KJ/m3)
λx
D
FCNN predicted ψ1 error as a function of microstructure
fiber diameter φ [μm]
volume fraction Θ [%]
MAPE ε (%)
E
Accuracy of FCNN in strip-biaxial predicting ψ2
Θ ~ 0.3%
φ = 0.1 μm
Seeds in DFN
250
250
300
300
350
350
400
400
450
450
ψ2 (KJ/m3)
λx
F
FCNN predicted ψ2 error as a function of microstructure
fiber diameter φ [μm]
volume fraction Θ [%]
MAE ε
G
FCNN predicted ψ1 error as a function of θ and ψ1true
ψ1true [KJ/m3]
volume fraction Θ [%]
MAPE ε (%)
H
FCNN predicted ψ2 error as a function of θ and ψ2true
ψ2true [KJ/m3]
volume fraction Θ [%]
MAE ε
I
FCNN predicted ψ1 error as a function of φ and ψ1true
ψ1true [KJ/m3]
fiber diameter φ [μm]
MAPE ε (%)
J
FCNN predicted ψ2 error as a function of φ and ψ2true
ψ2true [KJ/m3]
fiber diameter φ [μm]
MAE ε

To visualize the convexity of strain energy density function, strain energy density Ψ was computed at a series of E_{11} and E_{22} values (-0.4 to 0.4). The strain energy density function can be calculated through trapezoidal numerical integration of $\Psi = \int \boldsymbol{S}: dE$, where S is the second Piola Kirchhoff stress tensor and dE is the Green Lagrange strain tensor increment. The resulting contours of strain energy function are plotted and examined for a represented microstructure ($\theta \approx 0.3\%$, $\varphi = 0.1$ μm). As shown in Figure 4.5, the strain energy density function was convex.

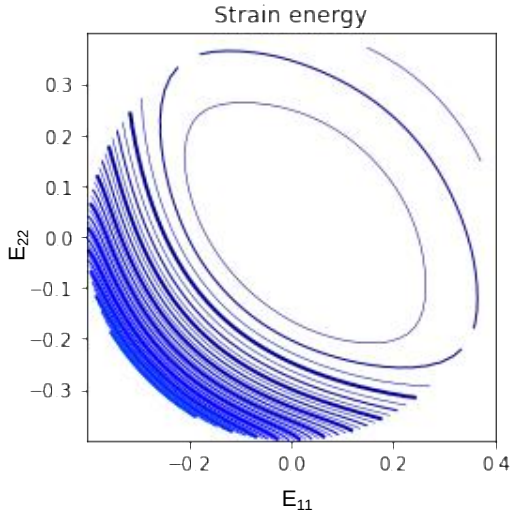

Figure 4.5. Strain energy density function with respect to E_{11} and E_{22} with $E_{12} = 0$ for a network with microstructure ($\theta \approx 0.3\%$, $\varphi = 0.1$ μm)

4.4.4 Finite element simulations

Figure 4.6. shows results from three basic tests done to verify the correct implementation of the FCNN in the UMAT subroutine. We performed a uniaxial test in which symmetry for X, Y, and Z planes was imposed on the corresponding boundaries. A x-displacement was applied on one end of the domain to impose an overall stretch of 1.1 with respect to the initial dimension of the domain. The microstructure parameters used corresponded to $\varphi = 0.161499$ μm and $\theta = 0.45089\%$. The result is a homogeneous stress distribution that is required based on the boundary conditions and aligns with the analytical calculation $\sigma_{11} = 0.3396$ kPa. Secondly, a uniaxial deformation for a higher stretch of 1.2 was applied, but in this case, one of the ends was subject to clamp boundary conditions, i.e. all degrees of freedom were restricted on one end. The x-displacement was applied to the opposite surface to the one that was clamped. All other surfaces were traction-free. The FE simulation converged without any problems. In this case, due to the clamp on one end, the stress

distribution is no longer uniform and boundary effects are visible. The center point of the mesh still behaves correspondingly to uniaxial loading, with a stress that aligns with FCNN predictions outside of the FE implementation. This simulation further suggests that the UMAT was implemented correctly. One last test to verify that the simulation converged under different loading, in particular one that involves shearing, the boundary condition was changed. The left end was kept clamped, but a shear deformation was added on the right boundary. All other surfaces were still traction free. The simulation converged also without a problem, and the resulting stress distribution showed a band of shear and normal stress along the diagonal, which is similar to deformations obtained with simple hyperelastic materials such as neo-Hookean strain energies. Overall these results suggest that the FCNN was implemented correctly in the UMAT, that the second derivatives obtained through back-propagation are also implemented correctly in the UMAT, and that the potential satisfies convexity under the deformations explored, leading to the proper convergence of the simulation.

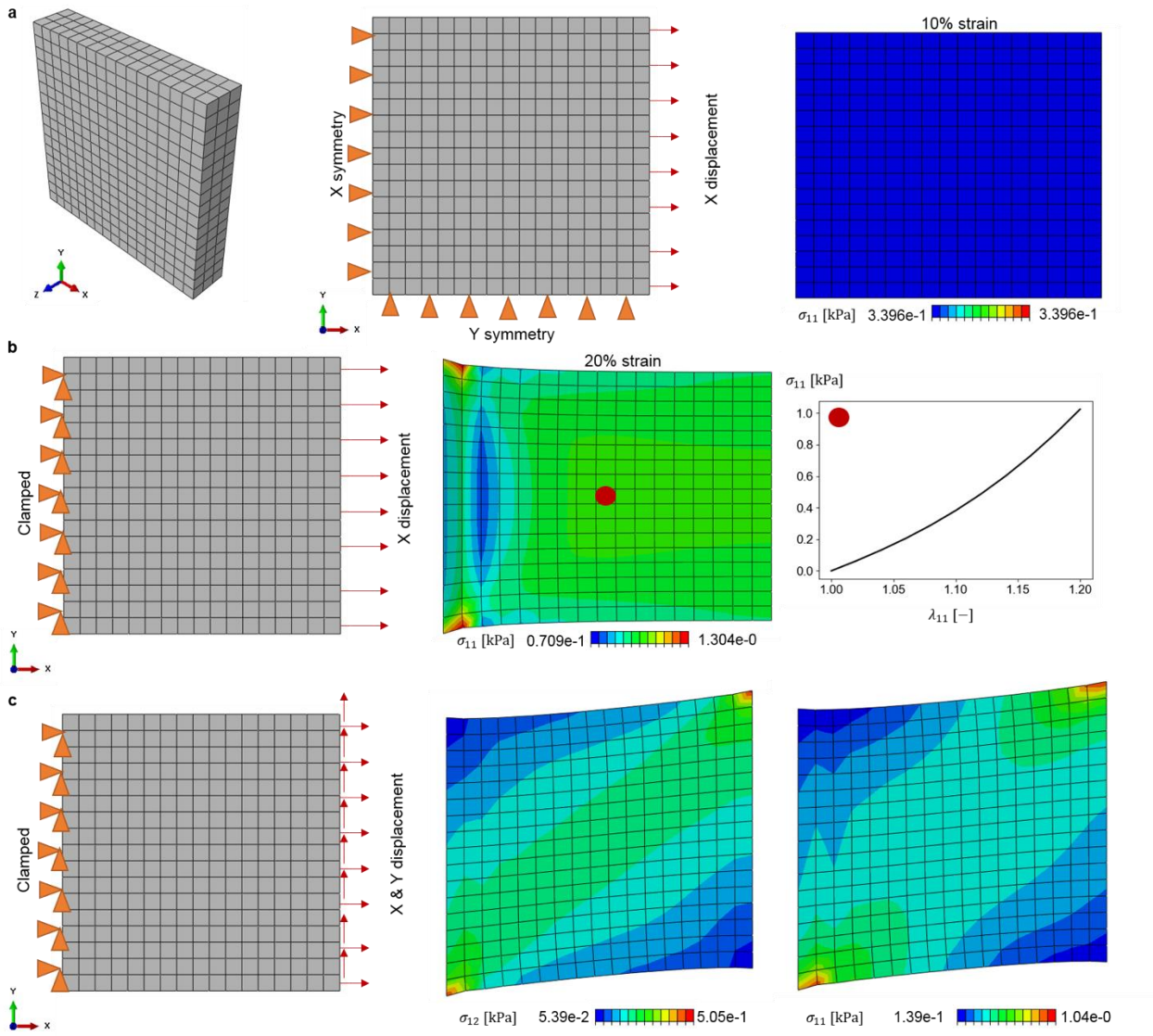

Figure 4.6. Verification of the correct implementation of the FCNN in the UMAT subroutine.

One final example was the modeling of two different biological materials and their interface. This type of domain could represent a wound or a muscle-tendon interface depending on the relative material properties. A circular domain partition was created within the rectangular domain. The UMAT was used for both domains, but with different inputs for the microstructure variables. For the surrounding material we continued to use $\varphi = 0.161499$ μm and $\theta = 0.45089\%$, while for the interior circular domain the microstructure variables were set to $\varphi = 0.2494702$ μm and $\theta = 0.732174\%$. The simulation ran without problems and converged to the results depicted in Figure 4.7, which shows the maximum principal stress over the entire domain. The microstructure of the

inner domain corresponds to slightly stronger material behavior of this inclusion, and thus the strain in the material between the inner circle and the stretched boundary is less than the strain in the outer domain.

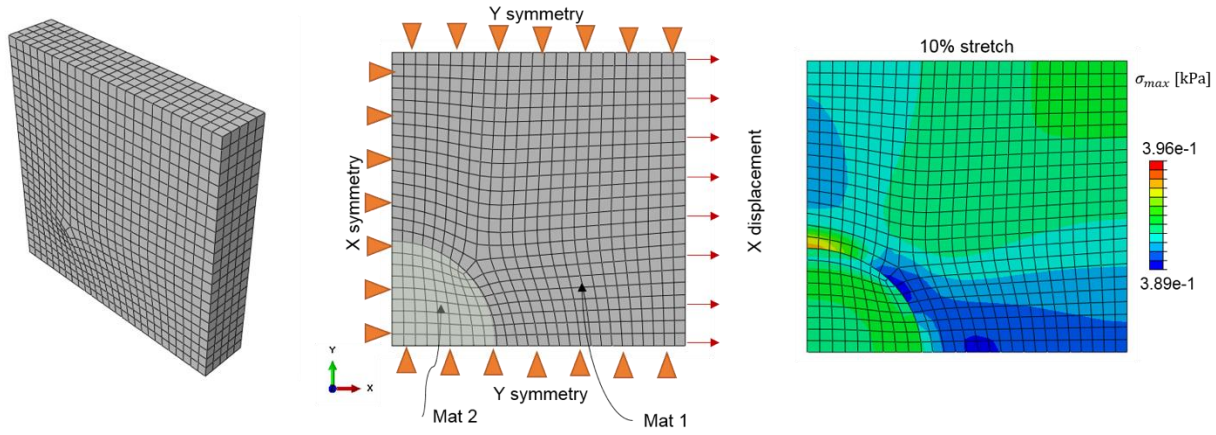

Figure 4.7. FE simulation of an interface with different microstructure for inner and outer domains.

4.5 Discussion

In this study, we proposed to use a FCNN based microscale model for the energy (and stress) prediction in a fiber network. A simple neural network was used as a basis function to approximate a complex constitutive relation between the fibrin network microstructures and the mechanical responses under certain stretch. While the RVE model took approximately 1min to solve equilibrium for a DFN network, the prediction from the FCNN was less than 1msec, highlighting the significant speed-up from using machine learning tools to interpolate physics-based models. Significantly, the FCNN model had a simple structure with a small number of parameters and was physically meaningful and numerically stable. Only two constitutive parameters (θ and φ) were needed for predicting a mechanical response. These constitutive parameters were physically relevant and could be analyzed from imaging data when available. The model reached considerably good accuracy in predicting ψ_1 and ψ_2 for most of the networks after several hours of training, i.e. similar to the results getting from solving equilibrium of RVE while taking more time and effort. The error was expected due to the uncertainty in the energy for a given microstructure. We remark once again that the error values are affected by the fact that for a single microstructure the random nature of the DFN results in predictions with the variance that is not captured by our deterministic FCNN. Upon inspection of the validation plots, it is clear that the

FCNN captures the mean response well. Future work will deal with Bayesian neural networks that can capture the variance in the response instead of deterministic predictions (Mullachery et al., 2018; Neal, 1996). For those samples with relatively larger error, most networks had extreme values of microstructure parameters. Moreover, their true ψ_1 and ψ_2 values were also in the outlier zone. These unusual and inconsistent values could be caused by the unstable/diverging/non-unique solutions from fitting GP and optimization. Other refinements of the DFN model can be considered. In this effort, we opted for a simple mechanical equilibrium problem in which fibers contribute only due to stretching but not bending. To make the network more stable, bending resistance could be considered (Licup et al., 2015; Zhang, 2013). Different constitutive models for individual fibers can also be incorporated (Aghvami et al., 2016; Hadi et al., 2012; Raghupathy & Barocas, 2009; Sander et al., 2009). For the FCNN based model, besides a Bayesian approach that could handle the variance in the response function, networks with a more advanced structure or activation functions could also be considered in the future to improve the training and testing performance.

Due to the substantial reduction in computational time and reasonable accuracy in energy prediction, we next embedded our FCNN as a microscale model in FE simulations and implemented on both basic cases and a composite network. The finite element implementation showed that the FCNN was indeed stable and computed derivatives accurately as needed for convergence of the Newton iterations in the commercial FE solver package.

Our work demonstrated that neural networks can be trained by micromechanical simulations, which capture ECM network behaviors and their relation to microstructural mechanisms. The future work includes using the FCNN to predict rate-dependent constitutive relations, the behaviors of fibrin gels *in vitro*, and for inverse estimation of microstructure parameters of a network with *in vitro* gel data.

5. CONCLUSION AND FUTURE DIRECTIONS

5.1 Conclusions

The goal of this dissertation was to investigate the role of ECM during early musculoskeletal development, and thus inform new tissue engineering approaches that facilitate tissue assembly. I made advances towards answering the central hypothesis directing the Calve Lab through the following contributions:

(1) Map the temporal and spatial distribution of key ECM (HA) during myogenesis and identify targets that regulate skeletal muscle differentiation and organization. To map the distribution of HA and its receptors (CD44 and RHAMM) with respect to the developing musculoskeletal system, we performed immunohistochemical analysis on Pax3-Cre/ZsGreen1+ forelimb during primary myogenesis (E10.5 – E12.5). To quantify the expression of these proteins with respect to time during development, gene expression was tested via qPCR. The role of HA and its receptors on the migration and proliferation of myoblasts and its surrounding connective tissue cell was investigated by adding 4-methylumbelliferone (a HA polymerization inhibitor), using antibodies against CD44 and RHAMM to block their activity, and performing depletion of CD44 and RHAMM by shRNA. We concluded that HA, through interactions with CD44 and RHAMM, promotes myogenic progenitor migration and proliferation. In this part of work, we integrated different established techniques into a robust method to assess the effect of perturbations on ECM-cell interactions, elucidate how cell behaviors are regulated by ECM composition, and identify specific components that regulate muscle assembly during musculoskeletal development.

(2) Establish a 3D map of ECM architecture, identify the composition of the ECM template and its potential instructive role during muscle, tendon, and MTJ formation. In order to resolve the 3D ECM architecture during development, we first created a novel decellularization method that maintains the matrix geometry of developing forelimb to image specific ECM deep within developing musculoskeletal tissues using confocal microscopy. With this imaging technique, we observed an abundance of ECM fibers was deposited before the integration of muscle and tendon. By comparing the Pax3-Cre/Cre and wild type forelimbs, the structure and alignment of ECM, tendon, and myotubes were visualized as a function of time and genotype. We also

identified proteins within the ECM with respect to the developing muscle, tendon, and their interface. In this part of the work, we provided evidence that an ECM-based template, deposited before the formation of muscle, tendon, and MTJ, participates in directing the proper combinations between muscle and tendon, and delineates space for muscle formation, indicating ECM is a macromolecular network with not only structural but also instructive functions.

(3) Create a multiscale computational model of growth and remodeling. In order to build a model that incorporates microscale events rather than is purely phenomenological, we developed a novel microstructure-sensitive, yet flexible and numerically efficient multifield model. To describe the microscale, the integration point subroutines of the FE implementation was using a FCNN model that was trained with RVE simulations of DFN. To ensure the model is physically meaningful with unambiguous mechanical characteristics and improve numerical stability, convexity was considered during the model training by a specifically designed loss function. In this part of the work. we demonstrated that neural networks can be trained by micromechanical simulations, which capture microscale ECM network changes accurately and efficiently and embedded in finite element simulations for the emergent mechanical behaviors at the tissue level.

We believe these results will provide critical insight into the mechanisms that orchestrate musculoskeletal assembly and establish guidelines for regenerative therapies.

5.2 Future Work

Current design of engineered scaffolds rarely has the architecture found *in vivo* and only one or two matrices can be reliably included *in vitro*. In contrast, the ECM consists of complex interpenetrating networks that are constructed of many different components. To better design a scaffold that meets the complex structural and mechanical requirements of tissue, an in-depth understanding of the biological and mechanical characterization of native muscle, tendon, and the myotendinous junction is required. Based on what we have found, and to further test our central hypothesis, the proposed future studies from this thesis are listed here:

(1) Enable 4D imaging of cells and ECM components in the developing mouse forelimb. In order to capture the local changes in the complex interpenetrating ECM network *in vivo* and investigate how cells respond to perturbations in the native 3D ECM environment of the

developing forelimb as a function of time, a robust live culturing and imaging system needs to be developed. Vibratome sectioned E11.5-E12.5 forelimb buds could be obtained from embryos. After staining for ECM of interest, specimen can be imaged via time-lapse confocal microscopy for 8-24 hours (Massarwa & Niswander, 2013). The distribution, organization, and the interactions of td-Tomato (red) labeled Pax3+ muscle progenitors, GFP+ Scx+ tendon progenitors, and particular ECM protein could be visualized. Local cell-autonomous displacements from bulk morphogenetic processes could be analyzed with particle image velocimetry computation tool and ImageJ/MATLAB (Prochazka et al., 2015; Zamir et al., 2006). The orientation and elongation of ECM fibers could be quantified with fast iterative digital volume correlation algorithm (Acuna et al., 2019; Bar-Kochba et al., 2015). Thus, the potential instructive role of ECM during early limb development could be validated.

(2) Identify the role of connective tissue and ECM with genetic manipulation of fibroblasts in muscle and tendon. Previous studies imply connective tissue, via Lmx1b (Li et al., 2010), Tcf4 (Mathew et al., 2011), Tbx3 (Colasanto et al., 2016), Tbx4, and Tbx5 (Hasson et al., 2010) function, influences the pattern of muscles and tendons in the murine limb. Take Tcf4 as an example, Proteomic analyses with liquid chromatography-tandem mass spectrometry could be done to find the potential Tcf4-dependent ECM template candidates. Developing forelimbs from Pax3 wild type, Pax3 Cre/Cre, Tcf4 wild type, limb specific TCF4 knockout embryos could be collected. The overall complex musculoskeletal architecture of the E12.5-E14.5 forelimbs and the distribution of these ECM molecules could be analyzed via immunostaining after clearing and decellularization. How the myoblasts and tendon cells migrate and deposit along the ECM fibers could be visualized *in situ*. Moreover, the mechanical properties of ECM fibers in forelimbs of different mouse models could be tested to provide insight into ECM mechanics *in vivo*.

(3) Include cells in multiscale computational model of growth and remodeling. Fibrin and collagen gels seeded with fibroblasts, and/or myoblasts and tenocytes could be generated. After subjected to an initial deformation, the mechanical properties of the gels and their stress-free configuration will be traced over time (days to weeks). Meanwhile, the microstructure of the gels could be imaged under confocal to evaluate ECM remolding. Then, the multiscale computational model incorporating a continuum field for cells could be tested for predicting the mechanical response compared to the experiment results. Furthermore, gels with more

complex structure or collagen-fibrin hybrid gels could also be made to make the model more robust. At last, native ECM in decellularized forelimb could be used to investigate how cell activity is coupled with ECM and tissue-scale changes.

These work will therefore guide the future design of scaffolds with a better understanding of growth, remodeling, and development *in vivo*.

APPENDIX A. SUPPLEMENT TO CHAPTER 2

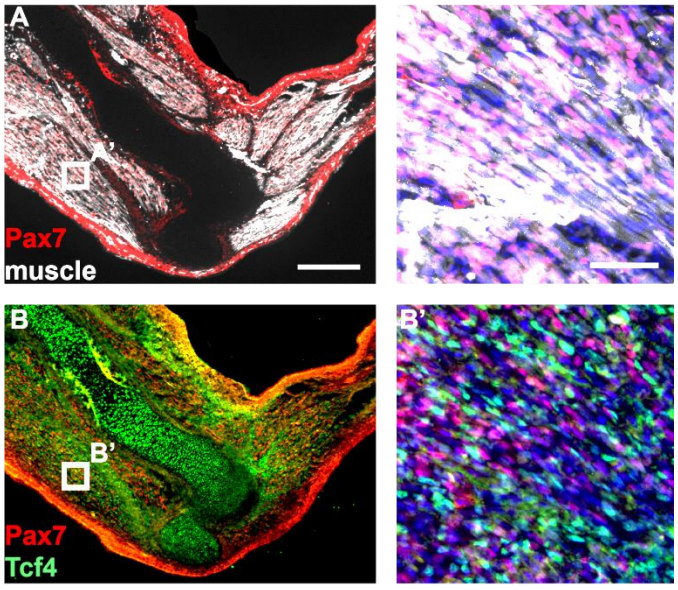

Figure A. 1. The characterization of GFP+ and GFP- cells. To confirm the GFP+ cells in our model system are part of the myogenic lineage, E13.5 forelimb cryosections were stained for Pax7 and Tcf4. Tcf4 is a transcription factor that is highly expressed in connective tissue cells between and surrounding the myogenic cells during development (Colasanto et al., 2016; Mathew et al., 2011; Murphy et al., 2011). Pax7, a paired box transcription factor family member, identifies myogenic stem cells (Murphy et al., 2011). Consistent with previous studies, Pax7 co-localized with the nuclei of GFP+ skeletal muscle cells, and Tcf4-labeled GFP- cells were found in between the Pax7+ muscle progenitors. (A-B) Cryosections of Pax3-Cre:ROSA-ZsGreen E13.5 forelimbs were fluorescently labeled for Pax7 (red), Tcf4 (green) and GFP+ muscle (white). 5×, bar = 300 μm. (A'-B') Higher resolution images of A and B labeled for Dapi (blue), Pax7 (red), Tcf4 (green) and GFP+ muscle (white). 20×, bar = 50 μm.

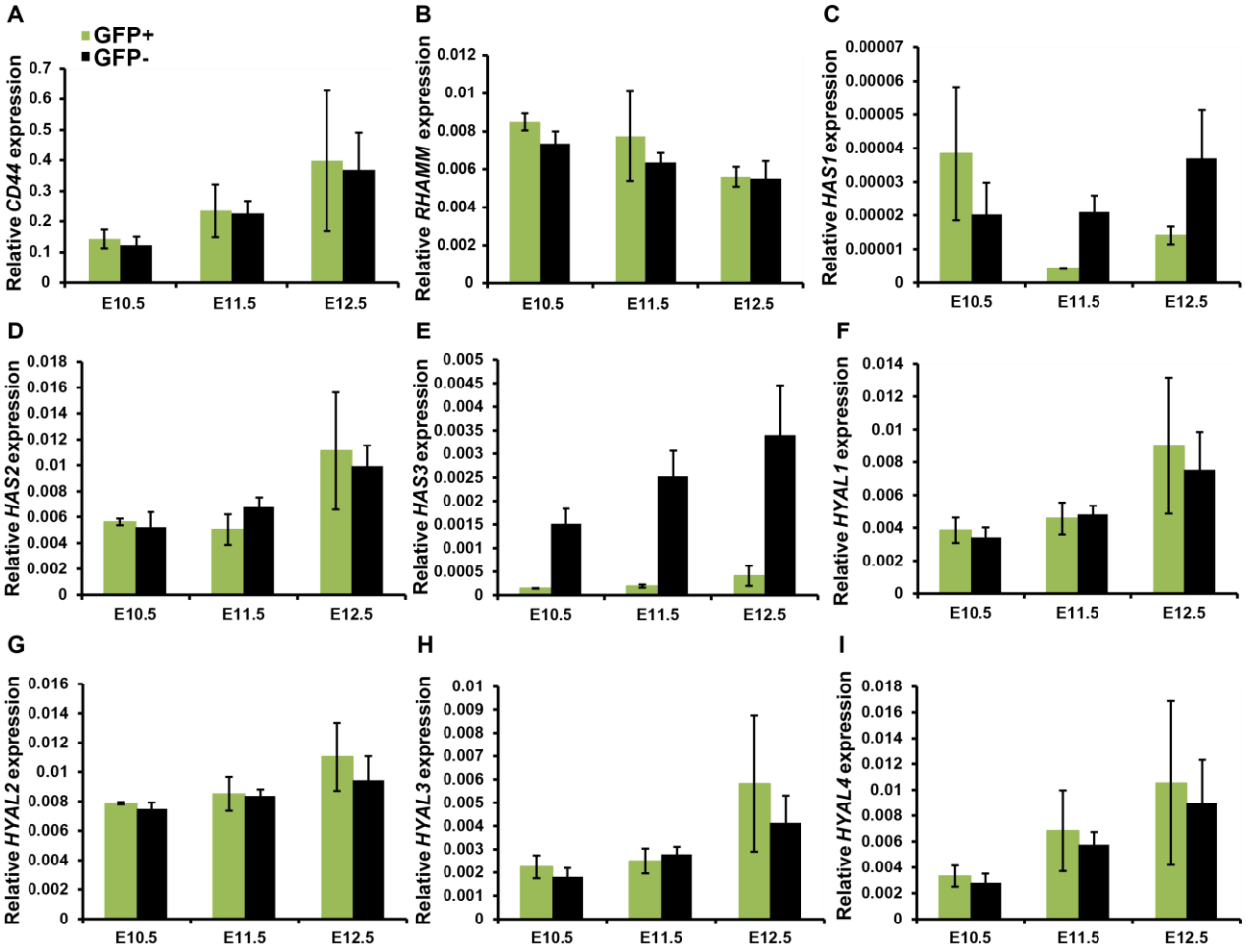

Figure A. 2. Relative expression of *CD44*, *RHAMM*, *HAS1-3* and *Hyal1-4*. Geometric means and standard deviation are shown (*p<0.05, Error bars= S.D.; n≥3 biological replicates)

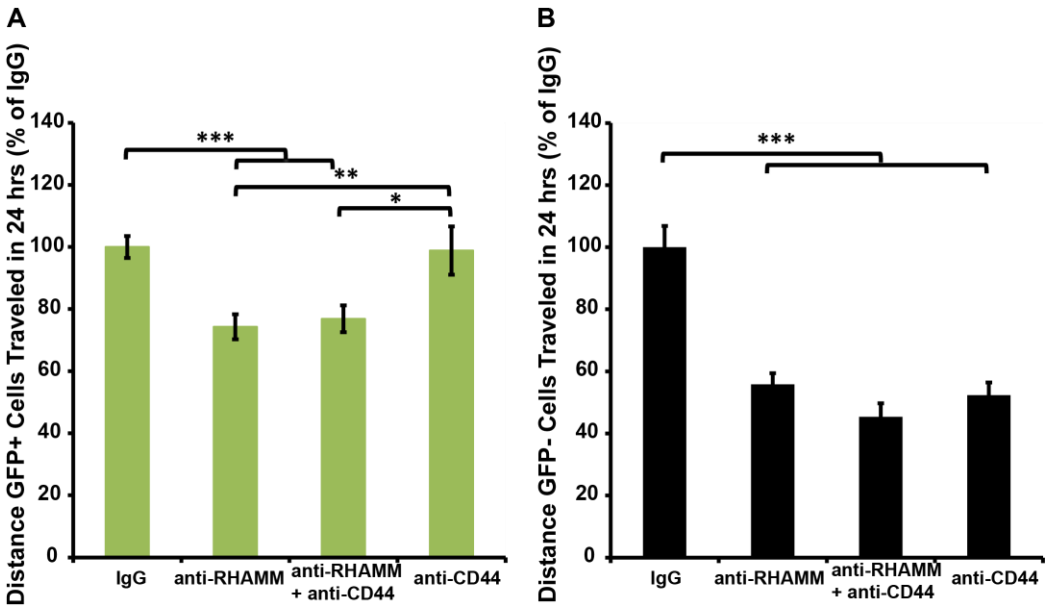

Figure A. 3. Anti-RHAMM and anti-CD44 affected unsorted cells the same as isolated cells (Fig. 4). Anti-RHAMM significantly decreased the total distance GFP+ cells migrated over 24 hrs, whereas both antibodies inhibited GFP- cell migration. (Two-way ANOVA showed that antibody treatment and cell type had a strong effect on cell migration $p<0.0001$. Tukey's post hoc test was used for comparisons between group, where ***$p<0.005$, **$p<0.01$, *$p<0.05$; error bars = S.E; $n \geq 45$ cells/condition across the 3 biological replicates.)

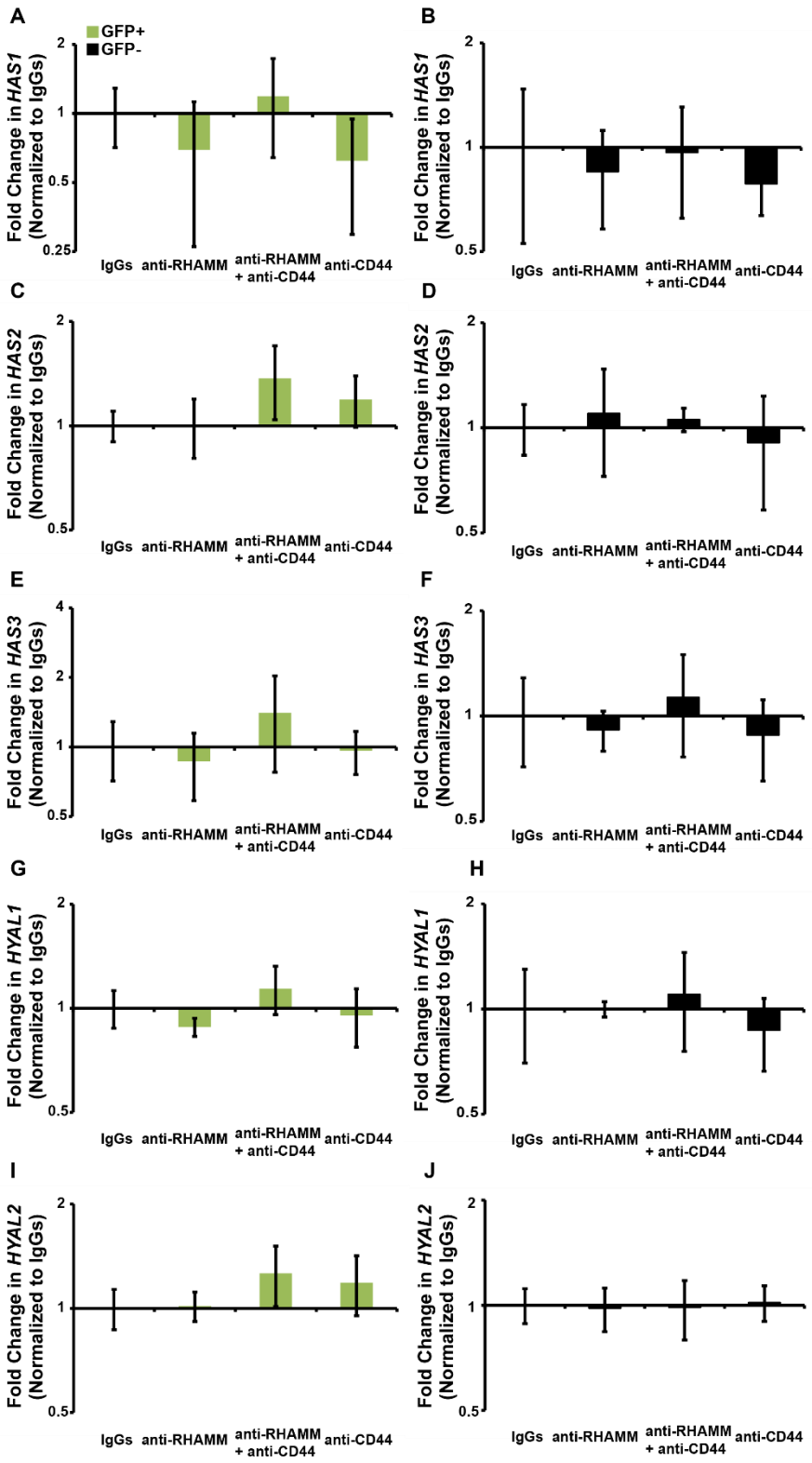

Figure A. 4. Differential expression of HA related genes in GFP+ (green) and GFP- cells (black) after antibody treatment. Geometric means and standard deviation are shown in $\log_2$ scale (Error bars= S.D.; n≥3).

APPENDIX B. SUPPLEMENT TO CHAPTER 3

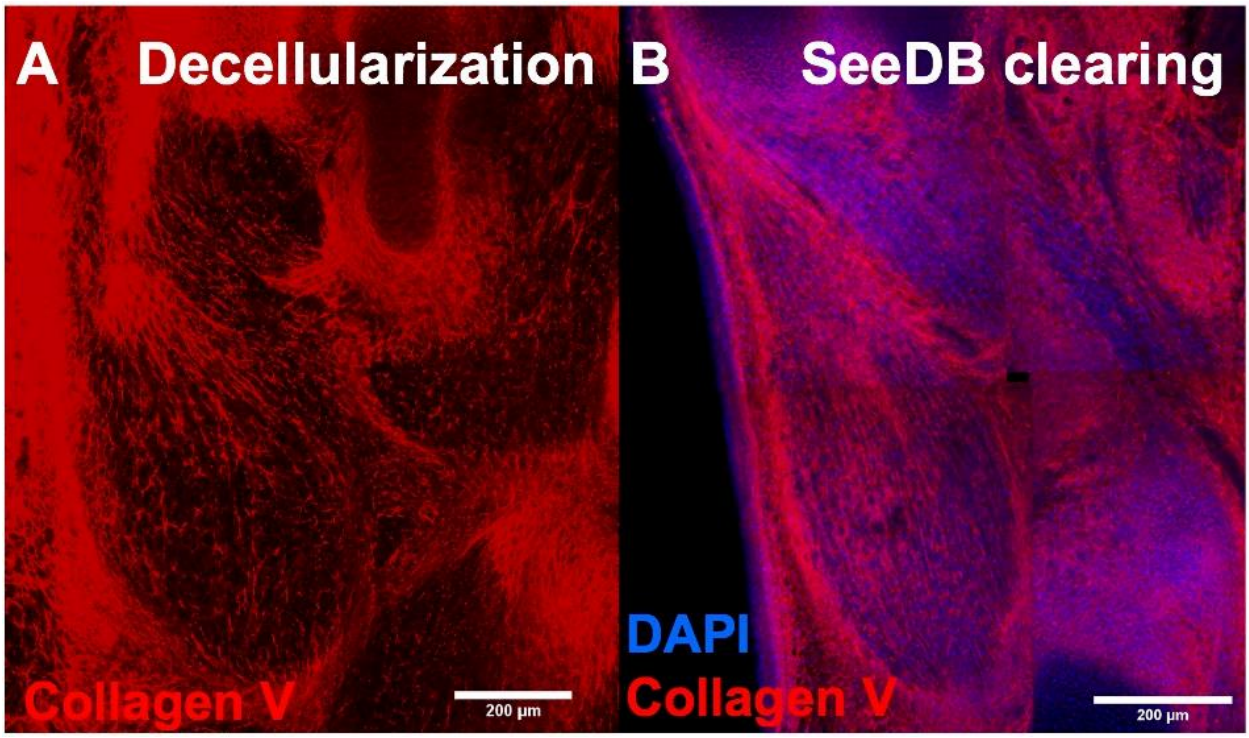

Figure B. 1. E13.5 WT Triceps region after decellularization (A) and SeeDB clearing (B). Red = type V collagen; Blue = DAPI. Single z plane image with the magnification 10x (A) and 25x (B). Scale bar = 200 µm. The bottom side of the image is proximal, and the top is distal.

APPENDIX C. SUPPLEMENT TO CHAPTER 4

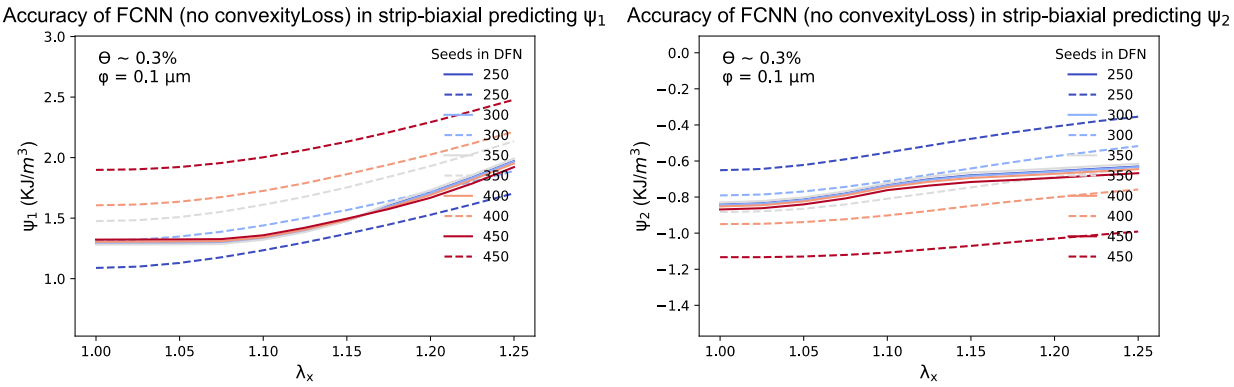

Figure C. 1. FCNN predictions on ψ_1 and ψ_2 without imposing convexity requirement on the model.

REFERENCES

Abadi, M., Agarwal, A., Barham, P., Brevdo, E., Chen, Z., Citro, C., Corrado, G. S., Davis, A., Dean, J., Devin, M., Ghemawat, S., Goodfellow, I., Harp, A., Irving, G., Isard, M., Jia, Y., Jozefowicz, R., Kaiser, L., Kudlur, M., … Zheng, X. (2016). *TensorFlow: Large-Scale Machine Learning on Heterogeneous Distributed Systems*. http://arxiv.org/abs/1603.04467

Acharya, P. S., Majumdar, S., Jacob, M., Hayden, J., Mrass, P., Weninger, W., Assoian, R. K., & Puré, E. (2008). Fibroblast migration is mediated by CD44-dependent TGF beta activation. *Journal of Cell Science*, *121*(Pt 9), 1393–1402. https://doi.org/10.1242/jcs.021683

Acuna, A., Sofronici, S. H., Goergen, C. J., & Calve, S. (2019). In Situ Measurement of Native Extracellular Matrix Strain. *Experimental Mechanics*, *59*(9), 1307–1321. https://doi.org/10.1007/s11340-019-00499-y

Acuna, Andrea. (2020). *Characterizing the mechanical behavior of extracellular matrix networks in situ*. https://doi.org/10.25394/PGS.12736370.V1

Acuna, Andrea, Drakopoulos, M. A., Leng, Y., Goergen, C. J., & Calve, S. (2018). Three-dimensional visualization of extracellular matrix networks during murine development. *Developmental Biology*, *435*(2), 122–129. https://doi.org/10.1016/j.ydbio.2017.12.022

Adamia, S., Maxwell, C. A., & Pilarski, L. M. (2005). Hyaluronan and hyaluronan synthases: potential therapeutic targets in cancer. *Current Drug Targets. Cardiovascular & Haematological Disorders*, *5*(1), 3–14. http://www.ncbi.nlm.nih.gov/pubmed/15720220

Aghvami, M., Billiar, K. L., & Sander, E. A. (2016). Fiber Network Models Predict Enhanced Cell Mechanosensing on Fibrous Gels. *Journal of Biomechanical Engineering*, *138*(10), 1010061. https://doi.org/10.1115/1.4034490

Agoram, B., & Barocas, V. H. (2001). Coupled macroscopic and microscopic scale modeling of fibrillar tissues and tissue equivalents. *Journal of Biomechanical Engineering*, *123*(4), 362–369. https://doi.org/10.1115/1.1385843

Alber, M., Buganza Tepole, A., Cannon, W. R., De, S., Dura-Bernal, S., Garikipati, K., Karniadakis, G., Lytton, W. W., Perdikaris, P., Petzold, L., & Kuhl, E. (2019). Integrating machine learning and multiscale modeling—perspectives, challenges, and opportunities in the biological, biomedical, and behavioral sciences. *Npj Digital Medicine*, *2*(1), 1–11. https://doi.org/10.1038/s41746-019-0193-y

Alberts, B., Johnson, A., Lewis, J., Raff, M., Roberts, K., & Walter, P. (2002). *The Extracellular Matrix of Animals*. https://www.ncbi.nlm.nih.gov/books/NBK26810/

Apte, S. S. (2016). ADAMTS Proteases: Mediators of Physiological and Pathogenic Extracellular Proteolysis. In *Encyclopedia of Cell Biology* (Vol. 1, pp. 630–638). Elsevier Inc. https://doi.org/10.1016/B978-0-12-394447-4.10074-4

Aruffo, A., Stamenkovic, I., Melnick, M., Underhill, C. B., & Seed, B. (1990). CD44 is the principal cell surface receptor for hyaluronate. *Cell*, *61*(7), 1303–1313. http://www.ncbi.nlm.nih.gov/pubmed/1694723

Asahara, H., Inui, M., & Lotz, M. K. (2017). Tendons and Ligaments: Connecting Developmental Biology to Musculoskeletal Disease Pathogenesis. *Journal of Bone and Mineral Research*, *32*(9), 1773–1782. https://doi.org/10.1002/jbmr.3199

Assmann, V., Jenkinson, D., Marshall, J. F., & Hart, I. R. (1999). The intracellular hyaluronan receptor RHAMM/IHABP interacts with microtubules and actin filaments. *Journal of Cell Science*, 3943–3954. http://www.ncbi.nlm.nih.gov/pubmed/10547355

Azeloglu, E. U., Albro, M. B., Thimmappa, V. A., Ateshian, G. A., & Costa, K. D. (2008). Heterogeneous transmural proteoglycan distribution provides a mechanism for regulating residual stresses in the aorta. *American Journal of Physiology - Heart and Circulatory Physiology*, *294*(3). https://doi.org/10.1152/ajpheart.01027.2007

Bajanca, F., Luz, M., Raymond, K., Martins, G. G., Sonnenberg, A., Tajbakhsh, S., Buckingham, M., & Thorsteinsdóttir, S. (2006). Integrin α6β1-laminin interactions regulate early myotome formation in the mouse embryo. *Development*, *133*(9), 1635–1644. https://doi.org/10.1242/dev.02336

Baldino, L., Cardea, S., Maffulli, N., & Reverchon, E. (2016). Regeneration techniques for bone-To-Tendon and muscle-To-Tendon interfaces reconstruction. *British Medical Bulletin*, *117*(1), 25–37. https://doi.org/10.1093/bmb/ldv056

Banos, C. C., Thomas, A. H., & Kuo, C. K. (2008). Collagen fibrillogenesis in tendon development: Current models and regulation of fibril assembly. In *Birth Defects Research Part C - Embryo Today: Reviews* (Vol. 84, Issue 3, pp. 228–244). John Wiley & Sons, Ltd. https://doi.org/10.1002/bdrc.20130

Bar-Kochba, E., Toyjanova, J., Andrews, E., Kim, K. S., & Franck, C. (2015). A Fast Iterative Digital Volume Correlation Algorithm for Large Deformations. *Experimental Mechanics*, *55*(1), 261–274. https://doi.org/10.1007/s11340-014-9874-2

Barco, R., Sánchez, P., Morrey, M. E., Morrey, B. F., & Sánchez-Sotelo, J. (2017). *The distal triceps tendon insertional anatomy-implications for surgery*. https://doi.org/10.1016/j.jses.2017.05.002

Bartels, H. (1987). Intramembrane aspects of myotendinous and myomuscular junctions: A freeze-fracture study of the gill sac-muscle of the atlantic hagfish,Myxine glutinosa. *The Anatomical Record*, *218*(3), 249–255. https://doi.org/10.1002/ar.1092180305

Bastow, E. R., Lamb, K. J., Lewthwaite, J. C., Osborne, A. C., Kavanagh, E., Wheeler-Jones, C. P. D., & Pitsillides, A. A. (2005). Selective activation of the MEK-ERK pathway is regulated by mechanical stimuli in forming joints and promotes pericellular matrix formation. *Journal of Biological Chemistry*, *280*(12), 11749–11758. https://doi.org/10.1074/jbc.M414495200

Bayrak, E., & Yilgor Huri, P. (2018). Engineering Musculoskeletal Tissue Interfaces. *Frontiers in Materials*, *5*, 24. https://doi.org/10.3389/fmats.2018.00024

Beldjilali-Labro, M., Garcia, A. G., Farhat, F., Bedoui, F., Grosset, J. F., Dufresne, M., & Legallais, C. (2018). Biomaterials in tendon and skeletal muscle tissue engineering: Current trends and challenges. In *Materials* (Vol. 11, Issue 7). MDPI AG. https://doi.org/10.3390/ma11071116

Bentzinger, C. F., Wang, Y. X., & Rudnicki, M. A. (2012). Building muscle: molecular regulation of myogenesis. In *Cold Spring Harbor perspectives in biology* (Vol. 4, Issue 2). Cold Spring Harbor Laboratory Press. https://doi.org/10.1101/cshperspect.a008342

Bernhard Schölkopf, Koji Tsuda, J.-P. V. (2019). Kernel Methods in Computational Biology. In *Kernel Methods in Computational Biology*. The MIT Press. https://doi.org/10.7551/mitpress/4057.001.0001

Besse, L., Sheeba, C. J., Holt, M., Labuhn, M., Wilde, S., Feneck, E., Bell, D., Kucharska, A., & Logan, M. P. O. (2020). Individual Limb Muscle Bundles Are Formed through Progressive Steps Orchestrated by Adjacent Connective Tissue Cells during Primary Myogenesis. *Cell Reports*, *30*(10), 3552-3565.e6. https://doi.org/10.1016/j.celrep.2020.02.037

Bhagawati, M., & Kumar, S. (2014). Biofunctionalization of Hydrogels for Engineering the Cellular Microenvironment. In *Micro-and Nanoengineering of the Cell Surface* (pp. 315–348). Elsevier Inc. https://doi.org/10.1016/B978-1-4557-3146-6.00014-3

Bhattacharjee, S., & Matouš, K. (2016). A nonlinear manifold-based reduced order model for multiscale analysis of heterogeneous hyperelastic materials. *Journal of Computational Physics*, *313*, 635–653. https://doi.org/10.1016/j.jcp.2016.01.040

Bi, Y., Ehirchiou, D., Kilts, T. M., Inkson, C. A., Embree, M. C., Sonoyama, W., Li, L., Leet, A. I., Seo, B. M., Zhang, L., Shi, S., & Young, M. F. (2007). Identification of tendon stem/progenitor cells and the role of the extracellular matrix in their niche. *Nature Medicine*, *13*(10), 1219–1227. https://doi.org/10.1038/nm1630

Bian, L. (2014). The Role of Mechanical Cues in Regulating Cellular Activities and Guiding Tissue Development. In *Bio-inspired Materials for Biomedical Engineering* (Vol. 9781118369364, pp. 45–58). John Wiley & Sons, Inc. https://doi.org/10.1002/9781118843499.ch3

Biewener, A. A. (1998). Muscle-tendon stresses and elastic energy storage during locomotion in the horse. *Comparative Biochemistry and Physiology - B Biochemistry and Molecular Biology*, *120*(1), 73–87. https://doi.org/10.1016/S0305-0491(98)00024-8

Biressi, S., Molinaro, M., & Cossu, G. (2007). Cellular heterogeneity during vertebrate skeletal muscle development. *Developmental Biology*, *308*(2), 281–293. https://doi.org/10.1016/j.ydbio.2007.06.006

Birk, D. E. (2001). Type V collagen: Heterotypic type I/V collagen interactions in the regulation of fibril assembly. In *Micron* (Vol. 32, Issue 3, pp. 223–237). Micron. https://doi.org/10.1016/S0968-4328(00)00043-3

Birk, D. E., & Trelstad, R. L. (1986). Extracellular compartments in tendon morphogenesis: Collagen fibril, bundle, and macroaggregate formation. *Journal of Cell Biology*, *103*(1), 231–240. https://doi.org/10.1083/jcb.103.1.231

Birk, D.E., Fitch, J. M., Babiarz, J. P., Doane, K. J., & Linsenmayer, T. F. (1990). Collagen fibrillogenesis in vitro: interaction of types I and V collagen regulates fibril diameter. *Journal of Cell Science*, *95*(4).

Birk, David E., Zycband, E. I., Woodruff, S., Winkelmann, D. A., & Trelstad, R. L. (1997). Collagen fibrillogenesis in situ: Fibril segments become long fibrils as the developing tendon matures. *Developmental Dynamics*, *208*(3), 291–298. https://doi.org/10.1002/(SICI)1097-0177(199703)208:3<291::AID-AJA1>3.0.CO;2-D

Black, L. D., Allen, P. G., Morris, S. M., Stone, P. J., & Suki, B. (2008). Mechanical and failure properties of extracellular matrix sheets as a function of structural protein composition. *Biophysical Journal*, *94*(5), 1916–1929. https://doi.org/10.1529/biophysj.107.107144

Blitz, E., Viukov, S., Sharir, A., Shwartz, Y., Galloway, J. L., Pryce, B. A., Johnson, R. L., Tabin, C. J., Schweitzer, R., & Zelzer, E. (2009). Bone Ridge Patterning during Musculoskeletal Assembly Is Mediated through SCX Regulation of Bmp4 at the Tendon-Skeleton Junction. *Developmental Cell*, *17*(6), 861–873. https://doi.org/10.1016/j.devcel.2009.10.010

Bogart, B. I., & Ort, V. H. (2007). *Elsevier's integrated anatomy and embryology*. Mosby/Elsevier.

Bonnin, M.-A., Laclef, C., Blaise, R., Eloy-Trinquet, S., Relaix, F., Maire, P., & Duprez, D. (2005). Six1 is not involved in limb tendon development, but is expressed in limb connective tissue under Shh regulation. *Mechanisms of Development*, *122*(4), 573–585. https://doi.org/10.1016/J.MOD.2004.11.005

Boregowda, R., Paul, E., White, J., & Ritty, T. M. (2008). Bone and soft connective tissue alterations result from loss of fibrillin-2 expression. *Matrix Biology*, *27*(8), 661–666. https://doi.org/10.1016/j.matbio.2008.09.579

Borschel, G. H., Dow, D. E., Dennis, R. G., & Brown, D. L. (2006). Tissue-Engineered Axially Vascularized Contractile Skeletal Muscle. *Plastic and Reconstructive Surgery*, *117*(7), 2235–2242. https://doi.org/10.1097/01.prs.0000224295.54073.49

Borselli, C., Cezar, C. A., Shvartsman, D., Vandenburgh, H. H., & Mooney, D. J. (2011). The role of multifunctional delivery scaffold in the ability of cultured myoblasts to promote muscle regeneration. *Biomaterials*, *32*(34), 8905–8914. https://doi.org/10.1016/j.biomaterials.2011.08.019

Bosman, F. T., & Stamenkovic, I. (2003). Functional structure and composition of the extracellular matrix. *The Journal of Pathology*, *200*(4), 423–428. https://doi.org/10.1002/path.1437

Boudjadi, S., Chatterjee, B., Sun, W., Vemu, P., & Barr, F. G. (2018). The expression and function of PAX3 in development and disease. In *Gene* (Vol. 666, pp. 145–157). Elsevier B.V. https://doi.org/10.1016/j.gene.2018.04.087

Bourguignon, L. Y. W., Gilad, E., & Peyrollier, K. (2007). Heregulin-mediated ErbB2-ERK signaling activates hyaluronan synthases leading to CD44-dependent ovarian tumor cell growth and migration. *The Journal of Biological Chemistry*, *282*(27), 19426–19441. https://doi.org/10.1074/jbc.M610054200

Bozycki, L., Łukasiewicz, K., Matryba, P., & Pikula, S. (2018). Whole-body clearing, staining and screening of calcium deposits in the mdx mouse model of Duchenne muscular dystrophy. *Skeletal Muscle*, *8*(1). https://doi.org/10.1186/s13395-018-0168-8

Brent, A. E., Braun, T., & Tabin, C. J. (2005). Genetic analysis of interactions between the somitic muscle, cartilage and tendon cell lineages during mouse development. *Development*, *132*(3), 515–528. https://doi.org/10.1242/dev.01605

Brent, A. E., Schweitzer, R., & Tabin, C. J. (2003). A somitic compartment of tendon progenitors. *Cell*, *113*(2), 235–248. https://doi.org/10.1016/S0092-8674(03)00268-X

Brent, A. E., & Tabin, C. J. (2004). FGF acts directly on the somitic tendon progenitors through the Ets transcription factors Pea3 and Erm to regulate scleraxis expression. *Development*, *131*(16), 3885–3896. https://doi.org/10.1242/dev.01275

Brinck, J., & Heldin, P. (1999). Expression of Recombinant Hyaluronan Synthase (HAS) Isoforms in CHO Cells Reduces Cell Migration and Cell Surface CD44. *Experimental Cell Research*, *252*(2), 342–351. https://doi.org/10.1006/excr.1999.4645

Brown, A. E. X., Litvinov, R. I., Discher, D. E., Purohit, P. K., & Weisel, J. W. (2009). Multiscale mechanics of fibrin polymer: Gel stretching with protein unfolding and loss of water. *Science*, *325*(5941), 741–744. https://doi.org/10.1126/science.1172484

Brown, N. H. (2000). Cell-cell adhesion via the ECM: Integrin genetics in fly and worm. In *Matrix Biology* (Vol. 19, Issue 3, pp. 191–201). Elsevier. https://doi.org/10.1016/S0945-053X(00)00064-0

Buckingham, M. (2006). Myogenic progenitor cells and skeletal myogenesis in vertebrates. *Current Opinion in Genetics & Development*, *16*(5), 525–532. https://doi.org/10.1016/j.gde.2006.08.008

Buckingham, M., Bajard, L., Chang, T., Daubas, P., Hadchouel, J., Meilhac, S., Montarras, D., Rocancourt, D., & Relaix, F. (2003). The formation of skeletal muscle: from somite to limb. *Journal of Anatomy*, *202*(1), 59–68. http://www.ncbi.nlm.nih.gov/pubmed/12587921

Calve, S., Isaac, J., Gumucio, J. P., & Mendias, C. L. (2012). Hyaluronic acid, HAS1, and HAS2 are significantly upregulated during muscle hypertrophy. *American Journal of Physiology. Cell Physiology*, *303*(5), C577-88. https://doi.org/10.1152/ajpcell.00057.2012

Calve, S., Odelberg, S. J., & Simon, H.-G. (2010). A transitional extracellular matrix instructs cell behavior during muscle regeneration. *Developmental Biology*, *344*(1), 259–271. https://doi.org/10.1016/j.ydbio.2010.05.007

Calve, S., Ready, A., Huppenbauer, C., Main, R., & Neu, C. P. (2015). Optical clearing in dense connective tissues to visualize cellular connectivity in situ. *PloS One*, *10*(1), e0116662. https://doi.org/10.1371/journal.pone.0116662

Camenisch, T. D., Spicer, A. P., Brehm-Gibson, T., Biesterfeldt, J., Augustine, M. L., Calabro, A., Kubalak, S., Klewer, S. E., McDonald, J. A., & McDonald, J. A. (2000). Disruption of hyaluronan synthase-2 abrogates normal cardiac morphogenesis and hyaluronan-mediated transformation of epithelium to mesenchyme. *The Journal of Clinical Investigation*, *106*(3), 349–360. https://doi.org/10.1172/JCI10272

Campbell, A. L., Shih, H.-P., Xu, J., Gross, M. K., & Kioussi, C. (2012). Regulation of Motility of Myogenic Cells in Filling Limb Muscle Anlagen by Pitx2. *PLoS ONE*, *7*(4), e35822. https://doi.org/10.1371/journal.pone.0035822

Capellini, T. D., Vaccari, G., Ferretti, E., Fantini, S., He, M., Pellegrini, M., Quintana, L., Di Giacomo, G., Sharpe, J., Selleri, L., & Zappavigna, V. (2010). Scapula development is governed by genetic interactions of Pbx1 with its family members and with Emx2 via their cooperative control of Alx1. *Development*, *137*(15), 2559–2569. https://doi.org/10.1242/dev.048819

Cartmell, J. S., & Dunn, M. G. (2000). Effect of chemical treatments on tendon cellularity and mechanical properties. *Journal of Biomedical Materials Research*, *49*(1), 134–140. https://doi.org/10.1002/(SICI)1097-4636(200001)49:1<134::AID-JBM17>3.0.CO;2-D

Chargé, S. B. P., & Rudnicki, M. A. (2004). Cellular and molecular regulation of muscle regeneration. *Physiological Reviews*, *84*(1), 209–238. https://doi.org/10.1152/physrev.00019.2003

Charvet, B., Malbouyres, M., Pagnon-Minot, A., Ruggiero, F., & Le Guellec, D. (2011). Development of the zebrafish myoseptum with emphasis on the myotendinous junction. *Cell and Tissue Research*, *346*(3), 439–449. https://doi.org/10.1007/s00441-011-1266-7

Charvet, B., Ruggiero, F., & Le Guellec, D. (2012). The development of the myotendinous junction. A review. In *Muscles, Ligaments and Tendons Journal* (Vol. 2, Issue 2, pp. 53–63). CIC Edizioni Internazionali. /pmc/articles/PMC3666507/?report=abstract

Chen, X. K., & Walters, T. J. (2013). Muscle-derived decellularised extracellular matrix improves functional recovery in a rat latissimus dorsi muscle defect model. *Journal of Plastic, Reconstructive & Aesthetic Surgery : JPRAS*, *66*(12), 1750–1758. https://doi.org/10.1016/j.bjps.2013.07.037

Cheng, L. S., Kang, H. W., & Cho, D. W. (2006). Improvement of the representative volume element method for 3-D scaffold simulation. *Journal of Mechanical Science and Technology*, *20*(10), 1722–1729. https://doi.org/10.1007/BF02916276

Chevallier, A., & Kieny, M. (1982). On the role of the connective tissue in the patterning of the chick limb musculature. *Wilhelm Roux's Archives of Developmental Biology*, *191*(4), 277–280. https://doi.org/10.1007/BF00848416

Chevallier, A., Kieny, M., & Mauger, A. (1977). Limb-somite relationship: origin of the limb musculature. *Development*, *41*(1).

Chollet, F., others, Chollet, F., & others. (2018). Keras: The Python Deep Learning library. *Ascl*, ascl:1806.022. https://ui.adsabs.harvard.edu/abs/2018ascl.soft06022C/abstract

Christ, B., & Brand-Saberi, B. (2002). Limb muscle development. *International Journal of Developmental Biology*, *46*(7), 905–914. https://doi.org/10.1387/ijdb.12455628

Chung, K., Wallace, J., Kim, S.-Y., Kalyanasundaram, S., Andalman, A. S., Davidson, T. J., Mirzabekov, J. J., Zalocusky, K. A., Mattis, J., Denisin, A. K., Pak, S., Bernstein, H., Ramakrishnan, C., Grosenick, L., Gradinaru, V., & Deisseroth, K. (2013). Structural and molecular interrogation of intact biological systems. *Nature*, *497*(7449), 332–337. https://doi.org/10.1038/nature12107

Clague, D. S., & Phillips, R. J. (1997). A numerical calculation of the hydraulic permeability of three-dimensional disordered fibrous media. *Physics of Fluids*, *9*(6), 1562–1572. https://doi.org/10.1063/1.869278

Clarkin, C. E., Allen, S., Wheeler-Jones, C. P., Bastow, E. R., & Pitsillides, A. A. (2011). Reduced chondrogenic matrix accumulation by 4-methylumbelliferone reveals the potential for selective targeting of UDP-glucose dehydrogenase. *Matrix Biology*, *30*(3), 163–168. https://doi.org/10.1016/j.matbio.2011.01.002

Colasanto, M. P., Eyal, S., Mohassel, P., Bamshad, M., Bonnemann, C. G., Zelzer, E., Moon, A. M., & Kardon, G. (2016). Development of a subset of forelimb muscles and their attachment sites requires the ulnar-mammary syndrome gene Tbx3. *Disease Models & Mechanisms*, *9*(11), 1257–1269. https://doi.org/10.1242/dmm.025874

Cronin, E. M., Thurmond, F. A., Bassel-Duby, R., Williams, R. S., Wright, W. E., Nelson, K. D., & Garner, H. R. (2004). Protein-coated poly(L-lactic acid) fibers provide a substrate for differentiation of human skeletal muscle cells. *Journal of Biomedical Materials Research. Part A*, *69*(3), 373–381. https://doi.org/10.1002/jbm.a.30009

Csapo, R., Gumpenberger, M., & Wessner, B. (2020). Skeletal Muscle Extracellular Matrix – What Do We Know About Its Composition, Regulation, and Physiological Roles? A Narrative Review. In *Frontiers in Physiology* (Vol. 11, p. 253). Frontiers Media S.A. https://doi.org/10.3389/fphys.2020.00253

D'Cruz, R. (2016). Identification of PDLIM7 as a Nedd4-1 substrate in the regulation of skeletal muscle mass. *Undefined*.

Derwin, K. A., Soslowsky, L. J., Kimura, J. H., & Plaas, A. H. (2001). Proteoglycans and glycosaminoglycan fine structure in the mouse tail tendon fascicle. *Journal of Orthopaedic Research*, *19*(2), 269–277. https://doi.org/10.1016/S0736-0266(00)00032-2

Dhume, R. Y., & Barocas, V. H. (2017). Fiber-Network Modeling in Biomechanics: Theoretical and Analytical Approaches. In *Studies in Mechanobiology, Tissue Engineering and Biomaterials* (Vol. 20, pp. 271–307). Springer. https://doi.org/10.1007/978-3-319-41475-1_7

Dicker, K. T., Gurski, L. A., Pradhan-Bhatt, S., Witt, R. L., Farach-Carson, M. C., & Jia, X. (2014). Hyaluronan: a simple polysaccharide with diverse biological functions. *Acta Biomaterialia*, *10*(4), 1558–1570. https://doi.org/10.1016/j.actbio.2013.12.019

Driessen, N. J. B., Bouten, C. V. C., & Baaijens, F. P. T. (2005). A structural constitutive model for collagenous cardiovascular tissues incorporating the angular fiber distribution. *Journal of Biomechanical Engineering*, *127*(3), 494–503. https://doi.org/10.1115/1.1894373

Dunkman, A. A., Buckley, M. R., Mienaltowski, M. J., Adams, S. M., Thomas, S. J., Satchell, L., Kumar, A., Pathmanathan, L., Beason, D. P., Iozzo, R. V., Birk, D. E., & Soslowsky, L. J. (2014). The tendon injury response is influenced by decorin and biglycan. *Annals of Biomedical Engineering*, *42*(3), 619–630. https://doi.org/10.1007/s10439-013-0915-2

Dzwonek, J., & Wilczynski, G. M. (2015). CD44: molecular interactions, signaling and functions in the nervous system. *Frontiers in Cellular Neuroscience*, *9*, 175. https://doi.org/10.3389/fncel.2015.00175

Edom-Vovard, F., & Duprez, D. (2004). Signals Regulating Tendon Formation during Chick Embryonic Development. In *Developmental Dynamics* (Vol. 229, Issue 3, pp. 449–457). Dev Dyn. https://doi.org/10.1002/dvdy.10481

Edom-Vovard, F., Schuler, B., Bonnin, M.-A., Teillet, M.-A., & Duprez, D. (2002). Fgf4 Positively Regulates scleraxis and Tenascin Expression in Chick Limb Tendons. *Developmental Biology*, *247*(2), 351–366. https://doi.org/10.1006/DBIO.2002.0707

Engleka, K. A., Gitler, A. D., Zhang, M., Zhou, D. D., High, F. A., & Epstein, J. A. (2005). Insertion of Cre into the Pax3 locus creates a new allele of Splotch and identifies unexpected Pax3 derivatives. *Developmental Biology*, *280*(2), 396–406. https://doi.org/10.1016/j.ydbio.2005.02.002

Epstein, D. J., Vogan, K. J., Trasler, D. G., & Gros, P. (1993). A mutation within intron 3 of the Pax-3 gene produces aberrantly spliced mRNA transcripts in the splotch (Sp) mouse mutant. *Proceedings of the National Academy of Sciences of the United States of America*, *90*(2), 532–536. https://doi.org/10.1073/pnas.90.2.532

Faassen, A. E., Schrager, J. A., Klein, D. J., Oegema, T. R., Couchman, J. R., & McCarthy, J. B. (1992). A cell surface chondroitin sulfate proteoglycan, immunologically related to CD44, is involved in type I collagen-mediated melanoma cell motility and invasion. *The Journal of Cell Biology*, *116*(2), 521–531. http://www.ncbi.nlm.nih.gov/pubmed/1730766

Frankel, A. L., Jones, R. E., & Swiler, L. P. (2019). Tensor basis Gaussian process models of hyperelastic materials. *ArXiv*. https://doi.org/10.1615/jmachlearnmodelcomput.2020033325

Frantz, C., Stewart, K. M., & Weaver, V. M. (2010). The extracellular matrix at a glance. *Journal of Cell Science*, *123*(Pt 24), 4195–4200. https://doi.org/10.1242/jcs.023820

Franz, T. (1989). Persistent truncus arteriosus in the Splotch mutant mouse. *Anatomy and Embryology*, *180*(5), 457–464. https://doi.org/10.1007/BF00305120

Fraser, J. R., Laurent, T. C., & Laurent, U. B. (1997). Hyaluronan: its nature, distribution, functions and turnover. *Journal of Internal Medicine*, *242*(1), 27–33. http://www.ncbi.nlm.nih.gov/pubmed/9260563

Fukashiro, S., Rob, M., Ichinose, Y., Kawakami, Y., & Fukunaga, T. (1995). Ultrasonography gives directly but noninvasively elastic characteristic of human tendon in vivo. *European Journal of Applied Physiology and Occupational Physiology*, *71*(6), 555–557. https://doi.org/10.1007/BF00238560

Galloway, M. T., Lalley, A. L., & Shearn, J. T. (2013). The role of mechanical loading in tendon development, maintenance, injury, and repair. In *Journal of Bone and Joint Surgery - Series A* (Vol. 95, Issue 17, pp. 1620–1628). Journal of Bone and Joint Surgery Inc. https://doi.org/10.2106/JBJS.L.01004

Gelse, K., Pöschl, E., & Aigner, T. (2003). Collagens - Structure, function, and biosynthesis. *Advanced Drug Delivery Reviews*, *55*(12), 1531–1546. https://doi.org/10.1016/j.addr.2003.08.002

Ghatak, S., Maytin, E. V., MacK, J. A., Hascall, V. C., Atanelishvili, I., Moreno Rodriguez, R., Markwald, R. R., & Misra, S. (2015). Roles of Proteoglycans and Glycosaminoglycans in Wound Healing and Fibrosis. In *International Journal of Cell Biology* (Vol. 2015). Hindawi Publishing Corporation. https://doi.org/10.1155/2015/834893

Gillies, A. R., & Lieber, R. L. (2011). Structure and function of the skeletal muscle extracellular matrix. In *Muscle and Nerve* (Vol. 44, Issue 3, pp. 318–331). John Wiley & Sons, Ltd. https://doi.org/10.1002/mus.22094

Gjorevski, N., Piotrowski, A. S., Varner, V. D., & Nelson, C. M. (2015). Dynamic tensile forces drive collective cell migration through three-dimensional extracellular matrices. *Scientific Reports*, *5*(1), 11458. https://doi.org/10.1038/srep11458

Gómez-Gaviro, M. V., Sanderson, D., Ripoll, J., & Desco, M. (2020). Biomedical Applications of Tissue Clearing and Three-Dimensional Imaging in Health and Disease. In *iScience* (Vol. 23, Issue 8, p. 101432). Elsevier Inc. https://doi.org/10.1016/j.isci.2020.101432

Gomez, D., Natan, S., Shokef, Y., & Lesman, A. (2019). Mechanical Interaction between Cells Facilitates Molecular Transport. *Advanced Biosystems*, *3*(12), 1900192. https://doi.org/10.1002/adbi.201900192

Goodison, S., Urquidi, V., & Tarin, D. (1999). CD44 cell adhesion molecules. *Molecular Pathology : MP*, *52*(4), 189–196. http://www.ncbi.nlm.nih.gov/pubmed/10694938

Gosline, J., Lillie, M., Carrington, E., Guerette, P., Ortlepp, C., & Savage, K. (2002). Elastic proteins: Biological roles and mechanical properties. *Philosophical Transactions of the Royal Society B: Biological Sciences*, *357*(1418), 121–132. https://doi.org/10.1098/rstb.2001.1022

Gouëffic, Y., Guilluy, C., Guerin, P., Patra, P., Pacaud, P., & Loirand, G. (2006). Hyaluronan induces vascular smooth muscle cell migration through RHAMM-mediated PI3K-dependent Rac activation. *Cardiovascular Research*, *72*(2), 339–348. https://doi.org/10.1016/j.cardiores.2006.07.017

Grasman, J. M., Zayas, M. J., Page, R. L., & Pins, G. D. (2015). Biomimetic scaffolds for regeneration of volumetric muscle loss in skeletal muscle injuries. *Acta Biomaterialia*, *25*, 2–15. https://doi.org/10.1016/j.actbio.2015.07.038

Gratton, E. (2011). Deeper Tissue Imaging with Total Detection. *Science*, *331*(6020), 1016–1017. https://doi.org/10.1126/science.1201542

Griffin, C. A., Apponi, L. H., Long, K. K., & Pavlath, G. K. (2010). Chemokine expression and control of muscle cell migration during myogenesis. *Journal of Cell Science*, *123*(18), 3052–3060. https://doi.org/10.1242/jcs.066241

Grounds, M. D. (2008). Complexity of Extracellular Matrix and Skeletal Muscle Regeneration. In *Skeletal Muscle Repair and Regeneration* (pp. 269–302). Springer Netherlands. https://doi.org/10.1007/978-1-4020-6768-6_13

Grzelkowska-Kowalczyk, K., Grabiec, K., Tokarska, J., Gajewska, M., Błaszczyk, M., & Milewska, M. (2015). Insulin-Like Growth Factor-I Increases Laminin, Integrin Subunits and Metalloprotease ADAM12 in Mouse Myoblasts. *Folia Biologica*, *63*(4), 241–247. http://www.ncbi.nlm.nih.gov/pubmed/26975138

Guerquin, M. J., Charvet, B., Nourissat, G., Havis, E., Ronsin, O., Bonnin, M. A., Ruggiu, M., Olivera-Martinez, I., Robert, N., Lu, Y., Kadler, K. E., Baumberger, T., Doursounian, L., Berenbaum, F., & Duprez, D. (2013). Transcription factor EGR1 directs tendon differentiation and promotes tendon repair. *Journal of Clinical Investigation*, *123*(8), 3564–3576. https://doi.org/10.1172/JCI67521

Gullberg, D., Tiger, C.-F., & Velling, T. (1999). Laminins during muscle development and in muscular dystrophies. *Cellular and Molecular Life Sciences*, *56*(5), 442–460. https://doi.org/10.1007/PL00000616

Guthold, M., Liu, W., Stephens, B., Lord, S. T., Hantgan, R. R., Erie, D. A., Taylor, R. M., & Superfinell, R. (2004). Visualization and mechanical manipulations of individual fibrin fibers suggest that fiber cross section has fractal dimension 1.3. *Biophysical Journal*, *87*(6), 4226–4236. https://doi.org/10.1529/biophysj.104.042333

Hadi, M. F., Sander, E. A., Ruberti, J. W., & Barocas, V. H. (2012). Simulated remodeling of loaded collagen networks via strain-dependent enzymatic degradation and constant-rate fiber growth. *Mechanics of Materials*, *44*, 72–82. https://doi.org/10.1016/j.mechmat.2011.07.003

Hall, B. K., & Herring, S. W. (1990). Paralysis and growth of the musculoskeletal system in the embryonic chick. *Journal of Morphology*, *206*(1), 45–56. https://doi.org/10.1002/jmor.1052060105

Hallmann, R., Horn, N., Selg, M., Wendler, O., Pausch, F., & Sorokin, L. M. (2005). Expression and function of laminins in the embryonic and mature vasculature. In *Physiological Reviews* (Vol. 85, Issue 3, pp. 979–1000). American Physiological Society. https://doi.org/10.1152/physrev.00014.2004

Hamilton, S. R., Fard, S. F., Paiwand, F. F., Tolg, C., Veiseh, M., Wang, C., McCarthy, J. B., Bissell, M. J., Koropatnick, J., & Turley, E. A. (2007). The hyaluronan receptors CD44 and Rhamm (CD168) form complexes with ERK1,2 that sustain high basal motility in breast cancer cells. *The Journal of Biological Chemistry*, *282*(22), 16667–16680. https://doi.org/10.1074/jbc.M702078200

Han, Y. L., Ronceray, P., Xu, G., Malandrino, A., Kamm, R. D., Lenz, M., Broedersz, C. P., & Guo, M. (2018). Cell contraction induces long-ranged stress stiffening in the extracellular matrix. *Proceedings of the National Academy of Sciences of the United States of America*, *115*(16), 4075–4080. https://doi.org/10.1073/pnas.1722619115

Hanson, A. N., & Bentley, J. P. (1983). Quantitation of Type I to type III collagen ratios in small samples of human tendon, blood vessels, and atherosclerotic plaque. *Analytical Biochemistry*, *130*(1), 32–40. https://doi.org/10.1016/0003-2697(83)90646-2

Hardwick, C., Hoare, K., Owens, R., Hohn, H. P., Hook, M., Moore, D., Cripps, V., Austen, L., Nance, D. M., & Turley, E. A. (1992). Molecular cloning of a novel hyaluronan receptor that mediates tumor cell motility. *The Journal of Cell Biology*, *117*(6), 1343–1350. http://www.ncbi.nlm.nih.gov/pubmed/1376732

Hasson, P. (2011). "Soft" tissue patterning: Muscles and tendons of the limb take their form. *Developmental Dynamics*, *240*(5), 1100–1107. https://doi.org/10.1002/dvdy.22608

Hasson, P., DeLaurier, A., Bennett, M., Grigorieva, E., Naiche, L. A., Papaioannou, V. E., Mohun, T. J., & Logan, M. P. O. (2010). Tbx4 and Tbx5 Acting in Connective Tissue Are Required for Limb Muscle and Tendon Patterning. *Developmental Cell*, *18*(1), 148–156. https://doi.org/10.1016/j.devcel.2009.11.013

Hatano, H., Shigeishi, H., Kudo, Y., Higashikawa, K., Tobiume, K., Takata, T., & Kamata, N. (2011). RHAMM/ERK interaction induces proliferative activities of cementifying fibroma cells through a mechanism based on the CD44-EGFR. *Laboratory Investigation; a Journal of Technical Methods and Pathology*, *91*(3), 379–391. https://doi.org/10.1038/labinvest.2010.176

Hatano, H., Shigeishi, H., Kudo, Y., Higashikawa, K., Tobiume, K., Takata, T., & Kamata, N. (2012). Overexpression of receptor for hyaluronan-mediated motility (RHAMM) in MC3T3-E1 cells induces proliferation and differentiation through phosphorylation of ERK1/2. *Journal of Bone and Mineral Metabolism*, *30*(3), 293–303. https://doi.org/10.1007/s00774-011-0318-0

Heinegård, D. (2009). Proteoglycans and more - From molecules to biology. In *International Journal of Experimental Pathology* (Vol. 90, Issue 6, pp. 575–586). Int J Exp Pathol. https://doi.org/10.1111/j.1365-2613.2009.00695.x

Helmbacher, F., & Stricker, S. (2020). Tissue cross talks governing limb muscle development and regeneration. In *Seminars in Cell and Developmental Biology* (Vol. 104, pp. 14–30). Elsevier Ltd. https://doi.org/10.1016/j.semcdb.2020.05.005

Heussinger, C., Schaefer, B., & Frey, E. (2007). Nonaffine rubber elasticity for stiff polymer networks. *Physical Review E - Statistical, Nonlinear, and Soft Matter Physics*, *76*(3). https://doi.org/10.1103/PhysRevE.76.031906

Hibino, S., Shibuya, M., Hoffman, M. P., Engbring, J. A., Hossain, R., Mochizuki, M., Kudoh, S., Nomizu, M., & Kleinman, H. K. (2005). Laminin α5 Chain Metastasis- and Angiogenesis-Inhibiting Peptide Blocks Fibroblast Growth Factor 2 Activity by Binding to the Heparan Sulfate Chains of CD44. *Cancer Research*, *65*(22), 10494–10501. https://doi.org/10.1158/0008-5472.CAN-05-0314

Hilberg, F., Protin, U., Schweighoffer, T., & Jochum, W. (2018). CD44-Deficient Mice Develop Normally with Changes in Subpopulations and Recirculation of Lymphocyte Subsets. *J Immunol References*, *4917*, 4917–4923. http://www.jimmunol.org/content/163/9/http://www.jimmunol.org/content/163/9/4917.full#ref-list-1

Hong, S. M., Noë, M., Hruban, C. A., Thompson, E. D., Wood, L. D., & Hruban, R. H. (2019). A “clearer” View of Pancreatic Pathology: A Review of Tissue Clearing and Advanced Microscopy Techniques. In *Advances in Anatomic Pathology* (Vol. 26, Issue 1, pp. 31–39). Lippincott Williams and Wilkins. https://doi.org/10.1097/PAP.0000000000000215

Hou, B., Zhang, D., Zhao, S., Wei, M., Yang, Z., Wang, S., Wang, J., Zhang, X., Liu, B., Fan, L., Li, Y., Qiu, Z., Zhang, C., & Jiang, T. (2015). Scalable and DiI-compatible optical clearance of the mammalian brain. *Frontiers in Neuroanatomy*, *9*, 19. https://doi.org/10.3389/fnana.2015.00019

Huang, A. H. (2017). Coordinated development of the limb musculoskeletal system: Tendon and muscle patterning and integration with the skeleton. In *Developmental Biology* (Vol. 429, Issue 2, pp. 420–428). Elsevier Inc. https://doi.org/10.1016/j.ydbio.2017.03.028

Huang, A. H., Lu, H. H., & Schweitzer, R. (2015). Molecular regulation of tendon cell fate during development. *Journal of Orthopaedic Research*, *33*(6), 800–812. https://doi.org/10.1002/jor.22834

Huang, A. H., Riordan, T. J., Pryce, B., Weibel, J. L., Watson, S. S., Long, F., Lefebvre, V., Harfe, B. D., Stadler, H. S., Akiyama, H., Tufa, S. F., Keene, D. R., & Schweitzer, R. (2015). Musculoskeletal integration at the wrist underlies the modular development of limb tendons. *Development (Cambridge)*, *142*(14), 2431–2441. https://doi.org/10.1242/dev.122374

Huang, M., Sun, R., Wei, H., & Tian, Z. (2013). Simultaneous knockdown of multiple ligands of innate receptor NKG2D prevents natural killer cell-mediated fulminant hepatitis in mice. *Hepatology*, *57*(1), 277–288. https://doi.org/10.1002/hep.25959

Hudson, N. E., Houser, J. R., O'Brien, E. T., Taylor, R. M., Superfine, R., Lord, S. T., & Falvo, M. R. (2010). Stiffening of individual fibrin fibers equitably distributes strain and strengthens networks. *Biophysical Journal*, *98*(8), 1632–1640. https://doi.org/10.1016/j.bpj.2009.12.4312

Humphries, D. L., Grogan, J. A., & Gaffney, E. A. (2017). Mechanical Cell–Cell Communication in Fibrous Networks: The Importance of Network Geometry. *Bulletin of Mathematical Biology*, *79*(3), 498–524. https://doi.org/10.1007/s11538-016-0242-5

Hunt, L. C., Gorman, C., Kintakas, C., McCulloch, D. R., Mackie, E. J., & White, J. D. (2013). Hyaluronan synthesis and myogenesis: a requirement for hyaluronan synthesis during myogenic differentiation independent of pericellular matrix formation. *The Journal of Biological Chemistry*, *288*(18), 13006–13021. https://doi.org/10.1074/jbc.M113.453209

Hurt-Camejo, E., Rosengren, B., Sartipy, P., Elfsberg, K., Camejo, G., & Svensson, L. (1999). CD44, a cell surface chondroitin sulfate proteoglycan, mediates binding of interferon-gamma and some of its biological effects on human vascular smooth muscle cells. *The Journal of Biological Chemistry*, *274*(27), 18957–18964. http://www.ncbi.nlm.nih.gov/pubmed/10383394

Hutcheson, D. A., Zhao, J., Merrell, A., Haldar, M., & Kardon, G. (2009). Embryonic and fetal limb myogenic cells are derived from developmentally distinct progenitors and have different requirements for beta-catenin. *Genes & Development*, *23*(8), 997–1013. https://doi.org/10.1101/gad.1769009

Ioffe, S., & Szegedy, C. (2015). Batch normalization: Accelerating deep network training by reducing internal covariate shift. *32nd International Conference on Machine Learning, ICML 2015*, *1*, 448–456. https://arxiv.org/abs/1502.03167v3

Iozzo, R. V., & Schaefer, L. (2015). Proteoglycan form and function: A comprehensive nomenclature of proteoglycans. In *Matrix Biology* (Vol. 42, pp. 11–55). Elsevier. https://doi.org/10.1016/j.matbio.2015.02.003

Isacke, C. M., & Yarwood, H. (2002). The hyaluronan receptor, CD44. *The International Journal of Biochemistry & Cell Biology*, *34*(7), 718–721. http://www.ncbi.nlm.nih.gov/pubmed/11950588

Itano, N. (2008). Simple primary structure, complex turnover regulation and multiple roles of hyaluronan. *Journal of Biochemistry*, *144*(2), 131–137. https://doi.org/10.1093/jb/mvn046

Ito, Y., Toriuchi, N., Yoshitaka, T., Ueno-Kudoh, H., Sato, T., Yokoyama, S., Nishida, K., Akimoto, T., Takahashi, M., Miyaki, S., & Asahara, H. (2010). The Mohawk homeobox gene is a critical regulator of tendon differentiation. *Proceedings of the National Academy of Sciences of the United States of America*, *107*(23), 10538–10542. https://doi.org/10.1073/pnas.1000525107

Jacobson, A., Brinck, J., Briskin, M. J., Spicer, A. P., & Heldin, P. (2000). Expression of human hyaluronan synthases in response to external stimuli. *The Biochemical Journal*, *348 Pt 1*, 29–35. http://www.ncbi.nlm.nih.gov/pubmed/10794710

Jacobson, K. R., Lipp, S., Acuna, A., Leng, Y., Bu, Y., & Calve, S. (2020). Comparative Analysis of the Extracellular Matrix Proteome across the Myotendinous Junction. *Journal of Proteome Research*, *19*(10), 3955–3967. https://doi.org/10.1021/acs.jproteome.0c00248

Jalkanen, S., & Jalkanen, M. (1992). Lymphocyte CD44 binds the COOH-terminal heparin-binding domain of fibronectin. *The Journal of Cell Biology*, *116*(3), 817–825. http://www.ncbi.nlm.nih.gov/pubmed/1730778

Ji, W., Li, L., Eniola-Adefeso, O., Wang, Y., Liu, C., & Feng, C. (2017). Non-invasively visualizing cell-matrix interactions in two-photon excited supramolecular hydrogels. *Journal of Materials Chemistry B*, *5*(38), 7790–7795. https://doi.org/10.1039/c7tb02274c

Jong, A., Wu, C.-H., Gonzales-Gomez, I., Kwon-Chung, K. J., Chang, Y. C., Tseng, H.-K., Cho, W.-L., & Huang, S.-H. (2012). Hyaluronic acid receptor CD44 deficiency is associated with decreased Cryptococcus neoformans brain infection. *The Journal of Biological Chemistry*, *287*(19), 15298–15306. https://doi.org/10.1074/jbc.M112.353375

Jozsa, L., Lehto, M., Kannus, P., Kvist, M., Reffy, A., Vieno, T., Järvinen, M., Demel, S., & Elek, E. (1989). Fibronectin and laminin in achilles tendon. *Acta Orthopaedica*, *60*(4), 469–471. https://doi.org/10.3109/17453678909149322

Kakizaki, I., Kojima, K., Takagaki, K., Endo, M., Kannagi, R., Ito, M., Maruo, Y., Sato, H., Yasuda, T., Mita, S., Kimata, K., & Itano, N. (2004). A novel mechanism for the inhibition of hyaluronan biosynthesis by 4-methylumbelliferone. *The Journal of Biological Chemistry*, *279*(32), 33281–33289. https://doi.org/10.1074/jbc.M405918200

Kamelger, F. S., Marksteiner, R., Margreiter, E., Klima, G., Wechselberger, G., Hering, S., & Piza, H. (2004). A comparative study of three different biomaterials in the engineering of skeletal muscle using a rat animal model. *Biomaterials*, *25*(9), 1649–1655. http://www.ncbi.nlm.nih.gov/pubmed/14697866

Kannus, P. (2000). Structure of the tendon connective tissue. *Scandinavian Journal of Medicine and Science in Sports*, *10*(6), 312–320. https://doi.org/10.1034/j.1600-0838.2000.010006312.x

Kaplan, P. (2005). Skeletal Dysplasias and Connective Tissue Disorders. In *Avery's Diseases of the Newborn* (pp. 279–299). Elsevier Inc. https://doi.org/10.1016/B978-072169347-7.50026-3

Kardon, G. (1998). Muscle and tendon morphogenesis in the avian hind limb. *Development*, *125*(20).

Kardon, Gabrielle, Harfe, B. D., & Tabin, C. J. (2003). A Tcf4-positive mesodermal population provides a prepattern for vertebrate limb muscle patterning. *Developmental Cell*, *5*(6), 937–944. http://www.ncbi.nlm.nih.gov/pubmed/14667415

Kastelic, J., Galeski, A., & Baer, E. (1978). The multicomposite structure of tendon. *Connective Tissue Research*, *6*(1), 11–23. https://doi.org/10.3109/03008207809152283

Kaur, J., & Reinhardt, D. P. (2015). Extracellular Matrix (ECM) Molecules. In *Stem Cell Biology and Tissue Engineering in Dental Sciences* (pp. 25–45). Elsevier Inc. https://doi.org/10.1016/B978-0-12-397157-9.00003-5

Kavanagh, E., Church, V. L., Osborne, A. C., Lamb, K. J., Archer, C. W., Francis-West, P. H., & Pitsillides, A. A. (2006). Differential regulation of GDF-5 and FGF-2/4 by immobilisation in ovo exposes distinct roles in joint formation. *Developmental Dynamics*, *235*(3), 826–834. https://doi.org/10.1002/dvdy.20679

Kaya, G., Rodriguez, I., Jorcano, J. L., Vassalli, P., & Stamenkovic, I. (1997). Selective suppression of CD44 in keratinocytes of mice bearing an antisense CD44 transgene driven by a tissue-specific promoter disrupts hyaluronate metabolism in the skin and impairs keratinocyte proliferation. *Genes & Development*, *11*(8), 996–1007. http://www.ncbi.nlm.nih.gov/pubmed/9136928

Ke, M.-T., Fujimoto, S., & Imai, T. (2013). SeeDB: a simple and morphology-preserving optical clearing agent for neuronal circuit reconstruction. *Nature Neuroscience*, *16*(8), 1154–1161. https://doi.org/10.1038/nn.3447

Kerfriden, P., Goury, O., Rabczuk, T., & Bordas, S. P. A. (2013). A partitioned model order reduction approach to rationalise computational expenses in nonlinear fracture mechanics. *Computer Methods in Applied Mechanics and Engineering*, *256*, 169–188. https://doi.org/10.1016/j.cma.2012.12.004

Keskar, N. S., Mudigere, D., Nocedal, J., Smelyanskiy, M., & Tang, P. T. P. (2016). On Large-Batch Training for Deep Learning: Generalization Gap and Sharp Minima. *5th International Conference on Learning Representations, ICLR 2017 - Conference Track Proceedings*. http://arxiv.org/abs/1609.04836

Kim, J., Feng, J., Jones, C. A. R., Mao, X., Sander, L. M., Levine, H., & Sun, B. (2017). Stress-induced plasticity of dynamic collagen networks /639/766/747 /631/57/2266 article. *Nature Communications*, *8*(1), 1–7. https://doi.org/10.1038/s41467-017-01011-7

Kingma, D. P., & Ba, J. L. (2015, December 22). Adam: A method for stochastic optimization. *3rd International Conference on Learning Representations, ICLR 2015 - Conference Track Proceedings*. https://arxiv.org/abs/1412.6980v9

Kitahama, S., Gibson, M. A., Hatzinikolas, G., Hay, S., Kuliwaba, J. L., Evdokiou, A., Atkins, G. J., & Findlay, D. M. (2000). Expression of fibrillins and other microfibril-associated proteins in human bone and osteoblast-like cells. *Bone*, *27*(1), 61–67. https://doi.org/10.1016/S8756-3282(00)00292-1

Kjaer, M. (2004). Role of Extracellular Matrix in Adaptation of Tendon and Skeletal Muscle to Mechanical Loading. In *Physiological Reviews* (Vol. 84, Issue 2, pp. 649–698). American Physiological Society. https://doi.org/10.1152/physrev.00031.2003

Knudsen, A. B., Larsen, M., Mackey, A. L., Hjort, M., Hansen, K. K., Qvortrup, K., Kjær, M., & Krogsgaard, M. R. (2015). The human myotendinous junction: An ultrastructural and 3D analysis study. *Scandinavian Journal of Medicine and Science in Sports*, *25*(1), e116–e123. https://doi.org/10.1111/sms.12221

Knudson, C. B. (2003). Hyaluronan and CD44: Strategic players for cell-matrix interactions during chondrogenesis and matrix assembly. *Birth Defects Research Part C: Embryo Today: Reviews*, *69*(2), 174–196. https://doi.org/10.1002/bdrc.10013

Knudson, W., Chow, G., & Knudson, C. B. (2002). CD44-mediated uptake and degradation of hyaluronan. *Matrix Biology*, *21*(1), 15–23. https://doi.org/10.1016/S0945-053X(01)00186-X

Koshida, S., Kishimoto, Y., Ustumi, H., Shimizu, T., Furutani-Seiki, M., Kondoh, H., & Takada, S. (2005). Integrinα5-dependent fibronectin accumulation for maintenance of somite boundaries in zebrafish embryos. *Developmental Cell*, *8*(4), 587–598. https://doi.org/10.1016/j.devcel.2005.03.006

Kostrominova, T. Y. (2011). Application of WGA lectin staining for visualization of the connective tissue in skeletal muscle, bone, and ligament/tendon studies. *Microscopy Research and Technique*, *74*(1), 18–22. https://doi.org/10.1002/jemt.20865

Kostrominova, T. Y., Calve, S., Arruda, E. M., & Larkin, L. M. (2009). Ultrastructure of myotendinous junctions in tendon-skeletal muscle constructs engineered in vitro. *Histology and Histopathology*, *24*(5), 541–550. https://doi.org/10.14670/HH-24.541

Kotlarchyk, M. A., Shreim, S. G., Alvarez-Elizondo, M. B., Estrada, L. C., Singh, R., Valdevit, L., Kniazeva, E., Gratton, E., Putnam, A. J., & Botvinick, E. L. (2011). Concentration Independent Modulation of Local Micromechanics in a Fibrin Gel. *PLoS ONE*, *6*(5), e20201. https://doi.org/10.1371/journal.pone.0020201

Kouznetsova, V., Brekelmans, W. A. M., & Baaijens, F. P. T. (2001). Approach to micro-macro modeling of heterogeneous materials. *Computational Mechanics*, *27*(1), 37–48. https://doi.org/10.1007/s004660000212

Kuang, S., Gillespie, M. A., & Rudnicki, M. A. (2008). Niche Regulation of Muscle Satellite Cell Self-Renewal and Differentiation. In *Cell Stem Cell* (Vol. 2, Issue 1, pp. 22–31). Cell Stem Cell. https://doi.org/10.1016/j.stem.2007.12.012

Kusindarta, D. L., & Wihadmadyatami, H. (2018). The Role of Extracellular Matrix in Tissue Regeneration. In *Tissue Regeneration*. InTech. https://doi.org/10.5772/intechopen.75728

Kuwajima, T., Sitko, A. A., Bhansali, P., Jurgens, C., Guido, W., & Mason, C. (2013). ClearT: a detergent- and solvent-free clearing method for neuronal and non-neuronal tissue. *Development*, *140*(6), 1364–1368. https://doi.org/10.1242/dev.091844

Lai, V. K., Lake, S. P., Frey, C. R., Tranquillo, R. T., & Barocas, V. H. (2012). Mechanical behavior of collagen-fibrin co-gels reflects transition from series to parallel interactions with increasing collagen content. *Journal of Biomechanical Engineering*, *134*(1). https://doi.org/10.1115/1.4005544

Le, B. A., Yvonnet, J., & He, Q.-C. (2015). Computational homogenization of nonlinear elastic materials using neural networks. *International Journal for Numerical Methods in Engineering*, *104*(12), 1061–1084. https://doi.org/10.1002/nme.4953

LeBleu, V. S., MacDonald, B., & Kalluri, R. (2007). Structure and Function of Basement Membranes. *Experimental Biology and Medicine*, *232*(9), 1121–1129. https://doi.org/10.3181/0703-MR-72

Lee, E., Choi, J., Jo, Y., Kim, J. Y., Jang, Y. J., Lee, H. M., Kim, S. Y., Lee, H.-J., Cho, K., Jung, N., Hur, E. M., Jeong, S. J., Moon, C., Choe, Y., Rhyu, I. J., Kim, H., & Sun, W. (2016). ACT-PRESTO: Rapid and consistent tissue clearing and labeling method for 3-dimensional (3D) imaging. *Scientific Reports*, *6*(1), 18631. https://doi.org/10.1038/srep18631

Lejard, V., Blais, F., Guerquin, M. J., Bonnet, A., Bonnin, M. A., Havis, E., Malbouyres, M., Bidaud, C. B., Maro, G., Gilardi-Hebenstreit, P., Rossert, J., Ruggiero, F., & Duprez, D. (2011). EGR1 and EGR2 involvement in vertebrate tendon differentiation. *Journal of Biological Chemistry*, *286*(7), 5855–5867. https://doi.org/10.1074/jbc.M110.153106

Leng, Y., Abdullah, A., Wendt, M. K., & Calve, S. (2019). Hyaluronic acid, CD44 and RHAMM regulate myoblast behavior during embryogenesis. *Matrix Biology*, *78–79*, 236–254. https://doi.org/10.1016/j.matbio.2018.08.008

Lesley, J., Hyman, R., & Kincade, P. W. (1993). CD44 and its interaction with extracellular matrix. *Advances in Immunology*, *54*, 271–335. http://www.ncbi.nlm.nih.gov/pubmed/8379464

Lesman, A., Notbohm, J., Tirrell, D. A., & Ravichandran, G. (2014). Contractile forces regulate cell division in three-dimensional environments. *Journal of Cell Biology*, *205*(2), 155–162. https://doi.org/10.1083/jcb.201309029

Li, Ying, Qiu, Q., Watson, S. S., Schweitzer, R., & Johnson, R. L. (2010). Uncoupling skeletal and connective tissue patterning: Conditional deletion in cartilage progenitors reveals cell-autonomous requirements for Lmx1b in dorsal-ventral limb patterning. *Development*, *137*(7), 1181–1188. https://doi.org/10.1242/dev.045237

Li, Yuting, Meng, H., Liu, Y., & Lee, B. P. (2015). Fibrin gel as an injectable biodegradable scaffold and cell carrier for tissue engineering. In *Scientific World Journal* (Vol. 2015). Hindawi Limited. https://doi.org/10.1155/2015/685690

Licup, A. J., Münster, S., Sharma, A., Sheinman, M., Jawerth, L. M., Fabry, B., Weitz, D. A., & MacKintosh, F. C. (2015). Stress controls the mechanics of collagen networks. *Proceedings of the National Academy of Sciences of the United States of America*, *112*(31), 9573–9578. https://doi.org/10.1073/pnas.1504258112

Lin, S., & Gu, L. (2015). Influence of crosslink density and stiffness on mechanical properties of type I collagen gel. *Materials*, *8*(2), 551–560. https://doi.org/10.3390/ma8020551

Lipp, S. N., Jacobson, K. R., Hains, D. S., Schwarderer, A. L., & Calve, S. (2020). 3D mapping reveals a complex and transient interstitial matrix during murine renal development. *BioRxiv*, 2020.08.20.258152. https://doi.org/10.1101/2020.08.20.258152

Litvinov, R. I., & Weisel, J. W. (2017). Fibrin mechanical properties and their structural origins. In *Matrix Biology* (Vols. 60–61, pp. 110–123). Elsevier B.V. https://doi.org/10.1016/j.matbio.2016.08.003

Liu, W., Watson, S. S., Lan, Y., Keene, D. R., Ovitt, C. E., Liu, H., Schweitzer, R., & Jiang, R. (2010). The Atypical Homeodomain Transcription Factor Mohawk Controls Tendon Morphogenesis. *Molecular and Cellular Biology*, *30*(20), 4797–4807. https://doi.org/10.1128/mcb.00207-10

Liu, Y., Sun, W., Yuan, Z., & Fish, J. (2016). A nonlocal multiscale discrete-continuum model for predicting mechanical behavior of granular materials. *International Journal for Numerical Methods in Engineering*, *106*(2), 129–160. https://doi.org/10.1002/nme.5139

Liu, Z., Moore, J. A., Aldousari, S. M., Hedia, H. S., Asiri, S. A., & Liu, W. K. (2015). A statistical descriptor based volume-integral micromechanics model of heterogeneous material with arbitrary inclusion shape. *Computational Mechanics*, *55*(5), 963–981. https://doi.org/10.1007/s00466-015-1145-2

Loeys, B. (2013). Transforming Growth Factor Beta and Bone: Lessons Learned from TGFbeta-Related Conditions. In *Osteogenesis Imperfecta: A Translational Approach to Brittle Bone Disease* (pp. 211–216). Elsevier Inc. https://doi.org/10.1016/B978-0-12-397165-4.00022-8

Lokeshwar, V. B., Lopez, L. E., Munoz, D., Chi, A., Shirodkar, S. P., Lokeshwar, S. D., Escudero, D. O., Dhir, N., & Altman, N. (2010). Antitumor activity of hyaluronic acid synthesis inhibitor 4-methylumbelliferone in prostate cancer cells. *Cancer Research*, *70*(7), 2613–2623. https://doi.org/10.1158/0008-5472.CAN-09-3185

Mäkisalo, S. E., Paavolainen, P. P., Lehto, M., Skutnabb, K., & Slätis, P. (1989). Collagen types I and III and fibronectin in healing anterior cruciate ligament after reconstruction with carbon fibre. *Injury*, *20*(2), 72–76. https://doi.org/10.1016/0020-1383(89)90143-5

Maleski, M. P., & Knudson, C. B. (1996). Hyaluronan-Mediated Aggregation of Limb Bud Mesenchyme and Mesenchymal Condensation during Chondrogenesis. *Experimental Cell Research*, *225*(1), 55–66. https://doi.org/10.1006/excr.1996.0156

Mansouri, A., Pla, P., Larue, L., & Gruss, P. (2001). Pax3 acts cell autonomously in the neural tube and somites by controlling cell surface properties. *Development*, *128*(11).

Maroudas, A. (1976). Balance between swelling pressure and collagen tension in normal and degenerate cartilage. *Nature*, *260*(5554), 808–809. https://doi.org/10.1038/260808a0

Martin, J. A., Mehr, D., Pardubsky, P. D., & Buckwalter, J. A. (2003). The role of tenascin-C in adaptation of tendons to compressive loading. *Biorheology*, *40*(1,2,3), 321–329.

Mase, V. J., Hsu, J. R., Wolf, S. E., Wenke, J. C., Baer, D. G., Owens, J., Badylak, S. F., & Walters, T. J. (2010). Clinical Application of an Acellular Biologic Scaffold for Surgical Repair of a Large, Traumatic Quadriceps Femoris Muscle Defect. *Orthopedics*. https://doi.org/10.3928/01477447-20100526-24

Masellis-Smith, A., Belch, A., Mant, M., Turley, E., & Pilarski, L. (1996). Hyaluronan-dependent motility of B cells and leukemic plasma cells in blood, but not of bone marrow plasma cells, in multiple myeloma: alternate use of receptor for hyaluronan-mediated motility (RHAMM) and CD44. *Blood*, *87*(5). http://www.bloodjournal.org/content/87/5/1891?ijkey=686355dd0fcfd6c8cda7723ddc0cf71256b454e0&keytype2=tf_ipsecsha

Massarwa, R., & Niswander, L. (2013). In toto live imaging of mouse morphogenesis and new insights into neural tube closure. *Development (Cambridge)*, *140*(1), 226–236. https://doi.org/10.1242/dev.085001

Mathew, S. J., Hansen, J. M., Merrell, A. J., Murphy, M. M., Lawson, J. A., Hutcheson, D. A., Hansen, M. S., Angus-Hill, M., & Kardon, G. (2011). Connective tissue fibroblasts and Tcf4 regulate myogenesis. *Development (Cambridge, England)*, *138*(2), 371–384. https://doi.org/10.1242/dev.057463

Matryba, P., Kaczmarek, L., & Gołąb, J. (2019). Advances in Ex Situ Tissue Optical Clearing. *Laser & Photonics Reviews*, *13*(8). https://doi.org/10.1002/LPOR.201800292@10.1002/(ISSN)1863-8899.REVIEWS

Matsumoto, K., Li, Y., Jakuba, C., Sugiyama, Y., Sayo, T., Okuno, M., Dealy, C. N., Toole, B. P., Takeda, J., Yamaguchi, Y., & Kosher, R. A. (2009). Conditional inactivation of Has2 reveals a crucial role for hyaluronan in skeletal growth, patterning, chondrocyte maturation and joint formation in the developing limb. *Development (Cambridge, England)*, *136*(16), 2825–2835. https://doi.org/10.1242/dev.038505

Maxwell, C. A., McCarthy, J., & Turley, E. (2008). Cell-surface and mitotic-spindle RHAMM: moonlighting or dual oncogenic functions? *Journal of Cell Science*, *121*(Pt 7), 925–932. https://doi.org/10.1242/jcs.022038

Mayne, R. (1989). Cartilage collagens. What Is Their Function, and Are They Involved in Articular Disease? *Arthritis & Rheumatism*, *32*(3), 241–246. https://doi.org/10.1002/anr.1780320302

Mendibil, U., Ruiz-Hernandez, R., Retegi-Carrion, S., Garcia-Urquia, N., Olalde-Graells, B., & Abarrategi, A. (2020). Tissue-Specific Decellularization Methods: Rationale and Strategies to Achieve Regenerative Compounds. *International Journal of Molecular Sciences*, *21*(15), 5447. https://doi.org/10.3390/ijms21155447

Michel, J. C., & Suquet, P. (2016). A model-reduction approach in micromechanics of materials preserving the variational structure of constitutive relations. *Journal of the Mechanics and Physics of Solids*, *90*, 254–285. https://doi.org/10.1016/j.jmps.2016.02.005

Midgley, A. C., Rogers, M., Hallett, M. B., Clayton, A., Bowen, T., Phillips, A. O., & Steadman, R. (2013). Transforming Growth Factor-β1 (TGF-β1)-stimulated Fibroblast to Myofibroblast Differentiation Is Mediated by Hyaluronan (HA)-facilitated Epidermal Growth Factor Receptor (EGFR) and CD44 Co-localization in Lipid Rafts. *Journal of Biological Chemistry*, *288*(21), 14824–14838. https://doi.org/10.1074/jbc.M113.451336

Mihai, L. A., & Goriely, A. (2015). Finite deformation effects in cellular structures with hyperelastic cell walls. *International Journal of Solids and Structures*, *53*, 107–128. https://doi.org/10.1016/j.ijsolstr.2014.10.015

Mihai, L. A., & Goriely, A. (2017). How to characterize a nonlinear elastic material? A review on nonlinear constitutive parameters in isotropic finite elasticity. *Proceedings of the Royal Society A: Mathematical, Physical and Engineering Sciences*, *473*(2207). https://doi.org/10.1098/rspa.2017.0607

Mihai, L. A., Wyatt, H., & Goriely, A. (2017a). Microstructure-based hyperelastic models for closed-cell solids. *Proceedings of the Royal Society A: Mathematical, Physical and Engineering Sciences*, *473*(2200), 20170036. https://doi.org/10.1098/rspa.2017.0036

Mihai, L. A., Wyatt, H., & Goriely, A. (2017b). A microstructure-based hyperelastic model for open-cell solids. *SIAM Journal on Applied Mathematics*, *77*(4), 1397–1416. https://doi.org/10.1137/16M1098899

Mikic, B., Wong, M., Chiquet, M., & Hunziker, E. B. (2000). Mechanical modulation of tenascin-C and collagen-XII expression during avian synovial joint formation. *Journal of Orthopaedic Research*, *18*(3), 406–415. https://doi.org/10.1002/jor.1100180312

Mikos, A. G., Herring, S. W., Ochareon, P., Elisseeff, J., Lu, H. H., Kandel, R., Schoen, F. J., Toner, M., Mooney, D., Atala, A., Van Dyke, M. E., Kaplan, D., & Vunjak-Novakovic, G. (2006). Engineering complex tissues. *Tissue Engineering*, *12*(12), 3307–3339. https://doi.org/10.1089/ten.2006.12.3307

Misra, S., Hascall, V. C., Markwald, R. R., & Ghatak, S. (2015). Interactions between Hyaluronan and Its Receptors (CD44, RHAMM) Regulate the Activities of Inflammation and Cancer. *Frontiers in Immunology*, *6*, 201. https://doi.org/10.3389/fimmu.2015.00201

Mohapatra, S., Yang, X., Wright, J. A., Turley, E. A., & Greenberg, A. H. (1996). Soluble hyaluronan receptor RHAMM induces mitotic arrest by suppressing Cdc2 and cyclin B1 expression. *Journal of Experimental Medicine*, *183*(4), 1663–1668. https://doi.org/10.1084/jem.183.4.1663

Morgan, S. C., Lee, H. Y., Relaix, F., Sandell, L. L., Levorse, J. M., & Loeken, M. R. (2008). Cardiac outflow tract septation failure in Pax3-deficient embryos is due to p53-dependent regulation of migrating cardiac neural crest. *Mechanisms of Development*, *125*(9–10), 757–767. https://doi.org/10.1016/j.mod.2008.07.003

Muiznieks, L. D., & Keeley, F. W. (2013). Molecular assembly and mechanical properties of the extracellular matrix: A fibrous protein perspective. In *Biochimica et Biophysica Acta - Molecular Basis of Disease* (Vol. 1832, Issue 7, pp. 866–875). Elsevier. https://doi.org/10.1016/j.bbadis.2012.11.022

Mullachery, V., Khera, A., & Husain, A. (2018). Bayesian Neural Networks. *ArXiv:1801.07710 [Cs, Stat]*, 1–16. http://arxiv.org/abs/1801.07710

Murchison, N. D., Price, B. A., Conner, D. A., Keene, D. R., Olson, E. N., Tabin, C. J., & Schweitzer, R. (2007). Regulation of tendon differentiation by scleraxis distinguishes force-transmitting tendons from muscle-anchoring tendons. *Development*, *134*(14), 2697–2708. https://doi.org/10.1242/dev.001933

Murphy, M. M., Lawson, J. A., Mathew, S. J., Hutcheson, D. A., & Kardon, G. (2011). Satellite cells, connective tissue fibroblasts and their interactions are crucial for muscle regeneration. *Development (Cambridge, England)*, *138*(17), 3625–3637. https://doi.org/10.1242/dev.064162

Mylona, E., Jones, K. A., Mills, S. T., & Pavlath, G. K. (2006). CD44 regulates myoblast migration and differentiation. *Journal of Cellular Physiology*, *209*(2), 314–321. https://doi.org/10.1002/jcp.20724

Nair, V., & Hinton, G. E. (2010). *Rectified Linear Units Improve Restricted Boltzmann Machines*.

Nakayama, K. H., Batchelder, C. A., Lee, C. I., & Tarantal, A. F. (2010). Decellularized Rhesus Monkey Kidney as a Three-Dimensional Scaffold for Renal Tissue Engineering. *Tissue Engineering Part A*, *16*(7), 2207–2216. https://doi.org/10.1089/ten.tea.2009.0602

Narayanan, N., & Calve, S. (2020). Extracellular matrix at the muscle–tendon interface: functional roles, techniques to explore and implications for regenerative medicine. *Connective Tissue Research*. https://doi.org/10.1080/03008207.2020.1814263

Nassari, S., Duprez, D., & Fournier-Thibault, C. (2017). Non-myogenic contribution to muscle development and homeostasis: The role of connective tissues. In *Frontiers in Cell and Developmental Biology* (Vol. 5, Issue MAR, p. 22). Frontiers Media S.A. https://doi.org/10.3389/fcell.2017.00022

Natan, S., Koren, Y., Shelah, O., Goren, S., & Lesman, A. (2020). Long-range mechanical coupling of cells in 3D fibrin gels. *Molecular Biology of the Cell*, *31*(14), 1474–1485. https://doi.org/10.1091/mbc.E20-01-0079

Neal, R. M. (1996). *Bayesian Learning for Neural Networks* (Vol. 118). Springer New York. https://doi.org/10.1007/978-1-4612-0745-0

Nedvetzki, S., Gonen, E., Assayag, N., Reich, R., Williams, R. O., Thurmond, R. L., Huang, J.-F., Neudecker, B. A., Wang, F.-S., Wang, F.-S., Turley, E. A., & Naor, D. (2004). RHAMM, a receptor for hyaluronan-mediated motility, compensates for CD44 in inflamed CD44-knockout mice: a different interpretation of redundancy. *Proceedings of the National Academy of Sciences of the United States of America*, *101*(52), 18081–18086. https://doi.org/10.1073/pnas.0407378102

Nielsen, M. J., & Karsdal, M. A. (2016). Type III Collagen. In *Biochemistry of Collagens, Laminins and Elastin: Structure, Function and Biomarkers* (pp. 21–30). Elsevier Inc. https://doi.org/10.1016/B978-0-12-809847-9.00003-9

Notbohm, J., Lesman, A., Rosakis, P., Tirrell, D. A., & Ravichandran, G. (2015). Microbuckling of fibrin provides a mechanism for cell mechanosensing. *Journal of The Royal Society Interface*, *12*(108), 20150320. https://doi.org/10.1098/rsif.2015.0320

Okita, M., Yoshimura, T., Nakano, J., Motomura, M., & Eguchi, K. (2004). Effects of reduced joint mobility on sarcomere length, collagen fibril arrangement in the endomysium, and hyaluronan in rat soleus muscle. *Journal of Muscle Research and Cell Motility*, *25*(2), 159–166. http://www.ncbi.nlm.nih.gov/pubmed/15360131

Oliver, J., Caicedo, M., Huespe, A. E., Hernández, J. A., & Roubin, E. (2017). Reduced order modeling strategies for computational multiscale fracture. *Computer Methods in Applied Mechanics and Engineering*, *313*, 560–595. https://doi.org/10.1016/j.cma.2016.09.039

Olivieri, J., Smaldone, S., & Ramirez, F. (2010). Fibrillin assemblies: extracellular determinants of tissue formation and fibrosis. *Fibrogenesis & Tissue Repair*, *3*, 24. https://doi.org/10.1186/1755-1536-3-24

Olwin, B. B., & Hall, Z. W. (1985). Developmental regulation of laminin accumulation in the extracellular matrix of a mouse muscle cell line. *Developmental Biology*, *112*(2), 359–367. https://doi.org/10.1016/0012-1606(85)90407-5

Onck, P. R., Koeman, T., Van Dillen, T., & Van Der Giessen, E. (2005). Alternative explanation of stiffening in cross-linked semiflexible networks. *Physical Review Letters*, *95*(17). https://doi.org/10.1103/PhysRevLett.95.178102

Ontell, M., & Kozeka, K. (1984). The organogenesis of murine striated muscle: A cytoarchitectural study. *American Journal of Anatomy*, *171*(2), 133–148. https://doi.org/10.1002/aja.1001710202

Orlich, M., & Kiefer, F. (2018). A qualitative comparison of ten tissue clearing techniques. *Histology and Histopathology*, *33*(2), 181–199. https://doi.org/10.14670/HH-11-903

Ott, H. C., Matthiesen, T. S., Goh, S.-K., Black, L. D., Kren, S. M., Netoff, T. I., & Taylor, D. A. (2008). Perfusion-decellularized matrix: using nature's platform to engineer a bioartificial heart. *Nature Medicine*, *14*(2), 213–221. https://doi.org/10.1038/nm1684

Ott, H. C., & Rajab, T. K. (2016). Tissue-Derived Matrices. In *In Situ Tissue Regeneration: Host Cell Recruitment and Biomaterial Design* (pp. 229–250). Elsevier Inc. https://doi.org/10.1016/B978-0-12-802225-2.00013-1

Page, R. L., Malcuit, C., Vilner, L., Vojtic, I., Shaw, S., Hedblom, E., Hu, J., Pins, G. D., Rolle, M. W., & Dominko, T. (2011). Restoration of skeletal muscle defects with adult human cells delivered on fibrin microthreads. *Tissue Engineering. Part A*, *17*(21–22), 2629–2640. https://doi.org/10.1089/ten.TEA.2011.0024

Passerieux, E., Rossignol, R., Letellier, T., & Delage, J. P. (2007). Physical continuity of the perimysium from myofibers to tendons: Involvement in lateral force transmission in skeletal muscle. *Journal of Structural Biology*, *159*(1), 19–28. https://doi.org/10.1016/j.jsb.2007.01.022

Peng, G. C. Y., Alber, M., Buganza Tepole, A., Cannon, W. R., De, S., Dura-Bernal, S., Garikipati, K., Karniadakis, G., Lytton, W. W., Perdikaris, P., Petzold, L., & Kuhl, E. (2020). Multiscale Modeling Meets Machine Learning: What Can We Learn? *Archives of Computational Methods in Engineering*, *1*, 3. https://doi.org/10.1007/s11831-020-09405-5

Perdahcioğlu, E. S., & Geijselaers, H. J. M. (2011). Constitutive modeling of two phase materials using the mean field method for homogenization. *International Journal of Material Forming*, *4*(2), 93–102. https://doi.org/10.1007/s12289-010-1007-6

Pereira, L., Lee, S. Y., Gayraud, B., Andrikopoulos, K., Shapiro, S. D., Bunton, T., Biery, N. J., Dietz, H. C., Sakai, L. Y., & Ramirez, F. (1999). Pathogenetic sequence for aneurysm revealed in mice underexpressing fibrillin-1. *Proceedings of the National Academy of Sciences of the United States of America*, *96*(7), 3819–3823. https://doi.org/10.1073/pnas.96.7.3819

Peyton, S. R., Ghajar, C. M., Khatiwala, C. B., & Putnam, A. J. (2007). The emergence of ECM mechanics and cytoskeletal tension as important regulators of cell function. In *Cell Biochemistry and Biophysics* (Vol. 47, Issue 2, pp. 300–320). Springer. https://doi.org/10.1007/s12013-007-0004-y

Pilarski, L. M., Masellis-Smith, A., Belch, A. R., Yang, B., Savani, R. C., & Turley, E. A. (1994). RHAMM, a receptor for hyaluronan-mediated motility, on normal human lymphocytes, thymocytes and malignant B cells: a mediator in B cell malignancy? *Leukemia & Lymphoma*, *14*(5–6), 363–374. https://doi.org/10.3109/10428199409049691

Platzer, W., & Kahle, W. (Werner). (2003). *Color atlas and textbook of human anatomy : in three volumes*. Thieme.

Ponta, H., Sherman, L., & Herrlich, P. A. (2003). CD44: from adhesion molecules to signalling regulators. *Nature Reviews. Molecular Cell Biology*, *4*(1), 33–45. https://doi.org/10.1038/nrm1004

Prochazka, J., Prochazkova, M., Du, W., Spoutil, F., Tureckova, J., Hoch, R., Shimogori, T., Sedlacek, R., Rubenstein, J. L., Wittmann, T., & Klein, O. D. (2015). Migration of Founder Epithelial Cells Drives Proper Molar Tooth Positioning and Morphogenesis. *Developmental Cell*, *35*(6), 713–724. https://doi.org/10.1016/j.devcel.2015.11.025

Prussing, J. E. (1986). The principal minor test for semidefinite matrices. *Journal of Guidance, Control, and Dynamics*, *9*(1), 121–122. https://doi.org/10.2514/3.20077

Pryce, B. A., Watson, S. S., Murchison, N. D., Staverosky, J. A., Dünker, N., & Schweitzer, R. (2009). Recruitment and maintenance of tendon progenitors by TGFB signaling are essential for tendon formation. *Development*, *136*(8), 1351–1361. https://doi.org/10.1242/dev.027342

Purslow, P. P. (2002). The structure and functional significance of variations in the connective tissue within muscle. *Comparative Biochemistry and Physiology - A Molecular and Integrative Physiology*, *133*(4), 947–966. https://doi.org/10.1016/S1095-6433(02)00141-1

Radotra, B., McCormick, D., & Crockard, A. (1994). CD44 plays a role in adhesive interactions between glioma cells and extracellular matrix components. *Neuropathology and Applied Neurobiology*, *20*(4), 399–405. https://doi.org/10.1111/j.1365-2990.1994.tb00986.x

Raghow, R. (2013). Connective Tissues of the Subendothelium. In *Vascular Medicine: A Companion to Braunwald's Heart Disease: Second Edition* (pp. 43–69). Elsevier Inc. https://doi.org/10.1016/B978-1-4377-2930-6.00004-5

Raghupathy, R., & Barocas, V. H. (2009). A closed-form structural model of planar fibrous tissue mechanics. *Journal of Biomechanics*, *42*(10), 1424–1428. https://doi.org/10.1016/j.jbiomech.2009.04.005

Raman, R., Sasisekharan, V., & Sasisekharan, R. (2005). Structural Insights into biological roles of protein-glycosaminoglycan interactions. In *Chemistry and Biology* (Vol. 12, Issue 3, pp. 267–277). Elsevier Ltd. https://doi.org/10.1016/j.chembiol.2004.11.020

Rees, S. G., Curtis, C. L., Dent, C. M., & Caterson, B. (2005). Catabolism of aggrecan proteoglycan aggregate components in short-term explant cultures of tendon. *Matrix Biology*, *24*(3), 219–231. https://doi.org/10.1016/j.matbio.2005.02.002

Reimann, D., Nidadavolu, K., ul Hassan, H., Vajragupta, N., Glasmachers, T., Junker, P., & Hartmaier, A. (2019). Modeling Macroscopic Material Behavior With Machine Learning Algorithms Trained by Micromechanical Simulations. *Frontiers in Materials*, *6*, 181. https://doi.org/10.3389/fmats.2019.00181

Reinhart-King, C. A., Dembo, M., & Hammer, D. A. (2008). Cell-cell mechanical communication through compliant substrates. *Biophysical Journal*, *95*(12), 6044–6051. https://doi.org/10.1529/biophysj.107.127662

Relaix, F., Rocancourt, D., Mansouri, A., & Buckingham, M. (2005). A Pax3/Pax7-dependent population of skeletal muscle progenitor cells. *Nature*, *435*(7044), 948–953. https://doi.org/10.1038/nature03594

Rhodes, J. M., & Simons, M. (2007). The extracellular matrix and blood vessel formation: Not just a scaffold: Angiogenesis Review Series. In *Journal of Cellular and Molecular Medicine* (Vol. 11, Issue 2, pp. 176–205). J Cell Mol Med. https://doi.org/10.1111/j.1582-4934.2007.00031.x

Ricard-Blum, S. (2011). The Collagen Family. *Cold Spring Harbor Perspectives in Biology*, *3*(1), 1–19. https://doi.org/10.1101/cshperspect.a004978

Ricard-Blum, S., & Ruggiero, F. (2005). The collagen superfamily: From the extracellular matrix to the cell membrane. *Pathologie Biologie*, *53*(7), 430–442. https://doi.org/10.1016/j.patbio.2004.12.024

Richardson, D. S., & Lichtman, J. W. (2015). Clarifying Tissue Clearing. *Cell*, *162*(2), 246–257. https://doi.org/10.1016/j.cell.2015.06.067

Riley, G. (2004). The pathogenesis of tendinopathy. A molecular perspective. In *Rheumatology* (Vol. 43, Issue 2, pp. 131–142). Rheumatology (Oxford). https://doi.org/10.1093/rheumatology/keg448

Riso, E.-M., Kaasik, P., & Seene, T. (2016). Remodelling of Skeletal Muscle Extracellular Matrix: Effect of Unloading and Reloading. In *Composition and Function of the Extracellular Matrix in the Human Body*. InTech. https://doi.org/10.5772/62295

Ritter, M. C., Jesudason, R., Majumdar, A., Stamenović, D., Buczek-Thomas, J. A., Stone, P. J., Nugent, M. A., & Suki, B. (2009). A zipper network model of the failure mechanics of extracellular matrices. *Proceedings of the National Academy of Sciences of the United States of America*, *106*(4), 1081–1086. https://doi.org/10.1073/pnas.0808414106

Ritty, T. M., Ditsios, K., & Starcher, B. C. (2002). Distribution of the elastic fiber and associated proteins in flexor tendon reflects function. *Anatomical Record*, *268*(4), 430–440. https://doi.org/10.1002/ar.10175

Ritty, T. M., Roth, R., & Heuser, J. E. (2003). Tendon cell array isolation reveals a previously unknown fibrillin-2-containing macromolecular assembly. *Structure*, *11*(9), 1179–1188. https://doi.org/10.1016/S0969-2126(03)00181-3

Roccabianca, S., Ateshian, G. A., & Humphrey, J. D. (2014). Biomechanical roles of medial pooling of glycosaminoglycans in thoracic aortic dissection. *Biomechanics and Modeling in Mechanobiology*, *13*(1), 13–25. https://doi.org/10.1007/s10237-013-0482-3

Rot-Nikcevic, I., Reddy, T., Downing, K. J., Belliveau, A. C., Hallgrímsson, B., Hall, B. K., & Kablar, B. (2006). Myf5 −/− :MyoD −/− amyogenic fetuses reveal the importance of early contraction and static loading by striated muscle in mouse skeletogenesis. *Development Genes and Evolution*, *216*(1), 1–9. https://doi.org/10.1007/s00427-005-0024-9

Rozario, T., & DeSimone, D. W. (2010). The extracellular matrix in development and morphogenesis: a dynamic view. *Developmental Biology*, *341*(1), 126–140. https://doi.org/10.1016/j.ydbio.2009.10.026

Rudnicki, M. S., Cirka, H. A., Aghvami, M., Sander, E. A., Wen, Q., & Billiar, K. L. (2013). Nonlinear strain stiffening is not sufficient to explain how far cells can feel on fibrous protein gels. *Biophysical Journal*, *105*(1), 11–20. https://doi.org/10.1016/j.bpj.2013.05.032

Rudzki, Z., & Jothy, S. (1997). CD44 and the adhesion of neoplastic cells. *Molecular Pathology : MP*, *50*(2), 57–71. https://doi.org/10.1136/MP.50.2.57

Rumelhart, D. E., Hinton, G. E., & Williams, R. J. (1986). Learning representations by back-propagating errors. *Nature*, *323*(6088), 533–536. https://doi.org/10.1038/323533a0

Ryan, E. A., Mockros, L. F., Weisel, J. W., & Lorand, L. (1999). Structural origins of fibrin clot rheology. *Biophysical Journal*, *77*(5), 2813–2826. https://doi.org/10.1016/S0006-3495(99)77113-4

Sab, K. (1992). On the homogenization and the simulation of random materials. *European Journal of Mechanics, A/Solids*, *11*(5), 585–607.

Sakai, L., Keene, D., Glanville, R., & Bächinger, H. (1991). Purification and partial characterization of fibrillin, a cysteine-rich structural component of connective tissue microfibrils. *Undefined*.

Salic, A., & Mitchison, T. J. (2008). A chemical method for fast and sensitive detection of DNA synthesis in vivo. *Proceedings of the National Academy of Sciences of the United States of America*, *105*(7), 2415–2420. https://doi.org/10.1073/pnas.0712168105

Sander, E. A., Stylianopoulos, T., Tranquillo, R. T., & Barocas, V. H. (2009). Image-based biomechanics of collagen-based tissue equivalents. *IEEE Engineering in Medicine and Biology Magazine*, *28*(3), 10–18. https://doi.org/10.1109/MEMB.2009.932486

Sanes, J. R. (2003). The basement membrane/basal lamina of skeletal muscle. *The Journal of Biological Chemistry*, *278*(15), 12601–12604. https://doi.org/10.1074/jbc.R200027200

Savani, R. C., Cao, G., Pooler, P. M., Zaman, A., Zhou, Z., & DeLisser, H. M. (2001). Differential involvement of the hyaluronan (HA) receptors CD44 and receptor for HA-mediated motility in endothelial cell function and angiogenesis. *The Journal of Biological Chemistry*, *276*(39), 36770–36778. https://doi.org/10.1074/jbc.M102273200

Schmits, R., Filmus, J., Gerwin, N., Senaldi, G., Kiefer, F., Kundig, T., Wakeham, A., Shahinian, A., Catzavelos, C., Rak, J., Furlonger, C., Zakarian, A., Simard, J. J., Ohashi, P. S., Paige, C. J., Gutierrez-Ramos, J. C., & Mak, T. W. (1997). CD44 regulates hematopoietic progenitor distribution, granuloma formation, and tumorigenicity. *Blood*, *90*(6), 2217–2233. http://www.ncbi.nlm.nih.gov/pubmed/9310473

Schroeter, S., & Tosney, K. W. (1991a). Spatial and temporal patterns of muscle cleavage in the chick thigh and their value as criteria for homology. *American Journal of Anatomy*, *191*(4), 325–350. https://doi.org/10.1002/aja.1001910402

Schroeter, S., & Tosney, K. W. (1991b). Ultrastructural and morphometric analysis of the separation of two thigh muscles in the chick. *American Journal of Anatomy*, *191*(4), 351–368. https://doi.org/10.1002/aja.1001910403

Schweitzer, R., Chyung, J., Murtaugh, L., Brent, A. E., Rosen, V., Olson, E., Lassar, A., & Tabin, C. (2001). Analysis of the tendon cell fate using Scleraxis, a specific marker for tendons and ligaments. *Undefined*.

Schweitzer, Ronen, Zelzer, E., & Volk, T. (2010). Connecting muscles to tendons: Tendons and musculoskeletal development in flies and vertebrates. In *Development* (Vol. 137, Issue 17, pp. 2807–2817). Oxford University Press for The Company of Biologists Limited. https://doi.org/10.1242/dev.047498

Screen, H. R. C., Berk, D. E., Kadler, K. E., Ramirez, F., & Young, M. F. (2015). Tendon functional extracellular matrix. *Journal of Orthopaedic Research*, *33*(6), 793–799. https://doi.org/10.1002/jor.22818

Seeger, M. (2004). Gaussian processes for machine learning. In *International journal of neural systems* (Vol. 14, Issue 2). MIT Press. https://doi.org/10.1142/S0129065704001899

Shahsavari, A., & Picu, R. C. (2012). Model selection for athermal cross-linked fiber networks. *Physical Review E - Statistical, Nonlinear, and Soft Matter Physics*, *86*(1), 011923. https://doi.org/10.1103/PhysRevE.86.011923

SheffieldML/GPy: Gaussian processes framework in python. (2018). https://github.com/SheffieldML/GPy

Sherman, L., Wainwright, D., Ponta, H., & Herrlich, P. (1998). A splice variant of CD44 expressed in the apical ectodermal ridge presents fibroblast growth factors to limb mesenchyme and is required for limb outgrowth. *Genes & Development*, *12*(7), 1058–1071. http://www.ncbi.nlm.nih.gov/pubmed/9531542

Shukunami, C., Oshima, Y., & Hiraki, Y. (2001). Molecular cloning of tenomodulin, a novel Chondromodulin-I related gene. *Biochemical and Biophysical Research Communications*, *280*(5), 1323–1327. https://doi.org/10.1006/bbrc.2001.4271

Shukunami, C., Takimoto, A., Oro, M., & Hiraki, Y. (2006). Scleraxis positively regulates the expression of tenomodulin, a differentiation marker of tenocytes. *Developmental Biology*, *298*(1), 234–247. https://doi.org/10.1016/j.ydbio.2006.06.036

Silverman-Gavrila, R., Silverman-Gavrila, L., Hou, G., Zhang, M., Charlton, M., & Bendeck, M. P. (2011). Rear Polarization of the Microtubule-Organizing Center in Neointimal Smooth Muscle Cells Depends on PKCα, ARPC5, and RHAMM. *The American Journal of Pathology*, *178*(2), 895–910. https://doi.org/10.1016/J.AJPATH.2010.10.001

Smith, M. M., & Melrose, J. (2015). Proteoglycans in Normal and Healing Skin. *Advances in Wound Care*, *4*(3), 152–173. https://doi.org/10.1089/wound.2013.0464

Smithmyer, M. E., Sawicki, L. A., & Kloxin, A. M. (2014). Hydrogel scaffolds as in vitro models to study fibroblast activation in wound healing and disease. In *Biomaterials Science* (Vol. 2, Issue 5, pp. 634–650). Royal Society of Chemistry. https://doi.org/10.1039/c3bm60319a

Snow, C. J., Goody, M., Kelly, M. W., Oster, E. C., Jones, R., Khalil, A., & Henry, C. A. (2008). Time-lapse analysis and mathematical characterization elucidate novel mechanisms underlying muscle morphogenesis. *PLoS Genetics*, *4*(10). https://doi.org/10.1371/journal.pgen.1000219

Solis, M. A., Chen, Y.-H., Wong, T. Y., Bittencourt, V. Z., Lin, Y.-C., & Huang, L. L. H. (2012). Hyaluronan regulates cell behavior: a potential niche matrix for stem cells. *Biochemistry Research International*, *2012*, 346972. https://doi.org/10.1155/2012/346972

Sopher, R. S., Tokash, H., Natan, S., Sharabi, M., Shelah, O., Tchaicheeyan, O., & Lesman, A. (2018). Nonlinear Elasticity of the ECM Fibers Facilitates Efficient Intercellular Communication. *Biophysical Journal*, *115*(7), 1357–1370. https://doi.org/10.1016/j.bpj.2018.07.036

Soriano, P. (1999). Generalized lacZ expression with the ROSA26 Cre reporter strain. *Nature Genetics*, *21*(1), 70–71. https://doi.org/10.1038/5007

Spicer, A P, & McDonald, J. A. (1998). Characterization and molecular evolution of a vertebrate hyaluronan synthase gene family. *The Journal of Biological Chemistry*, *273*(4), 1923–1932. http://www.ncbi.nlm.nih.gov/pubmed/9442026

Spicer, Andrew P, & Tien, J. Y. L. (2004). Hyaluronan and morphogenesis. *Birth Defects Research. Part C, Embryo Today : Reviews*, *72*(1), 89–108. https://doi.org/10.1002/bdrc.20006

Stuart, E. T., Kioussi, C., & Gruss, P. (1994). Mammalian Pax Genes. *Annual Review of Genetics*, *28*(1), 219–238. https://doi.org/10.1146/annurev.ge.28.120194.001251

Stylianopoulos, T., & Barocas, V. H. (2007). Volume-averaging theory for the study of the mechanics of collagen networks. *Computer Methods in Applied Mechanics and Engineering*, *196*(31–32), 2981–2990. https://doi.org/10.1016/j.cma.2006.06.019

Subramanian, A., Kanzaki, L. F., Galloway, J. L., & Schilling, T. F. (2018). Mechanical force regulates tendon extracellular matrix organization and tenocyte morphogenesis through TGFbeta signaling. *ELife*, *7*. https://doi.org/10.7554/eLife.38069

Subramanian, A., & Schilling, T. F. (2015). Tendon development and musculoskeletal assembly: Emerging roles for the extracellular matrix. In *Development (Cambridge)* (Vol. 142, Issue 24, pp. 4191–4204). Company of Biologists Ltd. https://doi.org/10.1242/dev.114777

Sudhakar, A., & Kalluri, R. (2010). Molecular mechanisms of angiostasis. In *Encyclopedia of the Eye* (pp. 52–59). Elsevier. https://doi.org/10.1016/B978-0-12-374203-2.00128-7

Sun, M., Connizzo, B. K., Adams, S. M., Freedman, B. R., Wenstrup, R. J., Soslowsky, L. J., & Birk, D. E. (2015). Targeted deletion of collagen V in tendons and ligaments results in a classic Ehlers-Danlos syndrome joint phenotype. *American Journal of Pathology*, *185*(5), 1436–1447. https://doi.org/10.1016/j.ajpath.2015.01.031

Svärd, A., Hammerman, M., & Eliasson, P. (2020). Elastin levels are higher in healing tendons than in intact tendons and influence tissue compliance. *The FASEB Journal*, *34*(10), 13409–13418. https://doi.org/10.1096/fj.202001255R

Takahashi, Y., Li, L., Kamiryo, M., Asteriou, T., Moustakas, A., Yamashita, H., & Heldin, P. (2005). Hyaluronan fragments induce endothelial cell differentiation in a CD44- and CXCL1/GRO1-dependent manner. *The Journal of Biological Chemistry*, *280*(25), 24195–24204. https://doi.org/10.1074/jbc.M411913200

Tepole, A. B., Nordsletten, D., Garikipati, K., & Kuhl, E. (2020). Special Issue on Uncertainty Quantification, Machine Learning, and Data-Driven Modeling of Biological Systems. In *Computer Methods in Applied Mechanics and Engineering* (Vol. 362, p. 112832). Elsevier B.V. https://doi.org/10.1016/j.cma.2020.112832

Thorpe, C. T., Birch, H. L., Clegg, P. D., & Screen, H. R. C. (2013). The role of the non-collagenous matrix in tendon function. In *International Journal of Experimental Pathology* (Vol. 94, Issue 4, pp. 248–259). John Wiley & Sons, Ltd. https://doi.org/10.1111/iep.12027

Thorsteinsdóttir, S., Deries, M., Cachaço, A. S., & Bajanca, F. (2011). The extracellular matrix dimension of skeletal muscle development. *Developmental Biology*, *354*(2), 191–207. https://doi.org/10.1016/j.ydbio.2011.03.015

Tien, J. Y. L., & Spicer, A. P. (2005). Three vertebrate hyaluronan synthases are expressed during mouse development in distinct spatial and temporal patterns. *Developmental Dynamics*, *233*(1), 130–141. https://doi.org/10.1002/dvdy.20328

Tolg, C., Hamilton, S. R., Morningstar, L., Zhang, J., Zhang, S., Esguerra, K. V, Telmer, P. G., Luyt, L. G., Harrison, R., McCarthy, J. B., & Turley, E. A. (2010). RHAMM promotes interphase microtubule instability and mitotic spindle integrity through MEK1/ERK1/2 activity. *The Journal of Biological Chemistry*, *285*(34), 26461–26474. https://doi.org/10.1074/jbc.M110.121491

Tolg, C., Hamilton, S. R., Nakrieko, K.-A., Kooshesh, F., Walton, P., McCarthy, J. B., Bissell, M. J., & Turley, E. A. (2006). Rhamm-/- fibroblasts are defective in CD44-mediated ERK1,2 motogenic signaling, leading to defective skin wound repair. *The Journal of Cell Biology*, *175*(6), 1017–1028. https://doi.org/10.1083/jcb.200511027

Tolg, C., McCarthy, J. B., Yazdani, A., & Turley, E. A. (2014). Hyaluronan and RHAMM in wound repair and the "cancerization" of stromal tissues. *BioMed Research International*, *2014*, 103923. https://doi.org/10.1155/2014/103923

Tolg, C., Poon, R., Fodde, R., Turley, E. A., & Alman, B. A. (2003). Genetic deletion of receptor for hyaluronan-mediated motility (Rhamm) attenuates the formation of aggressive fibromatosis (desmoid tumor). *Oncogene*, *22*(44), 6873–6882. https://doi.org/10.1038/sj.onc.1206811

Tolg, C., Yuan, H., Flynn, S. M., Basu, K., Ma, J., Tse, K. C. K., Kowalska, B., Vulkanesku, D., Cowman, M. K., McCarthy, J. B., & Turley, E. A. (2017). Hyaluronan modulates growth factor induced mammary gland branching in a size dependent manner. *Matrix Biology*, *63*, 117–132. https://doi.org/10.1016/j.matbio.2017.02.003

Toole, B P. (2001). Hyaluronan in morphogenesis. *Seminars in Cell & Developmental Biology*, *12*(2), 79–87. https://doi.org/10.1006/scdb.2000.0244

Toole, Bryan P. (2004). Hyaluronan: from extracellular glue to pericellular cue. *Nature Reviews. Cancer*, *4*(7), 528–539. https://doi.org/10.1038/nrc1391

Trelstad, R. L., & Hayashi, K. (1979). Tendon collagen fibrillogenesis: Intracellular subassemblies and cell surface changes associated with fibril growth. *Developmental Biology*, *71*(2), 228–242. https://doi.org/10.1016/0012-1606(79)90166-0

Trotter, J. A. (2002). Structure-function considerations of muscle-tendon junctions. *Comparative Biochemistry and Physiology - A Molecular and Integrative Physiology*, *133*(4), 1127–1133. https://doi.org/10.1016/S1095-6433(02)00213-1

Trotter, J. A., Eberhard, S., & Samora, A. (1983). Structural connections of the muscle-tendon junction. *Cell Motility*, *3*(5), 431–438. https://doi.org/10.1002/cm.970030511

Tuchin, V. V., Maksimova, I. L., Zimnyakov, D. A., Kon, I. L., Mavlyutov, A. H., & Mishin, A. A. (1997). Light propagation in tissues with controlled optical properties. *Journal of Biomedical Optics*, *2*(4), 401. https://doi.org/10.1117/12.281502

Turley, E. A., Noble, P. W., & Bourguignon, L. Y. W. (2002). Signaling properties of hyaluronan receptors. *The Journal of Biological Chemistry*, *277*(7), 4589–4592. https://doi.org/10.1074/jbc.R100038200

Twarock, S., Freudenberger, T., Poscher, E., Dai, G., Jannasch, K., Dullin, C., Alves, F., Prenzel, K., Knoefel, W. T., Stoecklein, N. H., Savani, R. C., Homey, B., & Fischer, J. W. (2011). Inhibition of oesophageal squamous cell carcinoma progression by in vivo targeting of hyaluronan synthesis. *Molecular Cancer*, *10*, 30. https://doi.org/10.1186/1476-4598-10-30

Tzaphlidou, M. (2008). Bone architecture: Collagen structure and calcium/phosphorus maps. In *Journal of Biological Physics* (Vol. 34, Issues 1-2 SPEC. ISS., pp. 39–49). Springer. https://doi.org/10.1007/s10867-008-9115-y

Urakawa, H., Nishida, Y., Wasa, J., Arai, E., Zhuo, L., Kimata, K., Kozawa, E., Futamura, N., & Ishiguro, N. (2012). Inhibition of hyaluronan synthesis in breast cancer cells by 4-methylumbelliferone suppresses tumorigenicity in vitro and metastatic lesions of bone in vivo. *International Journal of Cancer*, *130*(2), 454–466. https://doi.org/10.1002/ijc.26014

Vader, D., Kabla, A., Weitz, D., & Mahadevan, L. (2009). Strain-Induced Alignment in Collagen Gels. *PLoS ONE*, *4*(6), e5902. https://doi.org/10.1371/journal.pone.0005902

Valdivia, M., Vega-Macaya, F., & Olguín, P. (2017). Mechanical control of myotendinous junction formation and tendon differentiation during development. In *Frontiers in Cell and Developmental Biology* (Vol. 5, Issue MAR, p. 26). Frontiers Media S.A. https://doi.org/10.3389/fcell.2017.00026

Vallecillo-García, P., Orgeur, M., vom Hofe-Schneider, S., Stumm, J., Kappert, V., Ibrahim, D. M., Börno, S. T., Hayashi, S., Relaix, F., Hildebrandt, K., Sengle, G., Koch, M., Timmermann, B., Marazzi, G., Sassoon, D. A., Duprez, D., & Stricker, S. (2017). Odd skipped-related 1 identifies a population of embryonic fibro-adipogenic progenitors regulating myogenesis during limb development. *Nature Communications*, *8*(1), 1218. https://doi.org/10.1038/s41467-017-01120-3

Van Der Rest, M., & Garrone, R. (1991). Collagen family of proteins. *The FASEB Journal*, *5*(13), 2814–2823. https://doi.org/10.1096/fasebj.5.13.1916105

Van Helvert, S., Storm, C., & Friedl, P. (2018). Mechanoreciprocity in cell migration. In *Nature Cell Biology* (Vol. 20, Issue 1, pp. 8–20). Nature Publishing Group. https://doi.org/10.1038/s41556-017-0012-0

Varki, A., Cummings, R., Esko, J., Freeze, H., Hart, G., & Marth, J. (1999). *Proteoglycans and Glycosaminoglycans*. https://www.ncbi.nlm.nih.gov/books/NBK20693/

Vigetti, D., Rizzi, M., Viola, M., Karousou, E., Genasetti, A., Clerici, M., Bartolini, B., Hascall, V. C., De Luca, G., & Passi, A. (2009). The effects of 4-methylumbelliferone on hyaluronan synthesis, MMP2 activity, proliferation, and motility of human aortic smooth muscle cells. *Glycobiology*, *19*(5), 537–546. https://doi.org/10.1093/glycob/cwp022

Virtanen, P., Gommers, R., Oliphant, T. E., Haberland, M., Reddy, T., Cournapeau, D., Burovski, E., Peterson, P., Weckesser, W., Bright, J., van der Walt, S. J., Brett, M., Wilson, J., Millman, K. J., Mayorov, N., Nelson, A. R. J., Jones, E., Kern, R., Larson, E., … Vázquez-Baeza, Y. (2020). SciPy 1.0: fundamental algorithms for scientific computing in Python. *Nature Methods*, *17*(3), 261–272. https://doi.org/10.1038/s41592-019-0686-2

von der Mark, K. (2006). Structure, Biosynthesis and Gene Regulation of Collagens in Cartilage and Bone. In *Dynamics of Bone and Cartilage Metabolism* (pp. 3–40). Elsevier Inc. https://doi.org/10.1016/B978-012088562-6/50002-9

Walma, D. A. C., & Yamada, K. M. (2020). The extracellular matrix in development. In *Development (Cambridge, England)* (Vol. 147, Issue 10). NLM (Medline). https://doi.org/10.1242/dev.175596

Wang, H., Abhilash, A. S., Chen, C. S., Wells, R. G., & Shenoy, V. B. (2015). Long-range force transmission in fibrous matrices enabled by tension-driven alignment of fibers. *Biophysical Journal*, *107*(11), 2592–2603. https://doi.org/10.1016/j.bpj.2014.09.044

Wang, K., & Sun, W. C. (2018). A multiscale multi-permeability poroplasticity model linked by recursive homogenizations and deep learning. *Computer Methods in Applied Mechanics and Engineering*, *334*, 337–380. https://doi.org/10.1016/j.cma.2018.01.036

Wang, Y., Lauer, M. E., Anand, S., Mack, J. A., & Maytin, E. V. (2014). Hyaluronan synthase 2 protects skin fibroblasts against apoptosis induced by environmental stress. *The Journal of Biological Chemistry*, *289*(46), 32253–32265. https://doi.org/10.1074/jbc.M114.578377

Watson, S. S., Riordan, T. J., Pryce, B. A., & Schweitzer, R. (2009). Tendons and muscles of the mouse forelimb during embryonic development. *Developmental Dynamics*, *238*(3), 693–700. https://doi.org/10.1002/dvdy.21866

Watt, F. M., & Fujiwara, H. (2011). Cell-extracellular matrix interactions in normal and diseased skin. *Cold Spring Harbor Perspectives in Biology*, *3*(4), 1–14. https://doi.org/10.1101/cshperspect.a005124

Wen, Q., & Janmey, P. A. (2013). Effects of non-linearity on cell-ECM interactions. In *Experimental Cell Research* (Vol. 319, Issue 16, pp. 2481–2489). Academic Press Inc. https://doi.org/10.1016/j.yexcr.2013.05.017

Wenstrup, R. J., Florer, J. B., Brunskill, E. W., Bell, S. M., Chervoneva, I., & Birk, D. E. (2004). Type V collagen controls the initiation of collagen fibril assembly. *Journal of Biological Chemistry*, *279*(51), 53331–53337. https://doi.org/10.1074/jbc.M409622200

White, R. B., Biérinx, A. S., Gnocchi, V. F., & Zammit, P. S. (2010). Dynamics of muscle fibre growth during postnatal mouse development. *BMC Developmental Biology*, *10*(1), 21. https://doi.org/10.1186/1471-213X-10-21

Wilson, K., Terlouw, A., Roberts, K., & Wolchok, J. C. (2016). The characterization of decellularized human skeletal muscle as a blueprint for mimetic scaffolds. *Journal of Materials Science: Materials in Medicine*, *27*(8). https://doi.org/10.1007/s10856-016-5735-0

Wong, M., Germiller, J., Bonadio, J., & Goldstein, S. A. (1993). Neuromuscular atrophy alters collagen gene expression, pattern formation, and mechanical integrity of the chick embryo long bone. *Progress in Clinical and Biological Research*, *383 B*, 587–597. https://europepmc.org/article/med/8115375

Wong, E. V. (2020). *13.1: Introduction to Extracellular Matrix and Cell Adhesion - Biology LibreTexts*. Axolotl Academica Publishing (Biology) at Axolotl Academica Publishing. https://bio.libretexts.org/Bookshelves/Cell_and_Molecular_Biology/Book%3A_Cells_-_Molecules_and_Mechanisms_(Wong)/13%3A_Extracellular_Matrix_and_Cell_Adhesion/13.01%3A_Introduction_to_Extracellular_Matrix_and_Cell_Adhesion

Wu, M., Li, J., Engleka, K. A., Zhou, B., Min, M. L., Plotkin, J. B., & Epstein, J. A. (2008). Persistent expression of Pax3 in the neural crest causes cleft palate and defective osteogenesis in mice. *Journal of Clinical Investigation*, *118*(6), 2076–2087. https://doi.org/10.1172/JCI33715

Yang, B., Yang, B. L., Savani, R. C., & Turley, E. A. (1994). Identification of a common hyaluronan binding motif in the hyaluronan binding proteins RHAMM, CD44 and link protein. *The EMBO Journal*, *13*(2), 286–296. http://www.ncbi.nlm.nih.gov/pubmed/7508860

Yang, C., Kim, Y., Ryu, S., & Gu, G. X. (2020). Prediction of composite microstructure stress-strain curves using convolutional neural networks. *Materials and Design*, *189*, 108509. https://doi.org/10.1016/j.matdes.2020.108509

Yin, X., Yu, T., Chen, B., Xu, J., Chen, W., Qi, Y., Zhang, P., Li, Y., Kou, Y., Ma, Y., Han, N., Wan, P., Luo, Q., Zhu, D., & Jiang, B. (2019). Spatial distribution of motor endplates and its adaptive change in skeletal muscle. *Theranostics*, *9*(3), 734–746. https://doi.org/10.7150/thno.28729

Yoon, J. H., & Halper, J. (2005). Tendon proteoglycans: Biochemistry and function. *Journal of Musculoskeletal Neuronal Interactions*, *5*(1), 22–34. https://europepmc.org/article/med/15788868

Young, J. L., & Engler, A. J. (2011). Hydrogels with time-dependent material properties enhance cardiomyocyte differentiation in vitro. *Biomaterials*, *32*(4), 1002–1009. https://doi.org/10.1016/j.biomaterials.2010.10.020

Yue, B. (2014). Biology of the extracellular matrix: An overview. In *Journal of Glaucoma* (Vol. 23, Issue 8, pp. S20–S23). Lippincott Williams and Wilkins. https://doi.org/10.1097/IJG.0000000000000108

Zamir, E. A., Czirók, A., Cui, C., Little, C. D., & Rongish, B. J. (2006). Mesodermal cell displacements during avian gastrulation are due to both individual cell-autonomous and convective tissue movements. *Proceedings of the National Academy of Sciences of the United States of America*, *103*(52), 19806–19811. https://doi.org/10.1073/pnas.0606100103

Zhang, G., Young, B. B., Ezura, Y., Favata, M., Soslowsky, L. J., Chakravarti, S., & Birk, D. E. (2005). Development of tendon structure and function: Regulation of collagen fibrillogenesis. In *Journal of Musculoskeletal Neuronal Interactions* (Vol. 5, Issue 1, pp. 5–21). International Society of Musculoskeletal and Neuronal Interactions. https://jhu.pure.elsevier.com/en/publications/development-of-tendon-structure-and-function-regulation-of-collag-4

Zhang, L. (2013). *Microstructural modeling of cross-linked fiber network embedded in continuous matrix*.

Zhang, S., Chang, M. C., Zylka, D., Turley, S., Harrison, R., & Turley, E. A. (1998). The hyaluronan receptor RHAMM regulates extracellular-regulated kinase. *The Journal of Biological Chemistry*, *273*(18), 11342–11348. http://www.ncbi.nlm.nih.gov/pubmed/9556628

Zhang, Z., Ibrahim, M., Fu, Y., Wu, X., Ren, F., & Chen, L. (2018). Application of laser scanning confocal microscopy in the soft tissue exquisite structure for 3D scan. *International Journal of Burns and Trauma*, *8*(2), 17–25. http://www.ncbi.nlm.nih.gov/pubmed/29755838

PUBLICATIONS

Peer-Reviewed Journal Articles

Leng, Y., Abdullah, A., Wendt, M., Calve, S. (2018). Hyaluronic acid, CD44 and RHAMM regulate myoblast behavior during embryogenesis. *Matrix Biology.* 78, 236-254. https://doi.org/10.1016/j.matbio.2018.08.008

Xu, X., Li, Z., **Leng, Y**., Neu, C. P., Calve, S. (2016). Knockdown of the pericellular matrix molecule perlecan lowers in situ cell and matrix stiffness in developing cartilage. *Developmental Biology*. 418(2), 242-247. https://doi.org/10.1016/j.ydbio.2016.08.029

Acuna, A., Drakopoulos, M. A., **Leng, Y.**, Goergen, C. J., Calve, S. (2018). Three-dimensional visualization of extracellular matrix networks during murine development. *Developmental biology*. 435(2), 122-129. https://doi.org/10.1016/j.ydbio.2017.12.022

Jacobson, K., Lipp, S., Acuna, A., **Leng, Y.,** Bu, Y., Calve, S. (2019). Distribution of the extracellular matrix proteome across the myotendinous junction. *Journal of Proteome Research.* 19 (10), 3955-3967. https://doi.org/10.1021/acs.jproteome.0c00248

Chen, S., **Leng, Y.**, Labi, S. (2020). A deep learning algorithm for simulating autonomous driving considering prior knowledge and temporal information. *Computer-Aided Civil and Infrastructure Engineering, 35(4), 305-321*. https://doi.org/10.1111/mice.12495

Conference Presentations

Leng, Y., Garcia, J., Calve, S. (2016). Role of hyaluronic acid in promoting myogenesis by enhancing myogenic cell migration. Poster Presentation at Midwest SDB Regional Meeting, Ann Arbor, MI

Leng,Y., Garcia, J., Calve, S. (2017). RHAMM, but not CD44, regulates the migration of skeletal muscle progenitor cells during limb development. Poster Presentation at Musculoskeletal Regenerative Medicine and Biology Meeting, St Louis, MO

Leng,Y. (2018). Weldon School's Three-Minute Thesis (3MT™) Competition, Oral Presentation at Weldon school of biomedical engineering, Purdue, West Lafayette, IN

Leng, Y., Abdullah, A., Wendt, M., Calve, S. (2018). RHAMM and CD44 both mediate the influence of hyaluronic acid on embryonic myoblast behavior. Oral and Poster Presentation at ASMB Biennial Meeting, Las Vegas, NV

Leng, Y., Bu, Y., Calve, S. (2019). The Extracellular Matrix Directs Skeletal Muscle Organization in the Developing Mouse Forelimb. Poster Presentation at BMES Annual Meeting, Ann Philadelphia, PA

Leng, Y., Jimenez, J., Calve, S., Buganza Tepole, A. (2020). Predicting the mechanical properties of fibrin gels using neural networks trained on discrete fiber network data. Oral Presentation at Summer Biomechanics, Bioengineering and Biotransport Conference, Virtual